博 士 学 位 論 文
Doctoral Thesis

論文題目

Thesis Title

Theoretical Study on Relaxation Process
in Quantum Many-Body Systems
with Spatial or Temporal Randomness

東 北 大 学 大 学 院 工 学 研 究 科

Graduate School of Engineering,

TOHOKU UNIVERSITY

専攻/Department: Applied Physics

学籍番号/ ID No: C1TD3002

氏 名 /Name: Kohei Ogane

ACKNOWLEDGEMENT

I would like to express grateful thanks to my supervisor **Prof. Hiroaki Matsueda** for guiding and advising me. I would not forget that he warmly accepted me when I was in second year of the master's course. He has provided me sharp insights in discussions, which have brought me to which direction I should proceed my study. Without his support, this thesis would not have been successfully completed.

I would like to thank **Prof. Shigemi Mizukami, Prof. Taro Yamashita and Assoc. Prof. Yukihiro Shimizu** for providing crucial comments as sub-chief examiners of my PhD thesis. Their comments would significantly improve the quality of my study.

I would like to thank **assistant professor Yusuke Masaki** for helpfully advising and discussing me. He has given me useful and suitable advice every time I asked him. His advice would have facilitated my studies to complete it.

I would like to thank **Dr. Lev Vidmar (Jozef Stefan Institute)** for suggesting the research theme and guiding me through the project. I would like to thank **Dr. Patrycja Łydżba (Wroclaw University of Science and Technology)** for fruitful discussion. Dr. Lev has warmly accepted my visiting to Jozef Stefan Institute and supported my staying there. Without their help, I would not have successfully completed the study in the second half of my doctoral course.

I express thanks to my laboratory members **Yukihiro Mastubayashi, Osamu Kanehira, Sanshiro Hatakeyama, Kanji Itoh, Tomoki Mori** for fruitful discussion and helping me to complete my studies.

I also greatly express thanks to my friends and members of choir Flare for supporting me by going out to drink and hang out.

Finally, I would not forget thank to my father for his support whenever I needed it.

Place: Sendai, Japan

Date: March, 2024 **Kohei Ogane**

TABLE OF CONTENTS

CHAPTER 1

Introduction

Main targets in solid state physics are electronic systems on crystals until now. Since these systems have the discrete translational symmetry in the spatial domain and are easy to analyze via the Bloch's theorem. Recently, periodically driven systems, which also have the discrete translational symmetry in the temporal domain, have been studied. By virtue of these symmetries, basic properties of such materials have been revealed. However, systems in the real world are more or less subject to randomness. One of the examples is an electronic system with impurities or defects. The effect of randomness on quantum systems is possible to be reduced but ultimately inevitable. While randomness worsens our predictions made for quantum systems with the translational symmetries, the random systems exhibits rich and unique phenomena. Here, I review the physical phenomena emerging in quantum systems with randomness as an introduction of this thesis.

One of the most well-known phenomena in random quantum systems is Anderson localization (AL). AL has been proposed by Anderson in 1958 for an electronic system with impurities [1]. The effect of the impurities was modeled as spatial randomness of the potential energy. Until now, much effort has been devoted to understanding AL, and the properties and the precise conditions of AL have been revealed [2–5]. Nowadays, AL is one of the crucial subjects in condensed matter physics.

Randomness in the temporal domain has been first introduced as random forces in the Brownian motion of fine particles. As well known, the random forces lead to diffusion of the fine particles. Such diffusive dynamics is also thought as one of (classical) random walks. For quantum systems, temporal randomness frequently can be seen as the effect of environmental motions on the systems [6]. Quantum walks, which are quantum versions of random walks, are also studied to reveal phenomena that occurs in temporally random quantum systems [7–15]. An important conclusion in quantum walks is that the dynamics of quantum particles is decohered under time-evolution with temporal randomness. (Here, decoherence denotes that the probability distribution of the particles relaxes and becomes same as those in classical random walks.) Furthermore, particles are also decohered in the situations where randomness exists in the both spatial and temporal domains.

Anderson localization and decoherence of quantum walks are well understood issues. However, since the calculations and experiments in random systems are quite tough because they require averaging over samples, there are remained many questions open. I pick up two subjects that relates to the studies in this thesis.

1.1 Many-body localization

AL is a single-particle problem, where any many-body interaction is absent, and has been intensively studied until now. One may think that introducing many-body interaction is just an extension of the conventional AL problem. Nevertheless, AL in the presence of many-body interaction gathers peculiar attention because it relates to a central question in non-equilibrium physics and statistical mechanics. A many-body version of AL is called as many-body localization (MBL) [16–18].

MBL is not only a target in theoretical studies but also in experiments. MBL has been studied predominantly in computations. Whereas there are several methods to numerically compute quantum many-body systems, the system size (the number of particles or spins) is highly limited to $N \sim 10 - 100$. It is problematic in studying the behavior of MBL in the thermodynamic limit (the infinite particles or spins limit). Recently, quantum simulators, for example ultracold atoms, have been utilized to study MBL [19–27]. The accessible number of particles or spins in experiments is of the order of 1000. The quantum simulators is more advantageous in studying MBL in the themodynamic limit. However, the accessible quantities in experiments are highly restricted compared with numerical calculations. In this way, MBL studies suffer from such difficulties and are still lacking.

AL is simply understood as localization of wavefucntions. In contrast, the picture of MBL is quite elusive. An aspect of MBL is interpreted from viewpoint of quantum information [28–30]. In delocalized systems, initial information encoded at a local degree of freedom, for example a local spin state at initial time, propagates over the systems and becomes untraceable by local measurements. In MBL systems, such initial information is locally preserved through the time-evolution. In this sense, MBL can be regarded as localization of quantum information. Another aspect is interpreted as localization of many-body wavefunction in the Fock space [31–33]. In general, quantum many-body problems can be mapped to single-particle hopping problem in the Fock space, where the networks of the lattices are much more complex than those in single-particle problems in the real space. Although how the Fock space localization relates to localization in real space is still controversial, there is thought to be a close relation between them. Roughly speaking, localization in the Fock space corresponds to MBL in the real space. These aspects of MBL are utilized to numerically detect MBL from delocalized one as the entanglement entropy (EE) and the inverse participation ratio (IPR) in the Fock space [33–41].

MBL is important for statistical mechanics because statistical mechanics fails to work to the MBL systems. As well known, statistical mechanics provides us an efficient algorithm to calculate observables in thermal equilibrium. However, since quantum states in isolated quantum systems are recursive, it is nontrivial that expectation values of observables irreversiblely relax to certain values [42]. However, researchers believe that most of quantum many-body systems exhibit the irreversible relaxation to thermal equilibrium and that statistical mechanics works there. A well-known example of systems avoiding such relaxations to thermal equilibrium is MBL. MBL is a universal phenomenon emerging in quantum many-body systems subject to sufficiently strong randomness in the spatial domain. Thus, studying MBL is expected to provide us insights to reveal how statistical mechanics is established in isolated quantum systems.

1.2 Entanglement growth and randomness

The entanglement entropy (EE) is an important quantity in relaxations to equilibrium. After starting time-evolution from a product state, the EE typically grows and saturates to the maximal value. How is the dynamics of the EE affected by spatial and temporal randomness?

For single-particle fermionic systems (without any many-body interactions), the dynamics of the EE can be understood by the propagation of quasi-particles. By using Wick's theorem, any correlation functions can be reduced into products of two-point correlation functions of quasi-particles $\langle c_i^\dagger(t) c_j(t) \rangle$ [43, 44]. The EE can be also obtained from the two point correlation functions [45, 46]. This implies that the propagation of the quasi-particles determines the dynamics of the correlation functions and the EE. In this sense, the dynamics of the EE is strongly affected by spatial and temporal randomness through the propagation of the quasi-particles as summarized in Table 1.1.

Table 1.1 Effect of randomness to quasi-particle propagation and entanglement

type of systems	quasi-particles	entanglement
delocalized	linear propagation	linear growth $\propto t$
localized	no propagation	immediate saturation
under temporal randomness	diffusive propagation	diffusive growth $\propto \sqrt{t}$

In many-body systems, calculating the EE is a tough task, and knowledge of the EE is still lacking. In Anderson localized systems, the EE saturates immediately and never grows extensively. In contrast, in MBL systems, the EE grows logarithmically in time although there is no transport [47, 48]. In some systems with temporal randomness, the growth of the EE follows Kardar-Parisi-Zhang (KPZ) equation, and entanglement entropy grows in time t as $\sim v_{\mathrm{E}} t + B t^{1/3}$ [49–51]. In the random quantum circuit model, where the time evolution is given by random unitary operators, the EE can be obtained analytically by using geometrical optimization in $(1+1)$-dimensional time-space plane. The dynamics of the EE in many-body systems is affected by randomness as well as that in single-particle systems. However, the detail behavior of the EE in generic many-body systems with randomness are undergoing.

1.3 Outline

This chapter is devoted to the introduction of this thesis. The remained parts of this thesis is organized as follows.

In Chap. 2, I study the time evolution of quasi-particles (domain walls) in the transverse field Ising model with temporal randomness. As mentioned above, the temporal profiles of the propagating quasi-particles determine the relaxation of correlation functions and the growth of the EE. This study is motivated by a study in the Ising model with binary and temporal fluctuating field. That study has shown that the propagation of the quasi-particles is super-diffusive under specific conditions. I test the robustness of the super-diffusive propagation against introducing an additional interaction term. I find that, after introducing the additional term, the super-diffusive propagation disappears. This result can be explained by using eigenvectors of stroboscopic time evolution operators.

In Chap. 3, I study the nonergodic (MBL) transition in the anisotropic Heisenberg model realized on the Rydberg atoms. The word "nonergodic" means that a given system has no ability to have the relaxation to thermal equilibrium. Shortly, statistical mechanics no longer work in nonergodic systems. The precise condition of the nonergodic transition is still open. Especially, whether many-body systems are able to be nonergodic in the thermodynamic limit is a crucial and challenging question. Recently, an experimental study has reported a fingerprint that the non-ergodicity may be observed in the Rydberg atoms. I numerically analyze the nonergodicity by using indicators, i.e., the EE and the inverse participation ratio. I found the transition from the ergodic regime to the nonergodic regime and the shift of the critical disorder strength with increasing the number of the Rydberg atoms.

In Chap. 4, I summarize two studies as a conclusion.

CHAPTER 2

Robust modes against temporally random field

2.1 Introduction

Quantum walks have originally introduced as quantum versions of classical random walks [52]. In setting of quantum walks, a quantum particle is initially put on a center of a system, and its wavefunction spreads over the system in the following time-evolution. Quantum walks have unique features that quite differ from those in classical random walks. Classical random walks display diffusive propagation of the particles and their probability distributions are Gaussian as in Fig. 2.1(b). In contrast, in quantum walks, a particle propagates ballistically and its probability distribution has two peaks at the edges of the probability distribution as in Fig. 2.1(a). The detail definition of diffusive and ballistic propagation is provided later. Since ballistic propagation is quite faster than diffusive one, quantum walks have been gathering attention in that they have potential to application for search algorithms.

Here, I clearly define the words "diffusive" and "ballistic" propagation. In both quantum and classical random walks, a particle is treated as a probability distribution $P(x,t)$. To extract a characteristic quantities from the probability distribution, one can define the variance of the probability distribution $\sigma^2(t)$ to quantify how extent the probability distribution spreads at time t. In the setting of quantum and random walks, the probability distribution is initially localized at a center of the system, where the variance is quite small. Through the time-evolution, the probability distribution becomes spread, and simultaneously the variance becomes larger. In long time scale, the standard deviation at time t, $\sigma(t)$, becomes $t^{1/z}$. The exponent z is called as the dynamical exponent. Propagation with $1/z = 1$ is referred to as ballistic propagation, and that with $1/z = 0.5$ is to as diffusive propagation. The relation between the standard deviation and the dynamical exponent is summarized in Fig. 2.1.

Table 2.1 Type of randomness and propagation

type of randomness	propagation	dynamical exponent z
none	ballistic	1
spatial	none	0
temporal	diffusive	2
spatial and temporal	diffusive	2

The dynamical properties in quantum walks are strongly affected by spatial and temporal randomness. While the ballistic dynamics is typically obtained in homogeneous systems, a particle is localized and does not propagates as $\sigma \sim 1$ in spatially localized systems in one dimension [53–57]. The particle propagates diffusively under temporal noises as $\sigma \sim \sqrt{t}$, regardless of the existence of

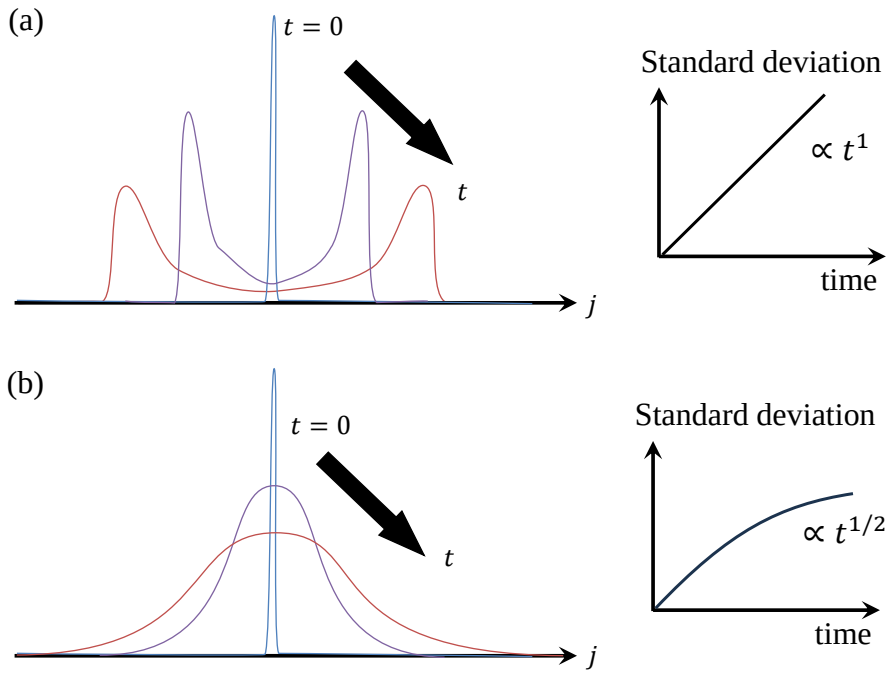

Fig. 2.1 Picture for quantum and (classical) random walks. (a) A typical probability distribution of quantum walks. The distribution has two peaks around edges of the distribution whereas the central part of the distribution is suppressed. The standard deviation of the distribution is proportional to time t, i.e., ballistic. (b) A typical probability distribution of (classical) random walks. In contrast to quantum walks, the distribution is Gaussian and the central part has a dominant weight. The standard deviation is proportional to $t^{1/2}$, i.e., diffusive.

spatial randomness [7–15]. The relation between the type of randomness and the dynamical exponent is summarized in Table 2.1.

There are two different formulations in quantum walks: a discrete-time quantum walk (DTQW), or a continuous-time quantum walk (CTQW) [58]. The main difference between them is in the ways of time-evolution. In DTQWs, time-evolution is performed by two unitary operators, a coin operator and a displacement operator. Since one needs to operate two time evolution operators for time t, the time evolution have discreteness. This formulation is natural as an expansion from the formulation of classical random walks. On the other hand, a time evolution operator in CTQW is given by a solution of the Schrödinger equation and is continuous. Thus, a CTQW is closer to the formulations of condensed matter physics and provides us information of non-equilibrium properties in condensed matters. Sachdev has first showed that the relaxation of observables can be estimated from the semi-classical trajectories of quasi-particles [43]. Treating the propagation of quantum objects classically is not an exact way. However, in the semi-classical theory, Sachdev can estimate the relaxation of the observables from the semi-classical trajectories with high accuracy to the exact result. Unitl now, this framework has been applied to integrable and disordered systems, and it has successfully estimated observables and correlations [44, 59]. Later, Roósz *et al.* has analyzed the quasi-particle dynamics in the one-dimensional transverse field Ising model (TFIM) whose transverse field is random in the temporal domain as in Fig. 2.3(c) [60]. The transverse field is randomly chosen from $\pm h$ at every time step with interval τ. They have shown that the standard deviation of the probability distribution of a

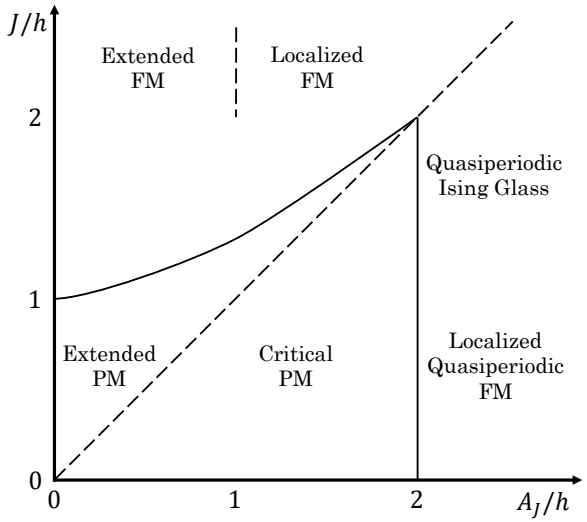

Fig. 2.2 Phase diagram of the QP-TFIM. The complexity is due to the various symmetries in individual parameter regimes. The abbreviation PM and FM indicate paramagnetic and ferromagnetic, respectively. The diagram was obtained by A. Chandran *et al.*

domain wall displays diffusive or super-diffusive behaviors $\sigma \sim t^{1/z}$ $(0.5 \leq 1/z < 1)$, depending on the interval τ. Furthermore, for a certain interval, the super-diffusive propagation is observed even in long time scale. Since the diffusive propagation implies completely decoherence of the coherence of the quasi-particles, the super-diffusive propagation denotes that the coherence of the quasi-particles is partially preserved even under temporal random field. In this study, I challenge to solve the questions whether the nearly ballistic propagation is broken by introducing an additional term to the system and how it is broken.

Spatial randomness brings localization of wavefunctions to systems where no many-body interaction works between particles as well known as Anderson localization [1]. The type of the spatial randomness originally used in Anderson localization is (quenched) random disorder (RD) in local chemical potential, which has no correlation between chemical potentials at two different points in the system. Quasi-periodicity (QP) also leads to localization of wavefunctions. The Hamiltonian's parameters of QP systems are modulated with incommensurate periods with lattice spacing. QP systems have been originally introduced by Abzel, Aubry and André [61, 62]. Compared with RD systems, QP systems have been less intensively studied but revealed some features in QP systems. While localization appears even for infinitesimal randomness in one-dimensional RD systems, QP systems display the localized-delocalized transition in one dimension. QP systems at critical points have fractal structure in their eigenenergies and eigenstates [63–65], and they display anomalous diffusion [66–68]. Whereas QP systems have these rich properties, there are not various options in QP models: the Aubry-André model is predominantly used in studying QP systems [69–72]. Recently, a new type of QP model, the quasi-periodic transverse field Ising model (QP-TFIM), has been proposed [73–75]. Analytical study has revealed that the QP-TFIM has the complicated phase diagram as in Fig. 2.2. From the viewpoint of localization, the phases are roughly categorized into three phases: extended, localized, and critical phases. In the extended phase, quasi-particles propagate ballistically whereas no transport is in the localized phase. Between them, there is the critical phase, where prop-

agation of the quasi-particles is extremely slow. The dynamics under the static Hamiltonian of the QP-TFIM has been revealed in Ref. [75]. However, since systems in the real world are more or less subject to temporally random field, it is worthwhile to reveal the non-equilibrium properties in a QP system under temporally randomness.

In this study, I consider the propagation of a domain wall in the QP-TFIM under binary and temporally random field. The transverse field is randomly chosen from $\pm h$ at every time step with an interval τ. The way that a domain wall spreads is a key to understanding the relaxation in the QP-TFIM because the local observables and correlation functions can be estimated from the semi-classical theory. Thus, I perform stroboscopic time-evolution and average the probability distribution over realized sequences of the binary and temporally random field. My calculations are performed within the extended paramagnetic (extended PM) region shown in Fig. 2.2, which contacts to the critical point of the TFIM. The results on the propagation of a domain wall can be summarized as follows. Short-time behaviors depend on τ, and the propagation of a domain wall is super-diffusive for certain values of τ. In contrast, the propagation approaches to be diffusive for any interval τ in long time scale. I also calculate the relaxation of a two-point spin-spin correlation function and the bipartite entanglement entropy (EE). The exponents in the relaxation of the correlation function is consistent with the dynamical exponents of the domain wall. Such dependence of the dynamical exponents on τ can be explained by the overlap between the eigenvectors of the static Hamiltonian with $\pm h$. For the TFIM, the overlap has a quite simple structure, which leads to nearly ballistic dynamical exponents for certain τ. In contrast, for the QPTFIM, finer structures appear as the strength of the quasi-periodic spin-spin couplings increases, which leads to a diffusive dynamics for any τ.

This chapter is organized as follows. In Sec. 2, I summarize the result in Roósz's paper. In Sec. 3, I describe the Hamiltonian and the formalism to analyze the motion of domain walls. In Sec. 4, I show the results obtained in numerics. In Sec. 5, I provide an explanation to the results and conclude this chapter.

2.2 Super-diffusive dynamics in clean transverse field Ising model

Roósz *et al.* have studied the dynamics of a domain wall in the TFIM under the binary and temporally random field and have shown that the domain wall propagates super-diffusively in a certain condition [60]. Here, I summarize the setting employed in Roósz's paper and the results. The detail definition and formulation is provided in Sec. 2.3.

The authors have analyzed one-dimensional Ising model under the binary and temporally random field (Fig. 2.3(c)). The field takes only two values $+h$ or $-h$ and randomly changes its sign at every time step with an interval τ. Between the adjacent time steps, the field is constant (static). They have simulated the time evolution of a domain wall in the following setting. The initial state has a domain wall localized at the center of the system as in Fig. 2.3(b). Under time-evolution, the domain wall propagates over the system. They have computed the probability distribution of the single domain wall, the corresponding standard deviation and the dynamical exponent.

The dynamical exponent is a quantity to characterize the way of the propagation. In clean quantum

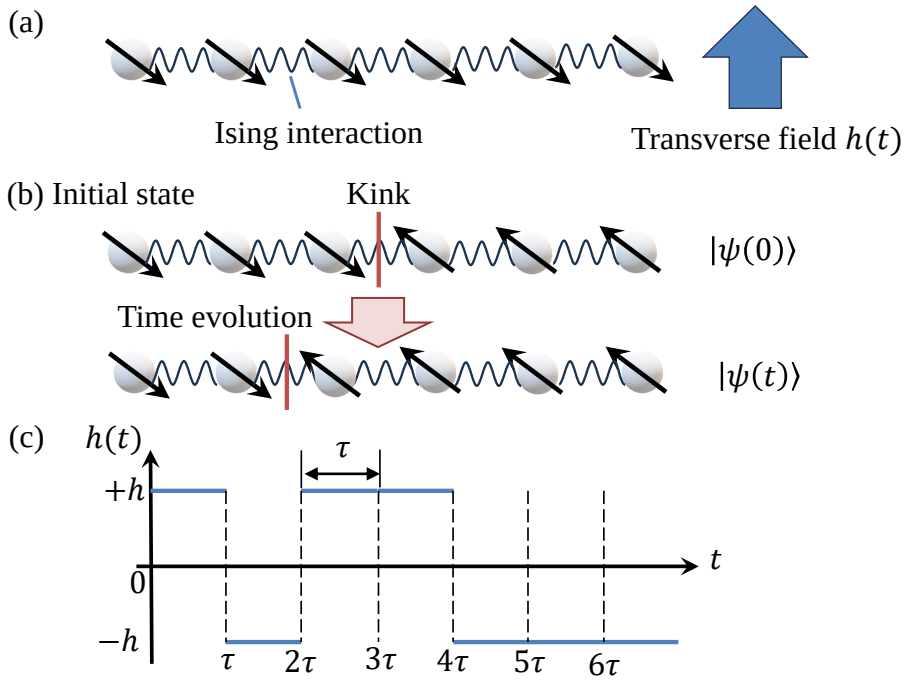

Fig. 2.3 (a) Schematic picture of transverse field Ising model in one dimension. The spins are coupled by the Ising interaction and are subject to the transverse field that is binary and temporally random. The profile of the transverse field is shown in Fig. 2.3(c). (b) The initial state has a domain wall at the center of the system. The domain wall propagates under time evolution. (c) The profile of the binary and temporally random field. The field takes only two values $\pm h$ and may change its sign at every time steps. The interval of the time steps is τ.

systems, particles propagate ballistically, that is, with constant velocities, and the dynamical exponent is 1. On the other hand, in classical systems where particles move in probabilistic manners, the particles propagate diffusively, that is, with velocity slowing down gradually but never stopping. The dynamical exponent in such systems is 2. Quantum walks are generally classified into the same class as classical random walks. I shown the dynamical exponent of a domain wall under the binary and temporally random field in Fig. 2.4(a), which is quoted from the original paper [60]. The parameters of the Hamiltonian are set as $J = h = 1, L = 2048$. The system size L is large enough to avoid an appearance of an effect from the edges within the time scale in the calculation. One finds that the dynamical exponent depends on the interval τ and takes super-diffusive vales for $\tau \geq \pi/2$ in spite of the existence of the temporal randomness. The dynamical exponent reaches the maximum at $\tau = \pi/2$. The shape of the probability distribution at $\tau = \pi/2$ has unique peaks: a peak pinned at the center and two peaks moving outwards around the edges of the distribution as in Fig. 2.4(b). The outer peaks moves ballistically and cause the super-diffusive (nearly ballistic) dynamics of the domain wall. The central peak is same as the diffusive distribution derived from random walks or the thermal equation, which can be checked by the rescaled distribution depicted in Fig. 2.4(d). The diffusive distribution at place l and time t is given by

$$p_l(t) = \frac{1}{2\sqrt{\pi D t}} \exp\left[-\frac{(l-l_0)^2}{4Dt}\right], \tag{2.1}$$

where $4Dt$ is the variance of the diffusive probability distribution. After taking logarithm, one find that

$$\ln[p_l(t)\sqrt{t}] \propto -\frac{1}{4D}\left(\frac{l-l_0}{\sqrt{t}}\right)^2. \tag{2.2}$$

In Fig. 2.4(d), a quadratic curve of $(l-l_0)/\sqrt{t}$ indicates a diffusive distribution. The central peak is collapsed although the outer peaks still move. In this way, at $\tau = \pi/2$, the probability distribution has both features of (classical) random and quantum walks. For $\tau < \pi/2$, the distribution becomes to fit the diffusive scaling in Fig. 2.4(c).

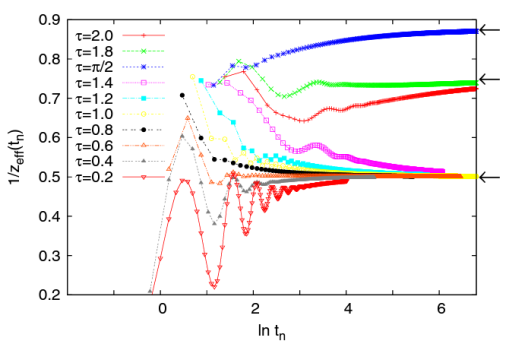

(a) Dynamical exponent

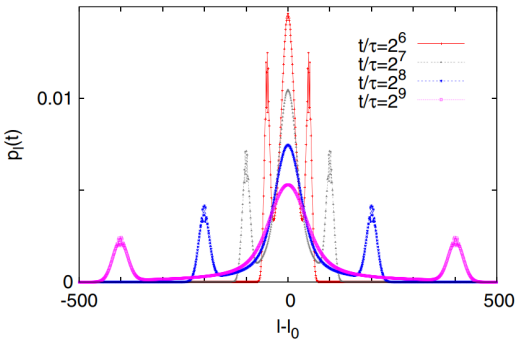

(b) Probability distribution at $\tau = \pi/2$

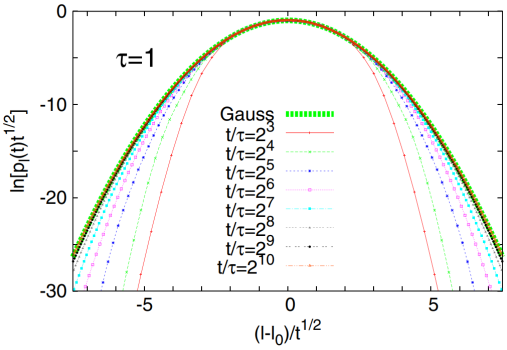

(c) Rescaled probability distribution at $\tau = 1$

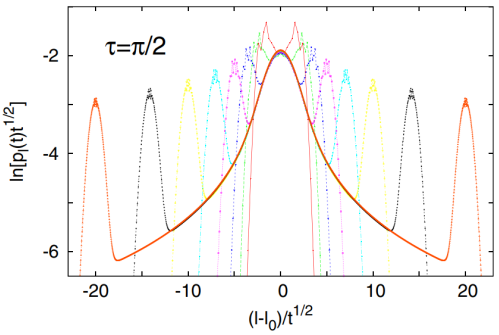

(d) Rescaled probability distribution at $\tau = \pi/2$

Fig. 2.4 (a) Dynamical exponent for several intervals τ. The result has been obtained for $J = h = 1$ and $L = 2048$. For τ less than $\pi/2$, the dynamical exponent approaches to the diffusive value in long time. At $\tau = \pi/2$, the dynamical exponent in long time reaches the maximum value (super-diffusive). For τ more than $\pi/2$, the dynamical exponent in long time takes the intermediate value (super-diffusive). Remarkably, the super-diffusive dynamical exponent never decay into the diffusive value as long as it has been calculated. (b) Probability distribution at $\tau = \pi/2$. The distribution has a peak around the center and two peaks at the front of the distribution. (c) Rescaled probability distribution around the center at $\tau = 1$. In the figure, a quadratic form of $(l-l_0)/\sqrt{t}$ denotes a diffusive probability distribution. The distribution approaches to the diffusive one in long time. (d) Rescaled probability distribution at $\tau = \pi/2$. The central part is diffusive whereas the peaks moves outwards ballistically. All of the figures are quoted from [60].

Furthermore, they have provided an explanation to the super-diffusive propagation by using eigenvectors of the stroboscopic time evolution operator. The detail description is provided in Sec. 2.5. The key is an eigenvector of both two types of time evolution operators. Generally, an eigenvector of a Hamiltonian $\hat{H}_A$ is not changed by operating the time evolution operator of the Hamiltonian $\hat{H}_A$.

On the other hand, the eigenvector generally is changed by operating the time evolution operators of different Hamiltonian $\hat{H}_B$. However, for $\tau \geq \pi/2$, a certain eigenvector is not changed by operating the time evolution operators of $\hat{H}_B$. Since the eigenvector is preserved under the temporally random field, the dynamics also exhibits (partially) quantum properties for $\tau \geq \pi/2$.

2.3 Hamiltonian and formalism

The formalism to analyze the motion of a domain wall is summarized as follows. Domain walls in the TFIM can be written in a quadratic form of the Majorana fermion. Instead of calculating wave-functions, I calculate a two-point correlation function of the Majorana fermion. The time-evolution is computed at time steps with an interval τ, which is called as stroboscopic time-evolution. Since the Hamiltonian is static between the adjacent time steps due to the property of the binary and temporally random field, the stroboscopic time-evolution can be realized by randomly operating two types of time evolution operators. After averaging the probability distribution over realizations of the random field, the standard deviation and the dynamical exponent is obtained.

2.3.1 Stroboscopic time evolution

The time-evolution is implemented by time evolution operators $\hat{U}(t)$, which is defined as a solution of the Schrödinger equation. The time-evolution operator for static Hamiltonian is given by a simple form $\mathrm{e}^{-\mathrm{i}\hat{H}t}$. On the other hand, for time dependent Hamiltonian, it takes a more complex form $\mathcal{T}\mathrm{e}^{-\mathrm{i}\int_0^t \mathrm{d}t'\hat{H}(t')}$ with the time ordering operator $\mathcal{T}$. In general, computing $\mathcal{T}\mathrm{e}^{-\mathrm{i}\int_0^t \mathrm{d}t'\hat{H}(t')}$ in a specific problem is difficult because approximation is necessary in a majority of the cases.

Nevertheless, the time evolution operator under the binary and temporally random field $h(t)$ can be computed in a simple way. The key is the property that $h(t)$ randomly changes at time steps with an interval τ and $h(t)$ is constant between the adjacent time steps. Since the Hamiltonian is also static between the adjacent time steps, the time evolution operator between the adjacent time steps is given by $\mathrm{e}^{-\mathrm{i}\hat{H}\tau}$. The properties of the random field in question reduces the time evolution operators under the time-dependent field into a pair of the time evolution operators under the static Hamiltonians, i.e., $\hat{u}_+(\tau) = \mathrm{e}^{-\mathrm{i}\hat{H}_+ t}$ and $\hat{u}_-(\tau) = \mathrm{e}^{-\mathrm{i}\hat{H}_- t}$ where $\hat{H}_\pm$ are static Hamiltonians and the subscript $\pm$ is the sign of $h(t)$. These descriptions are advantageous to compute the time-evolution because the time-evolution for time $t = n\tau$ is reduced to random operation of $\hat{u}_+(\tau)$ and $\hat{u}_-(\tau)$. Shortly,

$$\mathcal{T}\mathrm{e}^{-\mathrm{i}\int_0^{n\tau} \mathrm{d}t'\hat{H}(t')} = \hat{u}_{s_n}(\tau)\hat{u}_{s_{n-1}}(\tau)\cdots\hat{u}_{s_1}(\tau), \tag{2.3}$$

where s_n is the sign of $h(t)$ at nth interval. For this reason, the stroboscopic time-evolution, that is, discretized time-evolution efficiently works to compute the time-evolution in the system under the binary and temporal random field.

2.3.2 Hamiltonian and Majorana fermion

The Hamiltonian of the TFIM is defined as

$$\hat{H}(t) = -\frac{J}{2}\sum_{i=1}^{L}\hat{\sigma}_i^x\hat{\sigma}_{i+1}^x - \frac{h(t)}{2}\sum_{i=1}^{L}\hat{\sigma}_i^z, \tag{2.4}$$

where $\hat{\sigma}_i^\alpha$ is a Pauli operator at ith site, J is the strength of the Ising interaction, and $h(t)$ is the binary and temporally random filed. The spatial dimension is one, and the boundary condition is set to open.

The static Hamiltonian between the adjacent time steps is given by

$$\hat{H}_\pm = -\frac{J}{2}\sum_{i=1}^{L}\hat{\sigma}_i^x\hat{\sigma}_{i+1}^x - \frac{\pm h}{2}\sum_{i=1}^{L}\hat{\sigma}_i^z. \tag{2.5}$$

The Hamiltonian can be written in a quadratic form of the Majorana fermion:

$$\hat{H}_\pm = \frac{1}{4}\sum_{\mu=1}^{2L}\hat{\gamma}_\mu[\mathsf{H}_\pm]_{\mu\nu}\hat{\gamma}_\nu. \tag{2.6}$$

The matrix $\mathsf{H}_\pm$ is tridiagonal and skew. The Majorana fermion is composed from Pauli operators as

$$\gamma_{2i-1} = \Big[\prod_{j=1}^{i-1}(-\hat{\sigma}_j^z)\Big]\hat{\sigma}_i^x, \quad \gamma_{2i} = \Big[\prod_{j=1}^{i-1}(-\hat{\sigma}_j^z)\Big]\hat{\sigma}_i^y \tag{2.7}$$

and has an anti-commutation relation

$$\{\hat{\gamma}_\mu, \hat{\gamma}_\nu\} = 2\delta_{\mu\nu}. \tag{2.8}$$

Note that the subscript in the Majorana fermion operators does not correspond to the site in the real space. In the representation of the complex fermion (usual fermion), there are two types of the operators at a single site, i.e., creation and annihilation operators. On the other hand, in the Majorana fermion representation, there is only one type of the operator at a single site. Instead of that, the number of sites defined for the Majorana fermion is double of that in the real space.

The Majorana fermion can be interpreted as creation and annihilation operators of domain walls for the following reason. Consider a state $|{+x}\rangle \equiv \{|{\rightarrow}\rangle\}^{\otimes L}$ with $|{\rightarrow}\rangle = (|{\uparrow}\rangle + |{\downarrow}\rangle)/\sqrt{2}$ and operate $\hat{\gamma}_\mu$ onto it:

$$\hat{\gamma}_{2j-1}|{+x}\rangle = (-1)^{j-1}|{\leftarrow_1}\cdots{\leftarrow_{j-1}}{\rightarrow_j}{\rightarrow_{j+1}}\cdots{\rightarrow_L}\rangle \tag{2.9}$$

$$\hat{\gamma}_{2j}|{+x}\rangle = \mathrm{i}(-1)^{j}|{\leftarrow_1}\cdots{\leftarrow_{j-1}}{\leftarrow_j}{\rightarrow_{j+1}}\cdots{\rightarrow_L}\rangle\,. \tag{2.10}$$

One find that $\hat{\gamma}_{2j-1}$ creates a domain wall between $(j-1)$th and jth spins, and $\hat{\gamma}_{2j}$ creates a domain wall between jth and $(j+1)$th spins. Since $\hat{\gamma}_m^2 = 1$, the Majorana operators annihilate a domain wall at the same place where the operator creates a domain wall. In this sense, the Majorana fermion operators can be considered as creation and annihilation operators for domain walls as long as they

are operated onto $|+x\rangle$.

The detail derivation of the Majorana representation of the Hamiltonian as in Eq. 2.6 is provided in Appendix.

The time evolution of the Majorana fermion is derived from the Heisenberg equation

$$\mathrm{i}\frac{\partial}{\partial t}\hat{\gamma}_\mu(t) = \sum_\nu [\mathsf{H}_\pm]_{\mu\nu}\hat{\gamma}_\nu(t), \tag{2.11}$$

where $\hat{\gamma}_\mu(t)$ is written in the Heisenberg representation. The time evolution of the Majorana fermion is given by a solution of the above equation as

$$\hat{\gamma}_\mu(t) = \sum_\nu [\mathsf{O}_\pm(t)]_{\mu\nu}\hat{\gamma_\nu}(0), \tag{2.12}$$

where the matrix $\mathsf{O}_\pm(t)$ with respect to the time evolution of the Majorana fermion is an orthogonal matrix because $\mathsf{H}_\pm$ is skew. The subscript $\pm$ correspond to the sign of the binary and temporally random field $h(t)$

2.3.3 Definition of dynamical exponent

The aim in this study is revealing the motion of a domain under the binary and temporally random field. To achieve this aim, a correlation function of the Majorana fermion

$$G_\mu(t) = \frac{1}{\sqrt{2}}\langle +x|\,\hat{\gamma}_\mu(t)\hat{\gamma}_L\,|+x\rangle \tag{2.13}$$

is considered. This correlation function can be considered as a wavefunction of a domain wall for the following reasons.

The time evolution of the correlation function takes the same form as that of the Majorana fermion. One obtained it after substituting Eq. 2.12 to Eq. 2.13 as

$$G_\mu(t) = \sum_\nu [\mathsf{O}_\pm(t)]_{\mu\nu}G_\nu(0). \tag{2.14}$$

Since the matrices $\mathsf{O}_\pm(t)$ are orthogonal, the sum of $|G_\mu(t)|^2$ is conserved as

$$\sum_\mu |G_\mu(t)|^2 = \sum_{\mu\nu\lambda} G^*_\nu(0)[\mathsf{O}_\pm(t)]^*_{\nu\mu}[\mathsf{O}_\pm(t)]_{\mu\lambda}G_\lambda(0) = \sum_\nu |G_\nu(0)|^2. \tag{2.15}$$

Furthermore, the initial value of the correlation function is given by $G_L = 1/\sqrt{2}$, $G_{L+1} = \mathrm{i}/\sqrt{2}$ and otherwise $G_i = 0$, and the sum at initial time $\sum_\mu |G_\mu(0)|^2$ is 1. In this sense, $\{|G_\mu(t)|^2\}$ and $G_\mu(t)$ can be regarded as a probability distribution and an amplitude of the probability, respectively.

The physical meaning of the correlation function is an amplitude to find a domain wall at place μ and time t after initially creating a localized domain wall at the center of the system. As seen in the above subsection, $\hat{\gamma}_L$ creates a domain wall between $(L/2)$th and $(L/2+1)$th spins to the state $|+x\rangle$. $\hat{\gamma}_\mu(t)$ also creates a domain wall corresponding the subscript μ at time t to $\langle +x|$. The inner product

of these states is finite if the domain wall propagates to μ at time t.

The probability distribution of a domain wall at place j and time t is defined as

$$P_j(t) = |G_{2j-1}(t)|^2 + |G_{2j}(t)|^2. \tag{2.16}$$

The reason why $P_j(t)$ has two contributions is because the Majorana fermion is defined on doubled degrees of freedom compared with spins. At the initial time, the probability distribution has only finite value at $j = L/2$ or $j = L/2 + 1$.

The time evolution is implemented under temporal randomness coming from the transverse field. Thus, the universal behavior appears at quantities averaged over the realization of the randomness. Before proceeding the next step, one needs to average the probability distribution over the realizations of random fields. I denote the averaged probability distribution as

$$\langle P_j(t) \rangle = \frac{1}{N_s} \sum_{n_s} P_j^{n_s}(t), \tag{2.17}$$

where n_s is the number of a random realization, N_s is the total number of the realizations.

To quantify the probability distribution, the standard deviation is defined as

$$\sigma(t) = \sqrt{\sum_j \langle P_j(t) \rangle (j - j_0)^2}, \tag{2.18}$$

where the central position of the system $j_0 = (L + 1)/2$. The standard deviation represents how widely the probability distribution spreads at time t from the initial position. The standard deviation is $\propto t^1$ in ballistic systems while $\propto t^{1/2}$ in diffusive systems. Thus, the dynamical exponent of the standard deviation is defined as

$$\sigma(t) \propto t^{1/z}. \tag{2.19}$$

Practically, the dynamical exponent z is computed in the stroboscopic time evolution as

$$\frac{1}{z(t_n)} = \frac{\ln\Big[\sigma(t_n)/\sigma(t_{n-1})\Big]}{\ln\Big[t_n/t_{n-1}\Big]}, \tag{2.20}$$

where the discrete time $t_n = n\tau$.

2.3.4 Quasi-periodic disorder

In Roósz's paper, they have focused on the uniform TFIM. I add a kind of disorder, the quasi-periodicity to the system. The TFIM with the quasi-periodicity is called as the quasi-periodic transverse field Ising model (QP-TFIM).

The Hamiltonian of the OP-TFIM is defined as

$$\hat{H} = -\frac{1}{2}\sum_{i=1}^{L} J_{i+1/2}\hat{\sigma}_i^x\hat{\sigma}_{i+1}^x - \frac{1}{2}\sum_{i=1}^{L} h_i\hat{\sigma}_i^z, \tag{2.21}$$

where the quasi-periodic Ising interaction $J_{i+1/2} = J + A_J\cos\big(Q(i+1/2)\big)$, and the quasi-periodic transverse field $h_i = h + A_h\cos\big(Qi\big)$. Here, $Q = 2\pi \times q$ with an irrational number $q = (\sqrt{5}-1)/2$. If $A_J = 0$ and $A_h = 0$, the Hamiltonian corresponds to that of the uniform TFIM. Chandran *et al.* analytically studied the properties of eigenstates in the QP-TFIM. The results is summarized in Fig. 2.2. When drawing the diagram, the quasi-periodicity in the transverse field A_h is set to zero. The vertical line at $A_J = 0$ corresponds to the TFIM. On the TFIM line and around its vicinity, the eigenstates are extended over the system. In the extended regime, quasi-particles propagate ballistically. On the opposite side, the spins are subject to the strong quasi-periodicity, and the eigenstates are glassy or localized, where quasi-particles can not move extensively. Between them, there appears a critical regime, where quasi-particles propagate extremely slowly. In this study, I focus on the extended PM regime, which is in contact with the critical point of the TFIM.

In this study, the quasi-periodicity in the transverse field A_h is omitted. The static Hamiltonian of the QP-TFIM is given by

$$\hat{H}_\pm = -\frac{1}{2}\sum_{i=1}^{L} J_{i+1/2}\hat{\sigma}_i^x\hat{\sigma}_{i+1}^x - \frac{\pm h}{2}\sum_{i=1}^{L}\hat{\sigma}_i^z. \tag{2.22}$$

The matrices in the Majorana forms of the Hamiltonian $\mathsf{H}_\pm$ is given by changing the Hamiltonian parameters as $J \to J_{i+1/2}$ in Eq. A.26.

2.3.5 Some properties in static Hamiltonian

The static Hamiltonian matrices $\mathsf{H}_\pm$ have essential properties for this study. First, the chiral transformation changes the sign of eigenvalues of $\mathsf{H}_\pm$. The argument can be checked by using the chiral matrix $\mathsf{C} = \mathrm{diag}[-1, 1, -1, 1, \cdots]$ as

$$\mathsf{C}\mathsf{H}_\pm\mathsf{C} = -\mathsf{H}_\pm. \tag{2.23}$$

This leads to a property that, if $+\epsilon_\mu$ is an engenvalue of $\mathsf{H}_\pm$, then $-\epsilon_\mu$ is also an eigenvalue. Second, the static Hamiltonian with the transverse field $\pm h$ can be transformed to that with $\mp h$ by the parity operator that simultaneously flips all spins $\prod_i \hat{\sigma}_i^x$ as

$$\Big[\prod_i \hat{\sigma}_i^x\Big]\hat{H}_+\Big[\prod_i \hat{\sigma}_i^x\Big] = \hat{H}_-. \tag{2.24}$$

This relation leads to the same eigenspectra between $\hat{H}_+$ and $\hat{H}_-$ whereas the eigenvectors of $\hat{H}_\pm$ differ from each other. The eigenvectors of $\hat{H}_\pm$ can be obtained by operating $\prod_i \hat{\sigma}_i^x$ to the eigenvectors of the other Hamiltonian $\hat{H}_\mp$.

2.4 Super-diffusive dynamics in quasi-periodic transverse field Ising model

I show the results of the dynamical exponent in Fig. 2.5. As a property independent on τ, the dynamical exponent $1/z$ decays to the diffusive value after long time evolution within the range of time scale and parameters in my calculation. The dependence of the dynamical exponent on the interval τ at $A_J = 0.5$ is depicted in Fig. 2.5(a). The dynamical exponent $1/z$ slowly decays at $\tau/2\pi = 1.2$ whereas at $A_J \neq 1.2$ the dynamical exponent decays apparently faster. This behavior also can be found at $A_J = 2.4$ as shown in the inset of Fig. 2.5(a).

The dependence on the quasi-periodicity A_J at the fixed interval $\tau = \pi/2$ is shown in Fig. 2.5(b). For TFIM ($A_J = 0$), the dynamical exponent does not relaxes to the diffusive value in long time scale. On the other hand, the dynamical exponent relaxes to the diffusive value, whose relaxation speed gets faster as A_J increases. I rescale the dynamical exponent by taking logarithm as in Fig. 2.5(c). The time dependence of the dynamical exponent is $\propto t^{-1.06}$. The exponent -1.06 is obtained by fitting. The profiles of the relaxation of $1/z$ for various A_J are collapsed to a single curve by rescaling the horizontal axis as $A_J^{1.6}\ln[t/2\pi]$ (not shown in figure). However, the meaning of the exponent of A_J is unresolved and out of scope in this study.

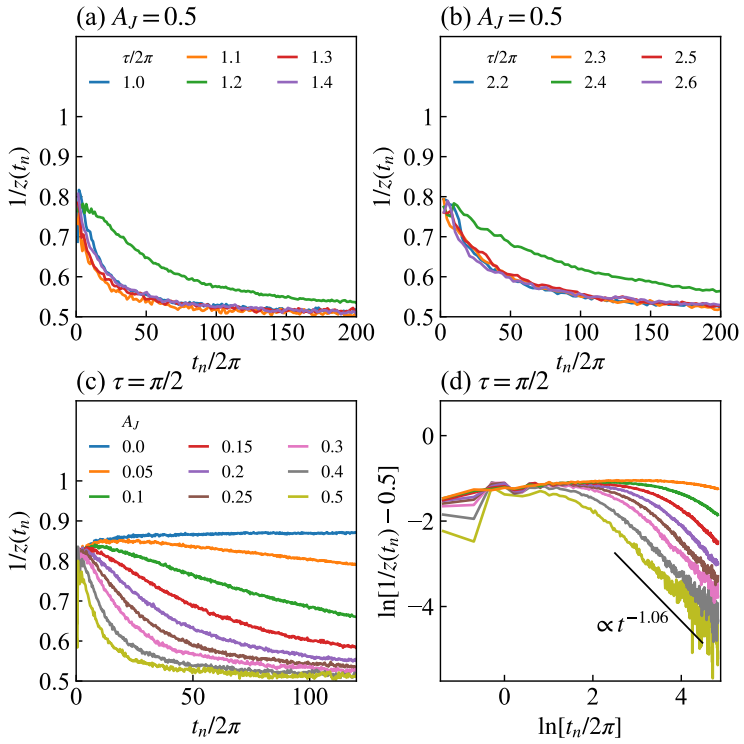

Fig. 2.5 Dynamics of inverse dynamical exponents, where all calculations were performed with $L = 2048, N_{\mathrm{samp}} = 10^4$. (a) Dependence of the fluctuation times τ on the dynamics of $1/z(t_n)$ at $A_J = 0.5$. The inverse dynamical exponent $1/z(t_n)$ approaches to the diffusive value 0.5 for most fluctuation times τ, except for $\tau/2\pi = 1.2, 2.4$. (b) Dependence of the quasi-periodic spin couplings A_J at $\tau/2\pi = 0.25$. The dynamical exponent at $A_J = 0$ (TFIM) does not drop to the diffusive value 0.5. In contrast, the other dynamical exponents reach the diffusive value in the long time scale, with the speed of the decay tending to be faster with increasing A_J. (c) Log-log plot of the relaxation curves in (b). The dynamical exponents exhibit power-law decay, and the slopes of the curves become the same in the long time scale.

I also show the profile of the probability distribution for the weak quasi-periodicity $0 \leq A_J \leq 0.2$ in Fig. 2.6. The profile is on the diffusive scaling, which is introduced in Sec. 2.2, in the figure. At $A_J = 0$ (TFIM), the distribution has two peaks moving outwards and a central peak collapsed after the diffusive scaling. The central peak is quadratic in the figure, which means the central peak is Gaussian. At $A_J = 0.1$, the two moving peaks become smaller in the amplitude as time advances. The part corresponding to the central peak becomes deviated from the initial curve in the time evolution. For larger A_J, the two moving peaks almost disappear and the central peak becomes to a quadratic curve with larger width than that at the initial time.

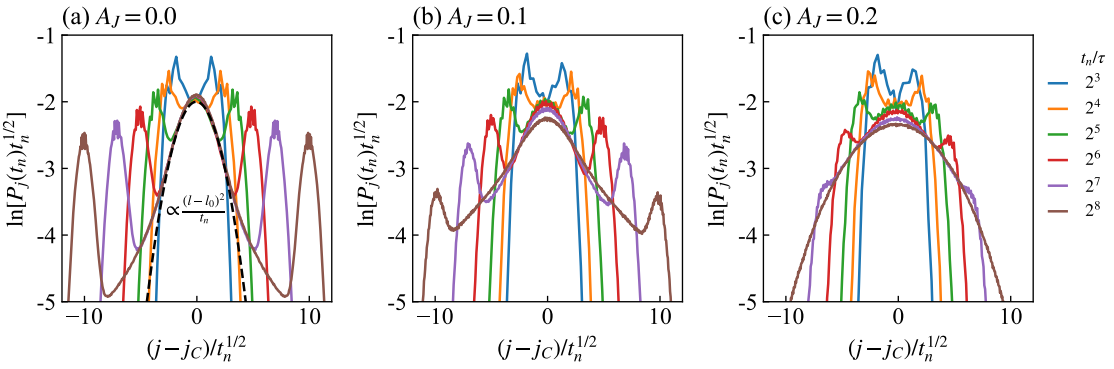

Fig. 2.6 Scaling of the shapes of the probability distributions for $A_J = 0, 0.1, 0.2$ (a-c, respectively). For $A_J = 0$ (TFIM), two outside peaks can be seen, and the distributions are not on the quadratic curve of the diffusive scaling. The peaks are suppressed as A_J increasing. For $A_J = 0.2, t_n/\tau = 2^8$, the distribution can be fit by the quadratic curve.

In the semi-classical theory introduced by Sachdev, correlation functions are estimated from the classical trajectories of quasi-particles [43]. To connect the quasi-particle propagation to the relaxation of the correlation functions, we calculate a spin-spin correlation function by using Wick's theorem. We consider the time dependence of a spin-spin correlation defined as

$$C_l(t) = \langle x | \hat{\sigma}^x_{L/2-l/2}(t) \hat{\sigma}^x_{L/2+l/2}(t) | x \rangle . \tag{2.25}$$

At the initial time, no transverse field is applied to the system, and the state, $|x\rangle$, is in one of the degenerate ground states, giving $C_l(0) = 1$. At $t = 0$, the transverse field is suddenly switched to a finite value with temporal fluctuation. The quasi-particle propagates super-diffusively for a certain time intervals in the short time scale, and its dynamics becomes diffusive in the long time scale. From the viewpoint of the semi-classical theory, the relaxations of the correlation functions are expected to have the same features as those of the quasi-particle propagation.

The correlation function can be written in the Majorana representation as

$$\langle x | \hat{\sigma}^x_i(t) \hat{\sigma}^x_j(t) | x \rangle \propto \langle x | \hat{\gamma}_{2i}(t) \hat{\gamma}_{2i+1}(t) \cdots \hat{\gamma}_{2j-1}(t) | x \rangle . \tag{2.26}$$

Wick's theorem then enables us to calculate $C_l(t)$ by the Pfaffian $\mathrm{Pf}[\mathsf{X}(t)]$, where the skew matrix

$\mathsf{X}(t)$ is defined by

$$\mathsf{X}_{ij}(t) = \begin{cases} 0 & (i=j) \\ \langle x|\, \hat{\gamma}_i(t)\hat{\gamma}_j(t)\, |x\rangle & (i \neq j) \end{cases} . \tag{2.27}$$

Figure 2.7 shows numerical results of the correlation function for several time intervals τ. Since the decay of the spin-spin correlation function over time is expected to be

$$C_l(t) \sim \mathrm{e}^{-bt^a}, \tag{2.28}$$

I calculate the exponent a by linear fitting by the least square method. After the long time-evolution, the value of a for $\tau/2\pi = 1.2$ approaches to the same value as for the other τ. The exponent $a = 0.724$ for $\tau/2\pi = 1.2$, while $a \sim 0.6$ for the other τ in the short time scale. These exponents a are close to the dynamical exponents $1/z(t)$, which are depicted in the inset of Fig. 2.7, in the short time scale, $\ln(t/2\pi) \lesssim 3$.

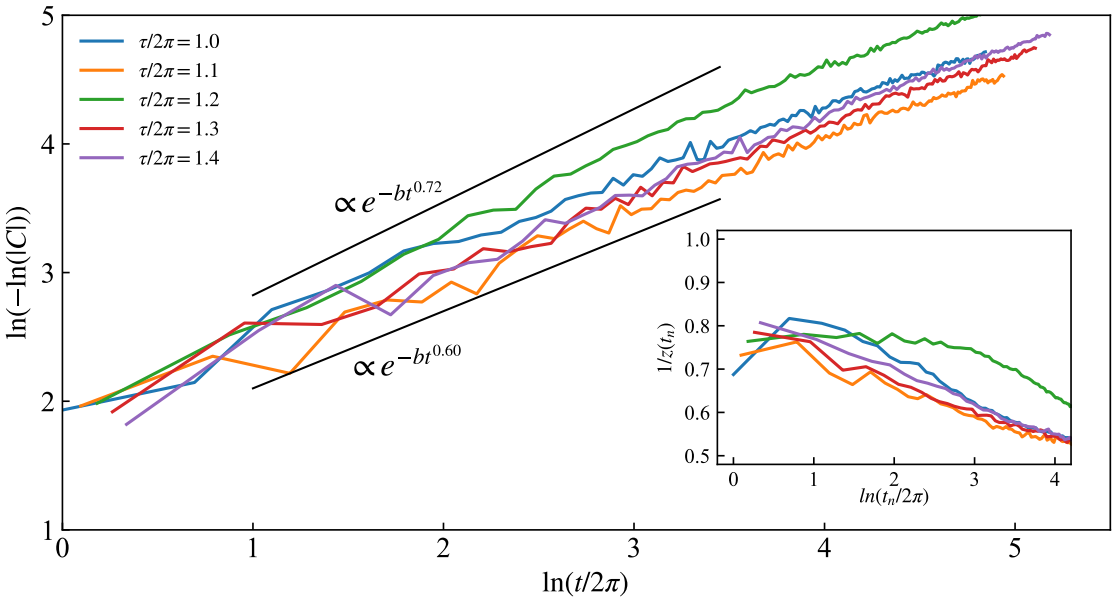

Fig. 2.7 Time dependence of the spin-spin correlation function with $L = 1024$, $l = 510$, $J = 1$, $A_J = 0.5$, $h = 1$, $N_{\mathrm{samp}} = 1000$ and $\tau/2\pi = 1.0 - 1.4$. The inset depicts the time-dependence of the dynamical exponents for the same setting as depicted in Fig. 2.5(a).

I calculate the dynamics of the bipartite entanglement entropy (EE) in the following way. For free fermionic systems

$$\hat{H} = \sum_{ij} \hat{c}_i^\dagger A_{ij} \hat{c}_j + \frac{1}{2}\hat{c}_i^\dagger B_{ij} \hat{c}_j^\dagger + \mathrm{H.c.}, \tag{2.29}$$

the EE is given from a partial matrix of fermion-fermion correlation functions [45, 46]. The matrix of correlation functions $\mathsf{F}(t)$ is defined as

$$\mathsf{C}_{\mu\nu}(t) = \langle z|\, \hat{\gamma}_\mu(t)\hat{\gamma}_\nu(t)\, |z\rangle\,, \tag{2.30}$$

where $|z\rangle$ denotes a state that all spins direct to the $+z$ direction, and $\hat{\gamma}_\mu$ is a Majorana fermion operator at site $\mu = 1, \cdots, 2L$. A matrix $\mathsf{F}'_{\mu\nu} = -\mathrm{i}\mathsf{C}'_{\mu\nu} + \mathrm{i}\delta_{\mu\nu}$ has eigenvalues $\mathrm{i}\lambda_\mu$. Here, the prime denotes limitation of the matrix into a subsystem A. $\{f_\mu = (1+\lambda_\mu)/2\}$ is entanglement spectrum, and the EE is calculated as

$$S = -\sum_{\mu \in A} f_\mu \log f_\mu. \tag{2.31}$$

I show the bipartite EE $S(t)$ in Fig. 2.8. The system size and the interval of the random field are set to 500 and $\pi/2$, respectively. To extract the exponent of the EE, I plot $S(t)$ in the log-log scale in Fig. 2.8(b). The slope corresponds to the exponent of $S(t)$ (see dashed lines). For $A_J = 0$, one can find that $S(t)$ decrease around $t/2\pi = 100$, which is thought the effect of the edges of the system. The exponent for $A_J = 0$ is ~ 0.79 (super-diffusive). For $A_J = 0.3, 0.5$, one can find that the exponent shifts from ~ 0.79 to ~ 0.518. For $A_J \geq 0.7$, the clear shift of the exponent can not be found. The time-evolution is also consistent with the estimation of the Sachdev's semi-classical theory.

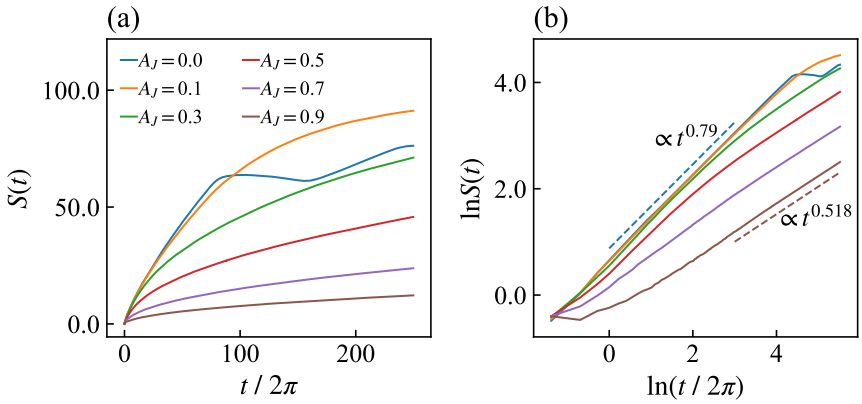

Fig. 2.8 (a) Time evolution of half chain entanglement entropy for $A_J = 0 - 0.9$. The system size and the interval of the random field are fixed $L = 500$ and $\tau = \pi/2$, respectively. (b) Log-log plot of the entanglement entropy. For $A_J = 0$, the exponent is ~ 0.79 (see blue dashed line). For $A_J = 0.3, 0.5$, the exponent shifts from 0.79 to 0.518 (see brown dashed line). For $A_J \geq 0.7$, the clear shift of the exponent can not be found.

2.5 Theory of stroboscopic eigenvectors

In this section, we review the theory of stroboscopic eigenvectors as adapted for the TFIM by Roósz [60], and I extend the theory to that for the QP-TFIM. The key to understanding the above results is to grasp how an eigenvector of $\mathsf{H}_\pm$ can be written with eigenvectors of $\mathsf{H}_\mp$. For the TFIM, the eigenvectors of $\mathsf{H}_\pm$ are spanned by those of $\mathsf{H}_\mp$ with a simple relation, which leads to the super-diffusive quasi-particle propagation. For the QP-TFIM, the finite quasi-periodicity makes the overlap complex, and this lack of the simple relation of overlap between the eigenvectors of H_+ and H_- leads to the diffusive propagation in the long time scale for any interval.

2.5.1 Case of TFIM

The binary and temporally random fields are regarded as randomly choosing either O_+ or O_- at each time step as a time-evolution operator. Since an eigenvector of O_+ is generally not an eigenvector of O_-, after the operation of O_- to an eigenvector of O_+, an eigenvector is no longer an eigenvector of both O_+ and O_-. After the random operations of $\mathsf{O}_\pm$, the propagation becomes diffusive. In the Roósz's theory, if one of the eigenvectors of H_+ is an eigenvector of both O_+ and O_-, then it survives even after the random operations of $\mathsf{O}_\pm$. I review this theory more precisely below.

In this section, H_s and H_{-s} denote the matrix representations of the Hamiltonians, where s represents the sign of $h(t)$. Since the TFIM in one dimension and in the periodic boundary condition can be solved exactly, the relation between eigenvectors of H_s and H_{-s} is given by

$$\boldsymbol{u}_\mu^s = c_{\nu\mu}\boldsymbol{u}_\nu^{-s} + c_{\bar{\nu}\mu}\boldsymbol{u}_{\bar{\nu}}^{-s}. \tag{2.32}$$

Here, $\boldsymbol{u}_\mu^s$ is the μth eigenvector of H_s, and $c_{\nu\mu} = (\boldsymbol{u}_\nu^{-s}, \boldsymbol{u}_\mu^s)$, where $(\cdot,\cdot)$ is an inner product defined as $(\boldsymbol{a},\boldsymbol{b}) = \sum_n a_n^* b_n$. The eigenvalues corresponding to $\boldsymbol{u}_\mu^{\pm s}$ are denoted by $\epsilon_\mu^{\pm s}$. $\overline{\mu}$ denotes the serial number of the eigenvector with eigenvalue $\epsilon_{\overline{\mu}}^{\pm s} = -\epsilon_\mu^{\pm s}$.

The correlation functions in Eq. (2.13) can be written in linear combinations of $\boldsymbol{u}_\mu^s$. The time-evolution is performed by random operations of O_s or O_{-s} as in Eq. (2.3). Now, I test whether $\boldsymbol{u}_\mu^s$ survives under the operation of both O_s and O_{-s}. The operation of $\mathsf{O}_s = \mathrm{e}^{-\mathrm{i}\mathsf{H}_s\tau}$ does not change the eigenvector itself. In contrast, $\mathsf{O}_{-s} = \mathrm{e}^{-\mathrm{i}\mathsf{H}_{-s}\tau}$ operates nontrivially on $\boldsymbol{u}_\mu^s$ as

$$\mathsf{O}_{-s}\boldsymbol{u}_\mu^s = \mathrm{e}^{-\mathrm{i}\epsilon_\nu^{-s}\tau}c_{\nu\mu}\boldsymbol{u}_\nu^{-s} + \mathrm{e}^{\mathrm{i}\epsilon_\nu^{-s}\tau}c_{\bar{\nu}\mu}\boldsymbol{u}_{\bar{\nu}}^{-s}. \tag{2.33}$$

Here, if a condition

$$\epsilon_\nu^{-s}\tau = m_{-s}\pi,\ m_{-s} = 1, 2, \cdots, \tag{2.34}$$

is satisfied, $\boldsymbol{u}_\mu^s$ is also an eigenvector of the time evolution operator O_{-s}. Note that $\boldsymbol{u}_\mu^s$ is still not an eigenvector of H_{-s}. I refer such an eigenvector of both O_+ and O_- as a stroboscopic eigenvector from now.

For $\tau < \pi/2$, the Hamiltonian of the TFIM does not have stroboscopic eigenvector. On the other hand, for $\tau \geq \pi/2$, the Hamiltonian has stroboscopic eigenvector. The reason is that the energy spectrum is zero at $|\epsilon| \geq 2$ as in Fig. 2.9(a). The correlation function includes the components of the eigenvectors satisfying the condition for τ, which are never disturbed by the binary and temporally random field. Such eigenvectors that survive under the random operation contribute to the super-diffusive propagation of the quasi-particles.

2.5.2 Theory for QP-TFIM

For the QP-TFIM, I obtain the result that the super-diffusive propagation disappears in the long time scale for any interval τ. Here, I attempt to extend Roósz's theory to that for the QP-TFIM.

In the presence of the quasi-periodicity, Eq. (2.32) does not hold. For the QP-TFIM, more than

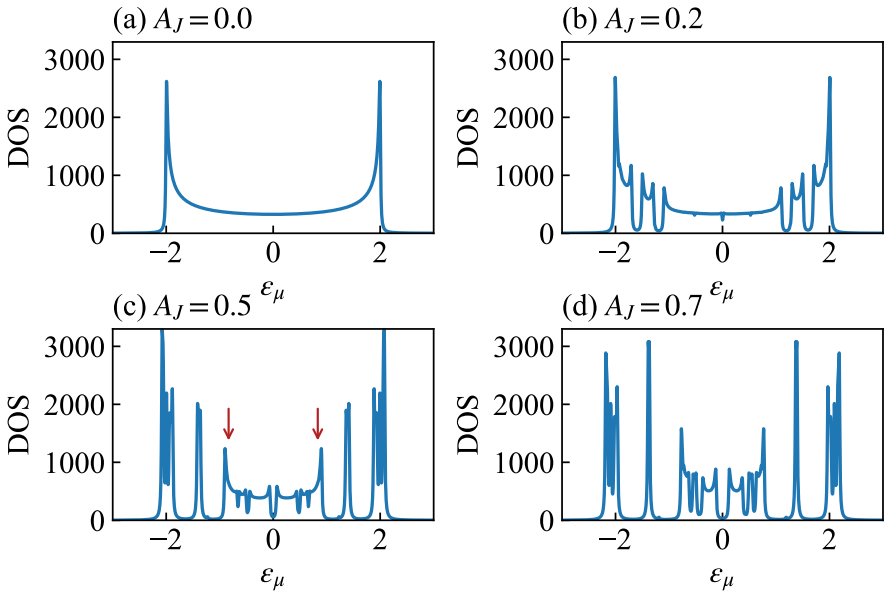

Fig. 2.9 Density of states (DOS) of the QP-TFIM for $A_J = 0, 0.2, 0.5, 0.7, 1$. The other Hamiltonian parameters are set as $J = h = 1$, $L = 2048$. At $A_J = 0$ (corresponding to the TFIM), the DOS has no gap and spans from -2 to $+2$. For the finite A_J, the DOS has gapes. The width of the gapes become wider as A_J increases. The red arrows in (c) denotes peaks corresponding to $\epsilon_\mu = \pm 0.833$.

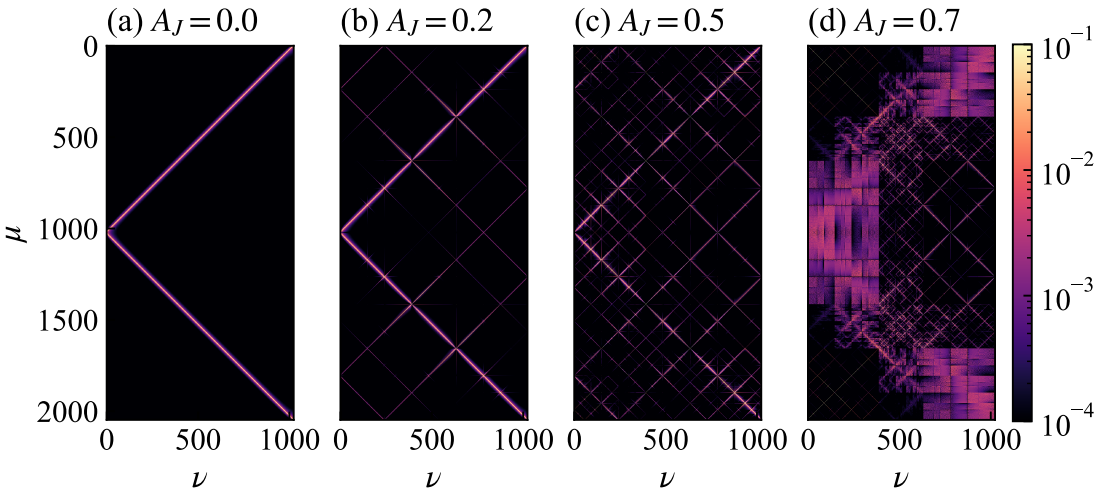

Fig. 2.10 Overlap between the eigenvectors of H_+ and H_-. The vertical axis μ and horizontal axis ν represent the numbers of eigenvectors of H_+ and H_-, respectively.

two pairs of the eigenvectors are required to describe the eigenvectors of the other Hamiltonian. To confirm this, I define overlap between the eigenvectors of H_s and H_{-s} as

$$M_{\mu\nu} := \left|(\boldsymbol{u}_\mu^s, \boldsymbol{u}_\nu^{-s})\right|^2 + \left|(\boldsymbol{u}_\mu^s, \boldsymbol{u}_{\bar{\nu}}^{-s})\right|^2. \tag{2.35}$$

Here, $M_{\mu\nu}$ quantifies how $\boldsymbol{u}_\mu^s$ is spanned by the pairs of $\boldsymbol{u}_\nu^{-s}$. The numerical result of $M_{\mu\nu}$ is shown in Fig. 2.10. For the TFIM($A_J = 0.0$), a single eigenvector $\boldsymbol{u}_\mu^A$ has an amplitude only for a certain ν. This indicates that $\boldsymbol{u}_\mu^s$ requires only the pair $\{\boldsymbol{u}_\nu^{-s}, \boldsymbol{u}_{\bar{\nu}}^{-s}\}$ to be spanned in the eigenbasis $\{\boldsymbol{u}_\nu^{-s}\}$. Introducing the quasi-periodicity creates fine structures in addition to the simple line obtained for the TFIM. Such structures becomes smeared as A_J increases. For the result, I can confirm that more than two pairs $\{\boldsymbol{u}_\nu^{-s}, \boldsymbol{u}_{\bar{\nu}}^{-s}\}$ are required to span an eigenvector $\boldsymbol{u}_\mu^s$ in the QP-TFIM.

Consider the simplest case, where $\boldsymbol{u}_\mu^s$ is spanned by only two pairs, $\{\boldsymbol{u}_\nu^{-s}, \boldsymbol{u}_{\bar{\nu}}^{-s}\}$ and $\{\boldsymbol{u}_\lambda^{-s}, \boldsymbol{u}_{\bar{\lambda}}^{-s}\}$:

$$\boldsymbol{u}_\mu^s = c_{\nu\mu}\boldsymbol{u}_\nu^{-s} + c_{\bar{\nu}\mu}\boldsymbol{u}_{\bar{\nu}}^{-s} + c_{\lambda\mu}\boldsymbol{u}_\lambda^{-s} + c_{\bar{\lambda}\mu}\boldsymbol{u}_{\bar{\lambda}}^{-s}. \tag{2.36}$$

The eigenvector operated byO_{-s} reads

$$\begin{aligned}\mathsf{O}_{-s}\boldsymbol{u}_\mu^s &= c_{\nu\mu}\mathrm{e}^{-\mathrm{i}\epsilon_\nu^{-s}\tau}\boldsymbol{u}_\nu^{-s} + c_{\bar{\nu}\mu}\mathrm{e}^{\mathrm{i}\epsilon_\nu^{-s}\tau}\boldsymbol{u}_{\bar{\nu}}^{-s} \\ &\quad + c_{\lambda\mu}\mathrm{e}^{-\mathrm{i}\epsilon_\lambda^{-s}\tau}\boldsymbol{u}_\lambda^{-s} + c_{\bar{\lambda}\mu}\mathrm{e}^{\mathrm{i}\epsilon_\lambda^{-s}\tau}\boldsymbol{u}_{\bar{\lambda}}^{-s}.\end{aligned} \tag{2.37}$$

Here, even if either $\mathrm{e}^{\pm\mathrm{i}\epsilon_\nu^{-s}\tau}$ or $\mathrm{e}^{\pm\mathrm{i}\epsilon_\lambda^{-s}\tau}$ equals to ± 1, the other one is impossible to be ± 1. I omit the case of $\epsilon_\lambda^{-s} = n\epsilon_\nu^{-s},\ n \in \mathbb{Z}$ in this study. In this way, $\boldsymbol{u}_\mu^s$ is impossible to be an eigenvector of O_{-s} in the case that $\boldsymbol{u}_\mu^s$ is spanned by multiple pairs $\{\boldsymbol{u}_\nu^{-s}, \boldsymbol{u}_{\bar{\nu}}^{-s}\}$.

In the TFIM, the quasi-particle avoids the diffusive propagation even in the long time scale. The reason is that the eigenvector survives under the random operations of $\mathsf{O}_\pm$ because of the simple overlap shown in Fig. 2.10. In contrast, the QP-TFIM has complex overlap than the TFIM, and there is no stroboscopic eigenvector. Thus, in the QP-TFIM, the quasi-particle propagation relaxes to the diffusive value after the long time-evolution.

The analytically obtained relation in Eqs. (2.32) and (2.36) controls the speed of the relaxation of the dynamical exponent as shown in Fig. 2.5. For small A_J, the overlap in Fig. 2.10 still has clear lines, which indicates that the first and second terms are dominant in Eq. (2.36), whereas the other terms are much smaller. Since $\boldsymbol{u}_\mu^s$ is similar to the eigenvector of O_{-s} for small A_J, the single operation of O_{-s} transforms $\boldsymbol{u}_\mu^s$ to a vector slightly different from $\boldsymbol{u}_\mu^s$. Such small changes of the eigenvector accumulate through the random operations of $\mathsf{O}_\pm$, and finally the eigenvector looses its coherence, that is, is decohered in the long time scale. For large A_J, the third, fourth, and subsequent terms are not negligible to the first and second terms. Thus, a single operation of O_{-s} transforms $\boldsymbol{u}_\mu^s$ to a vector greatly different from $\boldsymbol{u}_\mu^s$. This is an explanation to the dependence of the relaxation speed on the strength of the quasi-periodicity.

I also obtain that the dynamical exponent for $\tau/2\pi = 1.2$ and 2.4 relaxes more slowly than those for for the other intervals. The slow relaxation can be explained by the modification in eigenenergy structures as A_J increases in Fig. 2.9. The corresponding eigenenergies with $\tau/2\pi = 1.2$ and 2.4 are

$\epsilon_{-s} = 0.833$ for $m_{-s} = 2$ and $m_{-s} = 4$, respectively. One can find that small peaks at $\epsilon_{-s} = \pm 0.833$ in Fig. 2.9. In this way, the condition is partially satisfied for $\tau/2\pi = 1.2$ and 2.4, and the super-diffusive propagation occurs only for $\tau/2\pi = 1.2$ and 2.4.

2.6 Conclusion

In this study, I have analyzed the decoherence of the domain wall's propagation in the quasi-periodic Ising model under binary and temporal random field. The field takes only two vales $\pm h$ (being binary) and fluctuates its value at every time step whose interval is fixed to τ. I have used the stroboscopic time evolution. I found that, for finite quasi-periodicity $A_J \neq 0$, the domain wall's propagation is super-diffusive in short time scale for the certain intervals while it relaxes to being diffusive in long time scale. From the discussion in the stroboscopic eigenvectors of the time evolution operators, the result attributes to the vanishment of the stroboscopic eigenvectors. In other words, for $A_J \neq 0$ any eigenvector is not robust against the binary and temporal random field.

The propagation of the domain walls determines the dynamics of correlation functions and entanglement entropy in free fermionic systems including the system in question. I have confirmed that the spin-spin correlation function and the half chain entanglement entropy have the same dynamical exponent as the propagation of the domain walls. The domain walls propagating ballistically (or super-diffusively) bounce at the edges, and it makes the entanglement entropy oscillated. On the other hand, in the system with the diffusive domain walls, the entanglement has no oscillation within the temporal range I calculated. From viewpoint of the relaxation to equilibrium states, it is interesting to study a question whether the system where the domain walls propagates super-diffusively can relaxes to equilibrium. In general, isolated systems consisting of free particles have no ability to relax to thermal equilibrium by their own time evolution because of their integrability. However, systems with free particles under temporal randomness are not the case. Whether does such systems relax to thermal equilibrium?

Another perspective is studying the effect of many-body interactions to the propagation of the domain walls. The semi-classical framework works to describe the relaxation of the correlation functions in free particle systems like the TFIM. A next step could be testing the semi-classical framework in the TFIM with weakly interacting term like a type of $\hat{\sigma}_i^z \hat{\sigma}_{i+1}^z$. The semi-classical framework is expected to be ruined in the many-body systems. How is the semi-classical framework ruined? If the semi-classical framework does not work, what is the alternative?

One of the main targets in studies of relaxation to thermal equilibrium is periodically driven systems (so called Floquet systems). In such systems, statistical analysis using Floquet energies and Floquet Hamiltonian works to diagnose the ability to relaxes to the thermal equilibrium. Since the system in question have no periodicity in the time evolution, the analysis is not applicable to the system under temporal randomness. One of the possible future perspectives is studying statistical methods to diagnose the ability to relax to thermal equilibrium.

CHAPTER 3

Ergodicity breaking crossover in Rydberg atoms

In this section, I describe numerical study on ergodicity breaking in the anisotropic Heisenberg model with long range interactions. This study is inspired by an experiment that ergodicity breaking may be observed in thousands of Rydberg atoms.

3.1 Introduction

A macroscopic system prepared in a non-equilibrium state relaxes to a thermal equilibrium state characterized by few parameters like temperature and pressure. The relaxation process is called as "thermalization". Figure 3.1 illustrates a temporal profile of thermalization of an observable. If a system avoids thermalization, it implies that statistical mechanics no longer predicts an expectation value of an observable in thermal equilibrium. Thermalization is natural in quantum systems coupling with environments (baths). Energy and particles in the systems are exchanged with the environments until these densities in the systems converge to those in the environments. In contrast, whether isolated quantum systems (quantum systems isolated from environments) displays thermalization is a more subtle question because the time evolution in these systems is purely of quantum mechanics and is recursive [42]. The attempts to solve this problem has begun from the beginning of last century [76]. After studies for long time, thermalization is thought to be realized in a majority of isolated quantum systems. What is a condition for thermalizing in many-body systems?

Studies on thermalization has a long histroy since von Neumann has firstly proposed the quantum ergordic theorem in 1929 [76]. Until now, there have been discussions based on typicality and random matrix theory [77–79]. One of the most promising conditions is the eigenstate thermalization hypothesis (ETH) [79–81]. The detail description of ETH is provided in Appendix B. A direct conclusion from ETH is that, if a given system satisfy ETH, observables after long time evolution are same as expecation values predicted by microcanonical ensemble, i.e., the system thermalizes. However, there is no rigorous proof that any quantum system satisfies ETH. Indeed, integrable models (e.g. Heisenberg chain and Hubbard model in one dimension) and systems exhibiting many-body quantum scar or many-body localization (MBL) are known to violate ETH [82–85].

In the following subsection, I introduce the many-body localization, which is a target in this study. Before going to next subsection, I note a crucial terminology in this study. I denote the ability to satisfy ETH as ergodicity. Unlike the ergodic theory in classical mechanics, ergodicity does not relate to the justification of the principle of equal weight. Since systems displaying MBL do not have

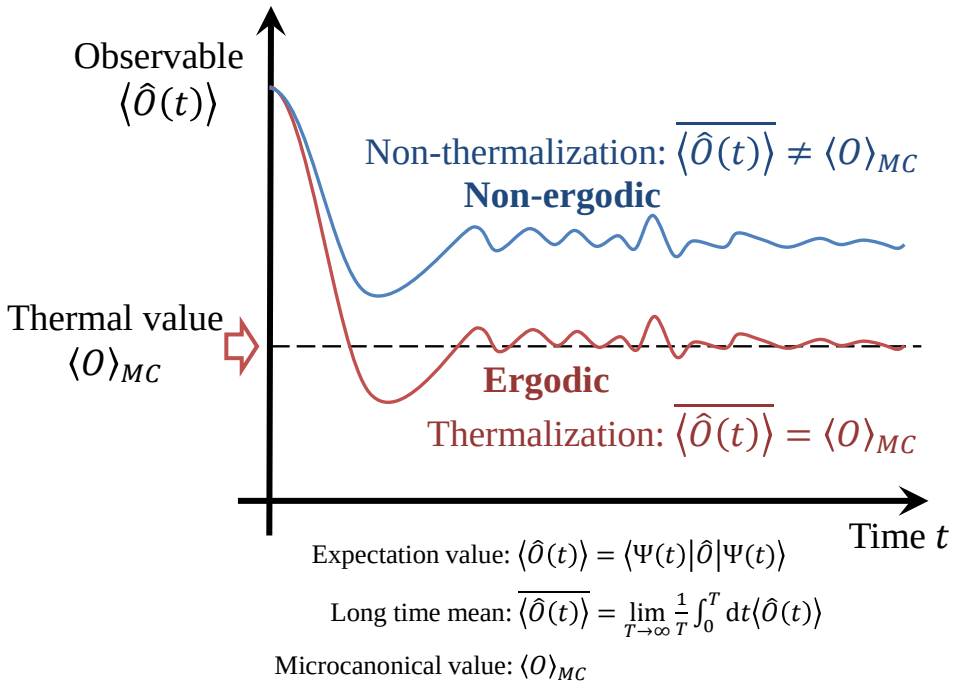

Fig. 3.1 Schematic figure of thermalization in isolated quantum systems.The red line and the blue line indicate the dynamics of observables in non-ergodic and ergodic systems, respectively.

ability to thermalize, these systems are non-ergodic. The detail description about thermalization and ETH is in Appendix B.

3.1.1 Many-body lcoalization

One of the most well-known examples to avoid thermalization is many-body localization (MBL) [16–18]. MBL emerges in many-body quantum systems under spatial randomness (quenched disorder), for example anisotropic Heisenberg chain with random local fields. Although MBL is just an extension of Anderson localization, it has been gathered much attentions in last two decades partially due to the progress in experimental techniques in artificial quantum systems isolated from environments [19–27]. Until now, some universal properties of MBL has been uncovered, for example no transport, Poissonian level statistics, area-law entanglement and logarithmic growth of entanglement [28, 29, 34, 47, 84, 86].

An issue attracting the researchers' attention is the ergodic-nonergodic transition [86]. MBL (non-ergodicity) emerges under sufficiently strong disorder while ergodicity emerges under weak disorder (except for integrable parameters). The ergodic-nonergodic transition is thought a new type of phase transition unlike conventional phase transitions. It is often expressed as an "eigenstate phase transition" because through the transition all eigenstates dramatically changes properties of their eigenstates, for example entanglement structures [36, 87]. In the nonergodic regime, the entanglement entropy of the subsystem A is proportional to the surface area in A (follows the area-law). On the other hand, in the ergodic regime, the entanglement entropy in A is proportional to the volume of A. At the critical point, the variance of the entanglement entropy reaches to the maximum [88]. From renomarlization groups [89], the entanglement entropy for a small subsystem shows discontinuous

jump at the critical point.

The ergodic-nonergodic transition has been studied by numerical calculations, phenomenological theories and experiments. Since studying ergodic-nonergodic transition has technologically difficulties, many questions are remained open. Some numerical studies devoted for determining the critical point by using the exact diagonalization (ED) method [36, 87]. At the critical point, the systems are invariant to changing the length scale. The correlation length plays a central role in finding the critical point. One of the possible definitions of the correlation length is a power-law type as

$$\xi = \frac{1}{|W - W^*|^\nu}, \tag{3.1}$$

where W^* is the critical disorder strength. Since the exponent ν is pointed out to violate the Harris bound $\nu \geqslant 2$ [90], the validity of the power-law type correlation length is questionable. Recently, another type of transition has been proposed by renormalization group approaches [91–93]. That type of the transition is called as Berezinski-Kosterlitz-Thouless (BKT) type, whose correlation length is defined as

$$\xi = \exp\left[\frac{b_\pm}{\sqrt{|W - W^*|}}\right]. \tag{3.2}$$

Here, $b_\pm$ are constant and may be different in both sides of the transition. The statement has been obtained by a scaling theory based on thermal avalanche (see below), and it has been verified numerical studies by ED [94, 95]. Recent studies in the ED calculation support that the critical point linearly shifts with a system size. The fact indicates two possible scenarios. One is what has been thought as the ergodic-nonergodic transition is actually a crossover. The other is that the critical point is quite large in thermodynamic limit (large size limit). The type of the ergodic-nonergodic transition and the critical point are still lack of conclusive evidence, and determining them is undergoing subject.

The most basic question, whether MBL exists in thermodynamic limit, is most challenging for following reasons. In numerical methods mainly based on the ED calculation, the accessible system size is highly limited (typically the maximum size is around 20 spins with $S = 1/2$). In experiments, the accessible time is too short to wait thermalization (typical time to thermalize is the exponential of the system size). One of the possible scenarios is that, in thermodynamic limit, MBL can exist in one dimension whereas cannot in dimensions more than one. This is obtained from a theory based on ETH and local integrals of motion (LIOMs), which is called as thermal avalanche.

3.1.2 Local integrals of motion

Since many-body systems under quenched disorder are non-integrable, there is no explicit symmetry (no conserved quantity). Nevertheless, a system displaying fully MBL has conserved quantities named as local integrals of motion (LIOMs) [30, 48, 96, 97]. The universal properties in MBL can be captured by LIOMs. For spin systems, LIOMs are dressed spin operators defined as $\hat{\tau}_i^z = \sum_j C_{ij}\hat{\sigma}_j^z$ with bare spin operators $\hat{\sigma}_j^z$. Since the weight C_{ij} exponentially decays with distance from i, LIOMs

are quasi-local operators. By using LIOMs, the MBL Hamiltonian can be rewritten as

$$\hat{H} = \sum_i h_i \hat{\tau}_i^z + \sum_{ij} J_{ij} \hat{\tau}_i^z \hat{\tau}_j^z + \sum_{ijk} K_{ijk} \hat{\tau}_i^z \hat{\tau}_j^z \hat{\tau}_k^z \cdots . \tag{3.3}$$

Apparently, since the Hamiltonian commutes LIOMs $\hat{\tau}_i^z$, the LIOMs are conserved through time evolution of its Hamiltonian.

3.1.3 Thermal avalanche

An important conclusion obtained from combination of LIOMs and ETH is thermal avalanche [98–100]. Thermal avalanche predicts the behavior of MBL in thermodynamic limit. Due to the property of spatial randomness, disordered systems in thermodynamic limit are inevitable to include two types of local regions: strongly disordered regions and weakly disordered regions. The former regions are regarded as in fully MBL and can be described by LIOMs. On the other hand, the latter regionsare regarded as ergodic and follows ETH. In Ref. [98], a situation where a MBL subsystem is in contact with a ergodic subsystem was considered. As a result, it was found that the ergodic subsystem makes the MBL subsystem unstable. In thermodynamic limit, such destabilization possibly occur sequentially, and the whole systems can reach to being ergodic. Whether MBL survives through the destabilization in thermodynamic limit depends on its spatial dimension. Specifically, in one dimension, MBL may survive even in thermodynamic limit whereas never in dimensions higher than one.

Until now, the existence of MBL in thermodynamic limit in one dimension has been verified at some extents via various numerical and experimental studies. On the other hand, the existence of MBL in dimensions higher than one is still controversial because some numerical and experimental studies insist that MBL exists in two or three dimensions.

3.1.4 MBL in two dimensions

In spite of the prediction that no MBL exist in two dimensions in thermodynamic limit, some numerical and experimental studies argue evidences of MBL in two dimensions [21, 26, 27, 101–107]. However, these results are controversial because there are methodological bottlenecks. When one observes relaxation of observables in experiments, time to take the relaxation is estimated much longer than time that one can access. Since a typical time to thermalize in many-body quantum systems is estimated as an exponential of system sizes, one cannot distinguish whether the system avoids thermalization or the system has not yet reached thermalization. For the same reason, results in numerical studies based on time evolution by tensor networks are also questionable. Some numerical studies are based on static ways whereas these methods, for example tensor networks, are more valid in the MBL regime but less in the ergodic regime. In other words, these methods are biased to the MBL regime. Thus, these studies are not suitable to provide information of the ergodic-nonergodic transition.

One of the most faithful method is the exact diagonalization (ED), which has played an important role in one-dimensional MBL studies. ED is a calculation method to compute all eigenstates and the corresponding eigenenergies without any approximation. However, the accessible system size is highly limited to ~ 20 spins with $S = 1/2$. It is standard that the behavior in thermodynamic limit

is estimated by extrapolating the trend with respect to small system sizes. Of course, one cannot deny the possibility that the extrapolation differs from a true behavior. Nonetheless, the extrapolation provides important information of the MBL behavior in thermodynamic limit because methods that one can use for MBL problem is limited.

The reliability of the extrapolation of the trend with respect to the system size is expected to be improved if one can calculate results for various system sizes. Since, in one dimension, the system size is adjustable with a unit of one spin, the extrapolation to the system is reliable at some extent. Meanwhile, it is less reliable in two dimensions because the variety of system sizes can be calculated in two-dimension regular lattice systems is limited more than in one dimension. One of the standard models in MBL studies is Heisenberg model with disordered fields, whose lattice is square. The number of all spins in such a system increases as L^2 with the number of spins in the one side L. Considered the maximal system size by ED, only 3×3 or 4×4 lattices are accessible in ED. (If including systems with square length, one can access more system sizes.) For this reason, in systems with regular lattices, extrapolation based on ED is unreliable (except constrained quantum systems like quantum dimer model [106, 107]).

However, if there no lattice structure, one can calculate systems with more various sizes, and the extrapolation is more reliable even in two dimensions. I am inspired by recent experiments and adopt a system with no lattice structure [26, 27]. The experiment is implemented in the Rydberg atoms, which are randomly distributed and are subject to the Rydberg blockade. A Rydberg atom can be regarded as a two level system (spin) during the experiment, and the whole system effectively realizes the anisotropic Heisenberg model with interaction decaying with distance between spins (van der Waals type of interaction). Due to such features, one can extrapolate the results more effectively.

In this study, I adopt the anisotropic Heisenberg model in two dimensions with van der Waals type of interaction, which is inpired by the experiment in the Rydberg atoms. The interaction is disordered due to the random distribution of the spins. Since the disorder strength in the system is unidentified, I start with defining the disorder strength. Then, I calculate ergodic indicators and estimate the critical disorder strength by differentiating the results of the indicators with respect to the disorder strength. Finally, I extrapolate the trend of the critical disorder strength and discuss whether MBL exists in the thermodynamic limit.

The rest of this chapter is organized as follows. In Sec. 3.2, I summarize a setting employed in the aforementioned experiment. In Sec. 3.3, I introduce a Hamiltonian in this study and describe a method to preparing the system. In Sec. 3.4, I define the disorder strength and check the validity. In Sec. 3.5, I define some ergodic indicators to distinguish the non-ergodic (MBL) regime from the ergodic regime, show the numerical results and obtain the critical disorder strength. In Sec. 3.6, I extrapolate the trend of the disorder strength with respect to the system size and discuss whether MBL exits in thermodynamic limit. Finally, I summarize this chapter in Sec. 3.7.

3.2 Avoiding thermalization in Rydberg atoms

References [26, 27] has studied the relaxation of the magnetization under time evolution in the Rydberg atoms. Inspired by the experiments, I analyze a spin model realized in the Rydberg atoms. Here, I review the basic properties in the Rydberg atoms and the experimental setting in the experiments [26, 27].

3.2.1 Basic properties of Rydberg atoms

Here, I provide basic properties of the Rydberg atoms [108]. Recently, the Rydberg atoms are utilized as a platform to simulate the dynamics of quantum many-body systems. The Rydberg atoms refer to atoms whose electronic states are pumped to excited states with the large principal quantum number. For the utility of quantum simulators, two excited states are used for computational states called as Rydberg states as in Fig. 3.2(b). The Rydberg atoms have large dipole moments, and the dominant interaction between them is the dipole-dipole interaction. Since the interaction decays with distances, it brings two different effects on the Rydberg atoms. In a short range, the interaction is so strong that the energy levels of the double excitation of the close two atoms are shifted as in Fig. 3.2(d). As a result, (unexcited) atoms near the Rydberg atoms are forbidden to be excited by microwaves with the same frequency. This effect is called as Rydberg blockade and works as an exclusion of the new Rydberg atoms from a certain range a Rydberg atom as in Fig. 3.2(c). On the other hand, in a long range, the dipole-dipole interaction works within the Rydberg states as the van der Waals interaction, which decays with r^{-6} with the distance of the Rydberg atoms r. The length scale to forbid the other atom excited into the Rydberg states is the blockade radius r_{b}. Within the range $r < r_{\mathrm{b}}$, the Rydberg blockade works, and otherwise the van der Waals interaction works but the Rydberg blockade does not.

3.2.2 Experimental setting

Preparation of the Rydberg atoms In Refs. [26, 27], the Rydberg atoms were prepared as follows. The authors prepared a gas of ^{87}Rb in their electronic ground state and trapped them by the optical dipole trap. To stop the motional degrees of freedom, they froze the atoms up to sufficiently low temperature. The motion of the atoms can be regarded stopped within the time scale of the experiments. After that, they applied the laser pulse to pump the electronic states of the atoms up to the $|\downarrow\rangle$ Rydberg state. To individually address two specific states, they continuously applied a magnetic field. A two-photon microwave was used to couple $|\downarrow\rangle$ and $|\uparrow\rangle$. The single-photon frequency was detuned from that of the intermediate state. As a result, the Rydberg atom can be considered as a system with two levels consisting from $\{|\uparrow\rangle, |\downarrow\rangle\}$, that is, a single spin with $S = 1/2$.

When the Rydberg atoms were excited, the Rydberg blockade effect prevented the (unexcited) atoms near by the Rydberg atoms from being excited to the Rydberg states. In this way, the Rydberg atoms were prepared at random positions and each Rydberg atom was apart from the others by more than r_{b} as in Fig. 3.2(c).

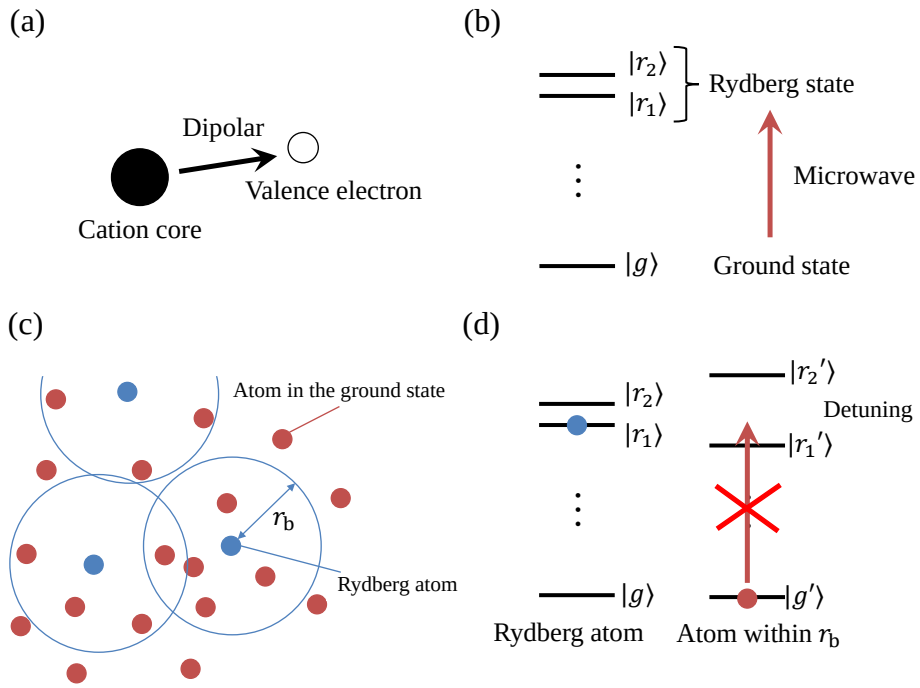

Fig. 3.2 (a) An excited atom with dipolar. (b) Energy level of an atom excited to the Rydberg states. (c) Rydberg blockade. The Rydberg atom prevents another excitation from the range of r_{b}. (d) Energy levels of the Rydberg atom and other atom near it. Due to the short range interaction, the Rydberg states in an atom are detuned by the excitation of the Rydberg atom.

Experimental protocol In the experiment [27], the time evolution of the magnetization in the effective spin states (the Rydberg states) in the ensemble of the Rydberg atoms has been observed. The experimental protocol to observe it is as follows. First, the initial state was prepared in $|{\rightarrow}\rangle^{\otimes N}$, where $|{\rightarrow}\rangle = (|{\uparrow}\rangle + |{\downarrow}\rangle)/\sqrt{2}$ and N is the number of the Rydberg atoms. Second, the system evolved under the anisotropic Heisenberg Hamiltonian with the van der Waals interaction and an external transverse field. The time evolution was taken for time t. Finally, the magnetization was observed. By repeating these process for different times t, they obtained the temporal profile of the magnetization in the system. The experimental protocol is summarized in Fig. 3.3(a).

Methodology to observe failure of thermalization The direct way to observe the failure of thermalization is comparing an expectation value of an observable to the corresponding thermal value predicted from statistical mechanics. It is possible in numerical studies. However, since there is no way to experimentally obtain the thermal value, it is impossible in experiments. In the experiment [27], the authors has adopted a method without using the thermal value. In the method, the mathematical property of ETH has been used. I summarize mathematical basics of thermalization in isolated quantum systems, and review the experimental method. The detail descriptions of thermalization in isolated quantum systems are provided in Appendix B.

Isolated quantum systems can be described by quantum mechanics. Let $|\psi(t)\rangle$ denotes an quantum state in an isolated quantum system at time t. Any quantum state can be decomposed into a linear combination of the eigenbasis of the Hamiltonian $\hat{H}$ as $|\psi(t)\rangle = \sum_\alpha \psi_\alpha(t)\,|\alpha\rangle$. The time evolution under Hamiltonian $\hat{H}$ is described by a time evolution operator $\mathrm{e}^{-\mathrm{i}\hat{H}t}$, and the state at time t is given

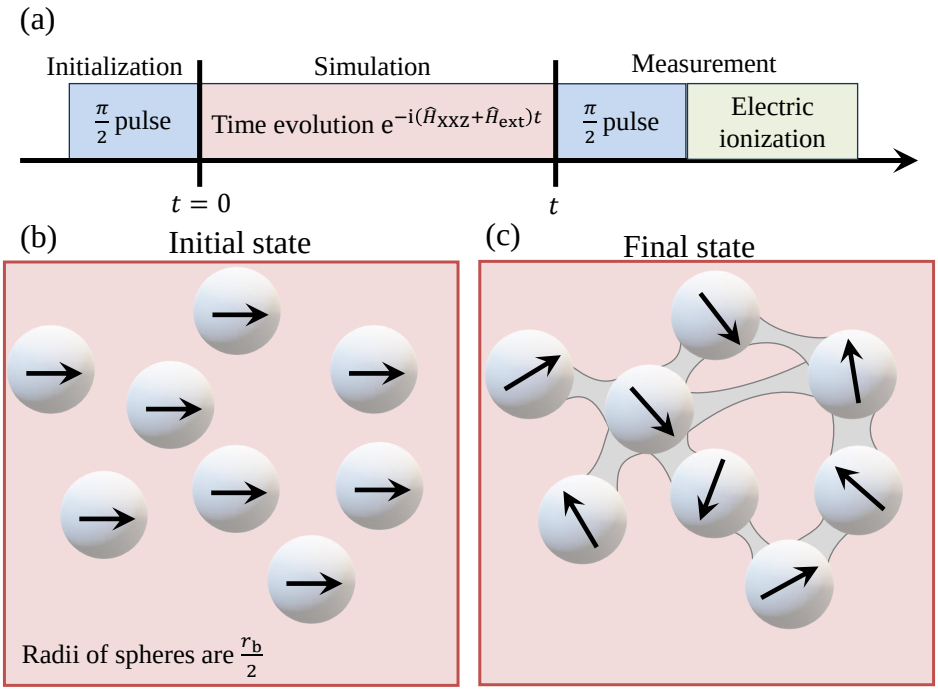

Fig. 3.3 (a) Experimental protocol. After initialization by a $\pi/2$ pulse, the system experiences time evolution during time t under Hamiltonian $\hat{H}_{\mathrm{XXZ}} + \hat{H}_{\mathrm{ext}}$. The evolved state is measured by applying a $\pi/2$ pulse and electric ionization. (b) Initial state of the experiment. All spins are fully polarized to $+x$ direction and are in a product state, which means that there is no entanglement. (c) Final sate of the experiment. If the system thermalizes, the system is no longer in a product state, and entanglement over some spatial scale grows due to the time evolution.

by

$$|\psi(t)\rangle = \sum_{\alpha} \psi_{\alpha} \mathrm{e}^{-\mathrm{i}E_{\alpha}t} |\alpha\rangle \,, \tag{3.4}$$

where an initial state $|\psi\rangle = \sum_{\alpha} \psi_{\alpha} |\alpha\rangle$ with $\psi_{\alpha} = \langle\alpha|\psi\rangle$, and E_{α} is the αth eigenenergy of $\hat{H}$. The expectation value of an observable $\hat{O}$ evolves as

$$\langle \hat{O}(t) \rangle = \langle \psi(t)| \hat{O} |\psi(t)\rangle = \sum_{\alpha,\beta} \psi_{\alpha}^{*} \psi_{\beta} \mathrm{e}^{\mathrm{i}(E_{\alpha}-E_{\beta})t} \langle\alpha| \hat{O} |\beta\rangle \,. \tag{3.5}$$

To test thermalization, one needs to take the long time limit $t \to \infty$. Instead of that, one can consider the long time average

$$\overline{O} = \lim_{T\to\infty} \int_{0}^{T} \mathrm{d}t \, \langle \hat{O}(t) \rangle, \tag{3.6}$$

which provides the expectation value in the long time limit. Since non-integrable systems have no degeneracy in the energy levels, the temporal integral vanishes unless $E_{\alpha} = E_{\beta}$. The long time average is reduced into the diagonal ensemble

$$\overline{O} = \sum_{\alpha} |\psi_{\alpha}|^2 \langle\alpha| \hat{O} |\alpha\rangle \equiv \langle \hat{O} \rangle_{\mathrm{DE}}. \tag{3.7}$$

If a system possesses the ability to thermalize, the long time average in Eq. (3.7) equals to the microcanonical ensemble (MCE)

$$\langle \hat{O} \rangle_{\mathrm{MCE}} = (\mathcal{D}_{E,\Delta E})^{-1} \sum_{|E-E_\alpha|<\Delta E} \langle \alpha | \hat{O} | \alpha \rangle . \tag{3.8}$$

The summation is taken over an energy shell whose center is E and width is ΔE, and $\mathcal{D}_{E,\Delta E}$ is the number of eigenstates within the energy shell. Thermalization is equivalent to $\overline{O} = \langle \hat{O} \rangle_{\mathrm{MC}}$, and its sufficient condition is ETH. If ETH holds, (i) a majority part of the probability distribution $|\psi_\alpha|^2$ is within the energy shell, and (ii) $\langle \alpha | \hat{O} | \alpha \rangle$ is approximately a smooth function of E_α.

In the experiment [27], the magnetization $\hat{S}^x = \sum_i \hat{S}^x_i$ is adopted as an observable, and the smoothness of $\langle \hat{S}^x(t) \rangle$ after relaxation as a function of the external field Ω is tested to check the properties (i) and (ii). If one find $\langle \hat{S}^x(t) \rangle$ after relaxation is not smooth as a function of Ω, the system is thought to avoid thermalization. However, there is a logical gap in checking (i) and (ii) via the smoothness of $\langle \hat{S}^x(t) \rangle$ with respect to Ω. This point has been verified by a numerical simulation in the system with 14 spins. In the numerical simulation, the expectation value does not thermalize for the strong disordered regime (small r_{b}) while it thermalizes for the weak disordered regime (large r_{b}). At the same time, the numerical simulation has checked that the expectation value has a cusp as a function of Ω for the strong disordered regime while does not for the weak disordered regime. The properties (i) and (ii) have also checked for these two regimes. (i) and (ii) are satisfied for the weak disordered regime whereas are not for the strong disordered regime. Thus, the smoothness of $\langle \hat{S}^x(t) \rangle$ with respect to Ω can be concluded as an indicator of thermalization. By the above method, the experiment [27] argues that failure of thermalization has been observed in the strong disordered Rydberg atoms.

3.2.3 Advantage of Rydberg atoms

The advantage when one numerically calculates the Rydberg atoms in ED calculation is the rich selectivity of the system sizes compared with models with square lattices.

The most orthodox model displaying MBL is the $S = 1/2$ Heisenberg model whose spins equidistantly locate at fixed positions. In one dimension, one can set the system size to arbitrary integers N. Current cluster computers can deal with systems with $N \lesssim 20$. In addition, when one tests the ergodicity in a given system, the system size is necessary to be sufficiently large, for $1/2$ spin systems, $N \gtrsim 10$. One can select the system size $N = 10 - 20$ in one dimension.

A natural extension of the one-dimensional Heisenberg model is the Heisenberg model with two-dimensional square lattice. One can select the system sizes from composite numbers. However, since the aspect ratio of the square lattices affects to the ergodicity for the small system sizes, the aspect ratio is essentially set to unit, i.e., the square-shaped square lattices are acceptable. Apparently, one can select square numbers $N = 4, 9, 16, 25, \cdots$. Additionally, one can also select $N = \sqrt{m^2 + n^2}$ with integers m, n. The latter corresponds to the tilted square lattice. The acceptable system sizes in the ED calculation are $N = 10, 13, 16, 17, 18$. The examples of the tilted square lattices are depicted in Fig. 3.4. In the tilted square lattice in the open boundary condition, sites around the edges have less

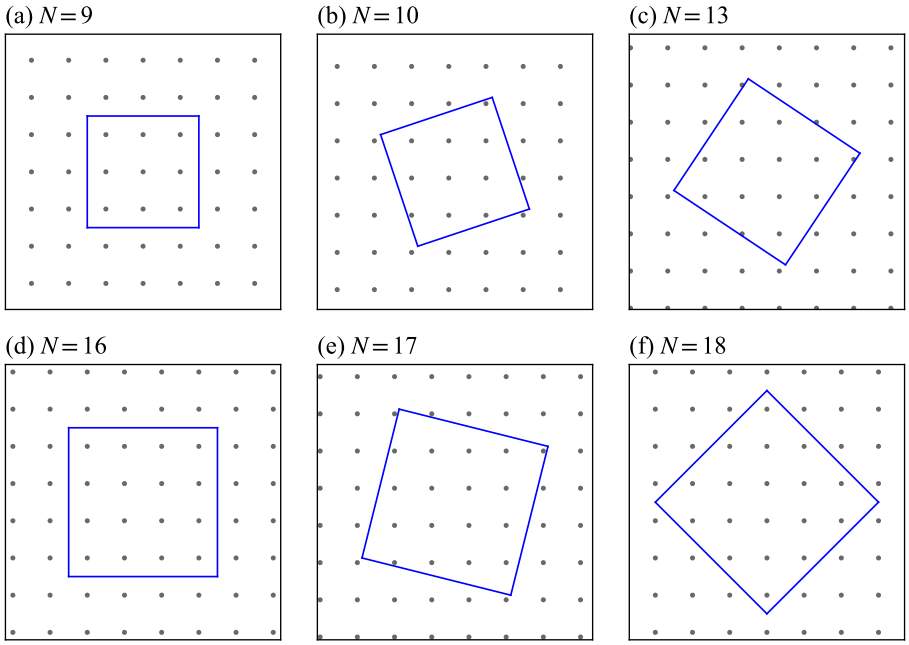

Fig. 3.4 Exemplary square lattices accessible in the ED calculation.

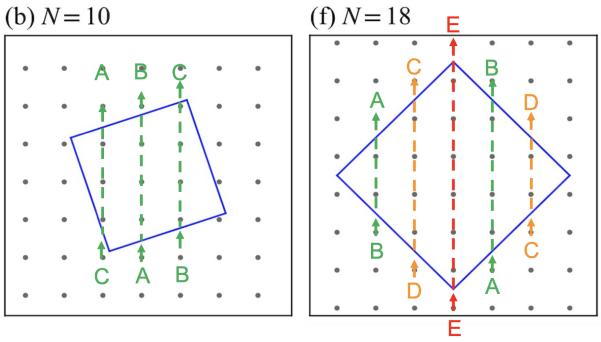

Fig. 3.5 Exemplary lattice geometries in the tilted square lattice in the periodic boundary condition.

bonds to the other sites, for example, for $N = 10$ the site at the top has only one bond as in Fig. 3.4 (b). This problem can be neglected by adopting the periodic boundary condition. The periodic boundary condition makes torus by connecting a side to the opposite side and all the sites equip same numbers of bounds. Instead, the lattice geometry in the tilted square lattices is more complex as in Fig. 3.5. Consider a path straightly running from a site in the periodic boundary condition. For $N = 9, 16, \cdots$, the path is closed to a single-winding loop. In the case of the tilted square lattices, the path is closed to a trice-winding loop for $N = 10, 13, 17, \cdots$ and to a twice-winding loop for $N = 18$ as in Fig. 3.5. The effect of the looping structures in the lattices on the ergodicity is unclear. In this way, models with square lattices are not preferred to study the ergodicity in the ED calculation.

The Rydberg atoms distribute randomly in a two-dimensional enclosing circle, i.e., the system has no lattice structure. The interaction between atoms is the van der Waals interaction and is a type of all-to-all interaction. Thus, the system is free from the aforementioned difficulty in the lattice geometry. One can select the system size to $N = 10 - 20$ by a unit of one spin in the ED calculation. This is advantageous in testing the system size effect on the ergodicity.

3.3 Hamiltonian and methods

Here, I define the Hamiltonian of the Rydberg atoms and describe how I prepare the random configuration of the Rydberg atoms by a numerical calculation.

The Hamiltonian of the effective spin model realized in the Rydberg atoms is defined as

$$\hat{H} = \frac{1}{2} \sum_{i=1}^{N} \sum_{\substack{j=1 \\ (j \neq i)}}^{N} J_{ij} \Big(\hat{S}_i^x \hat{S}_j^x + \hat{S}_i^y \hat{S}_j^y + \Delta \hat{S}_i^z \hat{S}_j^z \Big), \tag{3.9}$$

where the van der Waals interaction $J_{ij} = J/r_{ij}^{\alpha}$ with Euclidean distance between ith and jth atoms $r_{ij} = |\boldsymbol{x}_i - \boldsymbol{x}_j|$. Since the atoms are randomly distributed under the Rydberg blockade, the interactions J_{ij} are also random. J is set to 1 through this study. The anisotropy Δ and the exponent of the interaction α are set to -0.73 and 6 for consistency with the experiments.

3.3.1 Symmetry

In this study, I use indicators to statistically distinguish the ergodic phase from the nonergodic (MBL) phase. Since the ergodicity is a property involving all eigenstates, the indicators must be averaged over all the eigenstates. Symmetries of the Hamiltonian bring the crossing in the energy levels. Since the level crossing disturbs the statistics of the indicators, it must be removed. The Hamiltonian (3.9) has two symmetries that must be removed.

The Hamiltonian conserves the total z-spin defined by $\hat{Z} = \sum_{i=1}^{N} \hat{S}_i^z$. The matrix representation of the Hamiltonian is block-diagonalized into sectors labeled by the eigenvalues of $\hat{Z}$. Additionally, the Hamiltonian is invariant to operation of the parity $\hat{P} = \prod_{i=1}^{N} 2\hat{S}_i^x$. Clearly, $\hat{P}^2 = 1$. For the almost all sectors labeled by eigenvalues of $\hat{Z}$, the parity symmetry conflicts with the conserved quantity (equivalently, $[\hat{Z}, \hat{P}] \neq 0$). However, for the sector labeled by $\hat{Z} = 0$, the parity symmetry divides

the sector into two sectors. This is understood as follows. Consider arbitrary state spanned within the basis labeled by $\hat{Z} = z$. The states operated by $\hat{P}$ have eigenvalues with the opposite sign against the original sign:

$$\hat{Z}(\hat{P}\,|z\rangle) = \hat{P}\hat{P}\hat{Z}\hat{P}\,|z\rangle = -\hat{P}\hat{Z}\,|z\rangle = -z(\hat{P}\,|z\rangle). \tag{3.10}$$

From this equation, one can find that $|z\rangle$ and $\hat{P}\,|z\rangle$ have a same eigenvalue of $\hat{Z}$ only if the eigenvalue of $\hat{Z}$ is zero. The condition $\hat{Z} = 0$ can be satisfied only for systems containing even numbers of the spins.

In this study, I calculate systems with both even and odd numbers of the atoms. Thus, I focus on the sector with positive and minimum eigenvalue of $\hat{Z}$, that is, $\hat{Z} = 1$ for even N and $\hat{Z} = 1/2$ for odd N. Thus, the parity symmetry is irrelevant for my calculations. For clarity, I denote the sector labeled by $\hat{Z} = 1$ or $\hat{Z} = 1/2$ as $\mathcal{H}_{Z=1,1/2}$.

3.3.2 Random configurations of the Rydberg atoms (spins)

Here, I show the method to obtain the random configurations of the Rydberg atoms. The Rydberg atoms are randomly positioned within an enclosing circle whose diameter is L, and the Rydberg blockade affects to the positions of the Rydberg atoms. The range that the Rydberg atoms exclude the others is parameterized by the blockade radius r_{b}. The configuration of the atoms for the sufficiently small r_{b} is close to the uniform distribution, while it approaches to the close-packing configuration as r_{b} increases. I focus on the two-dimensional space and attempt to computationally generate the random configuration.

Naive method by iterative positioning One may come up with a naive method by iterative positioning to obtain the configurations. The algorithm of this method is as follows:

(1) determining the coordinate of single atom, (x, y), by random numbers,

(2) judging whether the position (x, y) satisfies the condition of the Rydberg blockade,

(3) going to (4) if the condition is satisfied, otherwise, returning to (1),

(4) repeating (1), (2) and (3) for another atoms until the all atoms are put.

This method works well for the small r_{b} whereas it does not for the large r_{b} because the accept rate decays significantly for the large r_{b}.

Method using displacement with expanding radii of atoms I take a different strategy to obtain the random configurations efficiently. Since the main difficulty in the naive method is the low acceptance rate, I adopt a method that all atoms are initially put within the enclosing circle and are displaced interatively. Through this method, I treat all atoms as rigid circles with a radius $r_{\mathrm{b}}/2$. This treatment is valid in the sense that the closest distance between the centers of the mass of the atoms is set to r_{b}. The detail method is as follows:

(1) aligning all the atoms in the configuration of the hexagonal crystals,

(2) iteratively picking up an atom and randomly choosing direction to displace it,

(3) calculating the maximal distance that is acceptable to displace the atom without violation of the condition of the Rydberg blockade, $l_{\max}$,

(4) randomly choosing the distance to displace the atom, $l_{\rm rnd}$, (which is less than the maximum distance,) and displace the atom by the distance$l_{\rm rnd}$.

(5) repeating (1)-(4) until the configurations stochastically settle.

This method is much faster than the naive method for the large $r_{\rm b}$ because it has no reject rate.

The configurations generated for the large $r_{\rm b}$ still resemble to the initial configuration because the hexagonal configuration is so stable that prohibits the configurations to transit to another configurations by the iterative displacement. To overcome it, I adopt the dynamical expansion of $r_{\rm b}$ through the iterative displacement. The improved method is as follows. Let's denote the initial radii of the rigid circles as r_0 and the radii at the nth loop of the iterative displacement as r_n, respectively. Until $n = 100$, the radii are fixed, $r_n = r_0$. After the 100 times of the iterations, the radii are updated as $r_n = \left[(r_{\rm b}/2r_0)^{1/M}\right] r_{n-1}$ if the condition that any atom is remote from the others by distance longer than $r_{\rm b}$ still satisfies after the update of the radii. The update continues until the radius of the all atoms reach to $r_{\rm b}/2$. The random configuration obtained by this method is depicted in Fig. 3.6. The detail description of this method is provided in Appendix C.

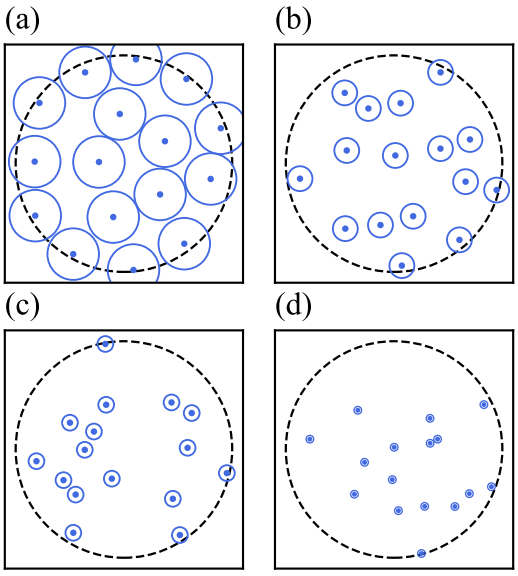

Fig. 3.6 Random configuration of atoms. The points and the circles denote the positions of atoms and the rigid sphere whose radii correspond to half of the blockade radius, $r_{\rm b}/2$. These results are obtained for (a) $W = 0.25$, (b) $W = 1.075$, (c) $W = 2.675$, (d) $W = 11.501$.

3.4 Definition of the strength of disorder

In a majority of systems employed for studying MBL, disorder is introduced in Hamiltonian's parameters as random numbers. These random numbers typically obey the uniform distributions or the Gauss distributions, where these distributions are well characterized by means and variances. There is no doubt that the variances directly relate to the strength of disorder. Thus, the variances (or its square root) can be regarded as the parameters of disorder. For example, when one adopt a uniform distribution, the strength of disorder can be defined as the width of the uniform distribution, which is proportional to the square root of the variance.

In contrast, in this study, how to determine the definition of strength is not so trivial. The procedure to obtain the random parameters in this study is summarized as follows. First, one sets the parameters of randomness in random configurations: the diameter of the enclosing circle L, the blockade radius $r_{\mathrm{b}}/2$ and the number of the atoms N. Second, one generates random configurations of the atoms. Finally, one calculates the interactions between the spins from the configuration. Then, one obtains the distribution of the interactions and finds the corresponding mean and variance. In other words, only after obtaining the interactions, one can find the statistical values. This is quite inconvenient in estimating the critical strength of disorder.

To overcome the inconvenience, I try to define the disorder strength W from the initial three parameters L, r_{b} and N. In the aforementioned method to generate random configurations, the Rydberg atoms are regarded as rigid circles with the radii $r_{\mathrm{b}}/2$, and the configurations are generated from the iterative displacement of the rigid circles. In the situation where the rigid circles position randomly, whether the rigid circles are packed equidistantly or randomly is determined by the packing ratio of the rigid circles, which is give by the ratio of the total area of the rigid circles to the area of the enclosing circle, i.e.,

$$\rho = \frac{N\pi(r_{\mathrm{b}}/2)^2}{\pi(L/2)^2}. \tag{3.11}$$

For the small ρ, although the positions of the rigid circles are weakly correlated, the positions of the rigid circles follows a nearly uniform distribution. For the large ρ, the rigid circles are packed in the close packing way. The packing ratio in the close packing configuration approaches $\eta = \pi/\sqrt{12}$ in $N \to \infty$. However, since the close packing configuration strongly depends on N, the packing ratio is slightly apart from η for the small number of the atoms. The strength of the disorder W is imposed to be a monotonically increasing function as the disorder strength. I define W as the inverse of the packing ratio

$$W = \frac{\eta}{4}\frac{L^2}{Nr_{\mathrm{b}}^2}. \tag{3.12}$$

There is an ambiguity in ways to take thermodynamic limit. Consider taking thermodynamic limit with the fixed disorder strength, $W = \mathrm{const.}$. It is obvious that increasing N up to infinity is necessary for taking thermodynamic limit. When N increases and W is fixed, one has two options:

increasing the diameter of the enclosing circle L or decreasing the blockade radius $r_{\rm b}$. Although one may think that the two options are same, these options differ in the energy scale. The energy scale of the Hamiltonian is determined by the maximal value of the interaction $J_{ij} = J/r_{ij}^6$, where r_{ij} is a distance between the atoms. If one adopt the way of decreasing $r_{\rm b}$ and keeping L fixed when taking the thermodynamic limit, the maximal interaction $J/r_{\rm b}^6$ diverges, and the energy scale of the Hamiltonian also diverges. In contrast, if one adopt the other way of increasing L and keeping $r_{\rm b}$ fixed, the maximal interaction is fixed, and the energy scale does not diverge. Instead of the energy scale, the volume of the system diverges to infinity, which is natural in the experimental setting. Thus, in this study, I increase the diameter of the enclosing circle L and keep the blockade radius $r_{\rm b}$ constant when testing a size effect at a given W.

3.4.1 Close packing configuration

Knowledge of close packing of circles in a circle would facilitate us to resolve the problem to generate the random configurations of the rigid circles in the enclosing circle. Here, I show some examples of the close packing configurations in Fig. 3.7 and the radii of the packed circles in Fig. 3.8. All of the data is quoted from Ref. [109]. As in Fig. 3.7, the close packing configurations are strongly affected by the number of the packed circles N. However, the radii of the packed circles asymptotically follow a clear-cut dependence on N.

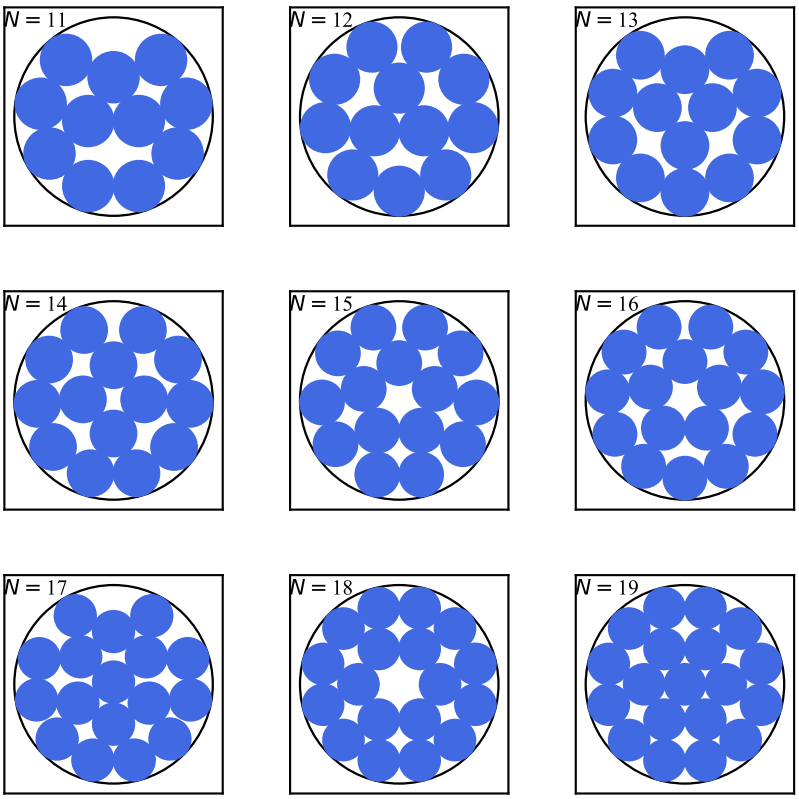

Fig. 3.7 Close packing configuration from $N = 11$ to $N = 19$. The radius of the enclosing circle is R, and the radii of the packed circles $r_{\rm max}$ are shown in Fig. 3.8(a).

Some of the close packing configurations have symmetries to rotation or reflection. The spin systems on these symmetric configurations would possess conserved quantities coming from the ge-

ometries, and some of the corresponding energy levels would be degenerated. Nevertheless, in this study, the spin systems on the close packing configuration are out of scope. These symmetries are broken in the random configuration unless a configuration is exactly same as the close packing one. Thus, I have no necessity to care about the geometrical symmetries.

I shown the N dependence of the radius of the packed circles $r_{\max}$ and the corresponding area density $\rho_{\max} = Nr_{\max}^2/R^2$ in the close packing configurations in Fig. 3.8. The radii $r_{\max}$ are given by a ratio to the radius of the enclosing circle R in the figure. The radii $r_{\max}$ decay as N increases as in Fig. 3.8(a), and the form of the decay asymptotically approaches to the power of N, which is apparent in Fig. 3.8(b). The power corresponds to the slope in the log-log plot. I determine the slope by using the polynomial fitting. The slope is obtained as -0.487, which is close to -0.5. The area density of the packed circles is given by $\rho_{\max} = Nr_{\max}^2/R^2$. As in Fig. 3.8(c) approaches to the close packing ratio in two dimensions given by $\eta = \pi/\sqrt{12}$ (depicted in the orange line in the figure). As in Fig. 3.8(d), the difference between the area density and η decreases faster than a power of N. Although the area density $\rho_{\max}$ is apart from the close packing rate η in finite N, $\rho_{\max}$ dramatically approaches to η as N increases. Assumed that the area density equals to η, $Nr_{\max}^2$ is constant. In this way, the relation between $r_{\max}$ and N reads $r_{\max} \propto 1/\sqrt{N}$. I draw the linear line with the slope -0.5 in Fig. 3.8(b) (depicted in green). The line agrees well to the scattered data points.

3.4.2 Distribution of the interaction

Here, I show the distributions of the distance r_{ij} and the interaction J_{ij} and elucidate the N and W dependence of J_{ij}. These distributions are shown in Fig. 3.9 for $N = 12, 14, 16, 18, 20$ and several W. The distributions are drawn by histograms of r_{ij} and J_{ij} accumulated for 10^4 realizations. The horizontal axis of the histogram is equidistantly divided into 100 segments in the log-scale. Since $J_{ij} \propto r_{ij}^6$, the histogram of r_{ij} in the log-scale has exactly same information to that of J_{ij}. These two histograms overlap by multiplying the negative sign and rescaling the x-axis.

As aforementioned, for fixed W, the diameter of the enclosing circle L is scaled as $\sqrt{N}$, and $r_{\rm b}$ is set to unit regardless of N. For this reason, the smallest distance is set to 1 while the largest distance is scaled as $\sqrt{N}$. Around the close packing configuration ($W \sim 0.25$), the circles are packed closely in such a way as to almost touch to the nearest circle as in Fig. 3.6(a). Since, due to the high density, the circles almost cannot move, the distribution of the distance has multiple peaks as in Fig. 3.9(a). The number and the positions of the peaks strongly are affected by N. The cut off at the left edge in the distribution of the distance corresponds to the minimal distance $r_{\rm b}$, and the cut off at the opposite side corresponds to the maximal distance L. As W increases, the width of the peaks enlarges so that the fine structure of the peaks are unresolved in Fig. 3.9(b). For the large W, the circles distribute sparsely regardless to the positions of the other circles. As in Fig. 3.9(c) and (d), there is no peak, and the distributions become smooth curves. At $W = 11.5$, the cut off at the left side in the distribution of the distance is not prominent, and the positions of the circles distribute uniformly.

It is expected that the variance of these distributions becomes large as W increases for W being a good parameter of the disorder. I show the means and the standard deviations of the interactions in Fig. 3.10. I calculate two types of the mean: arithmetic and geometric means. The arithmetic mean is

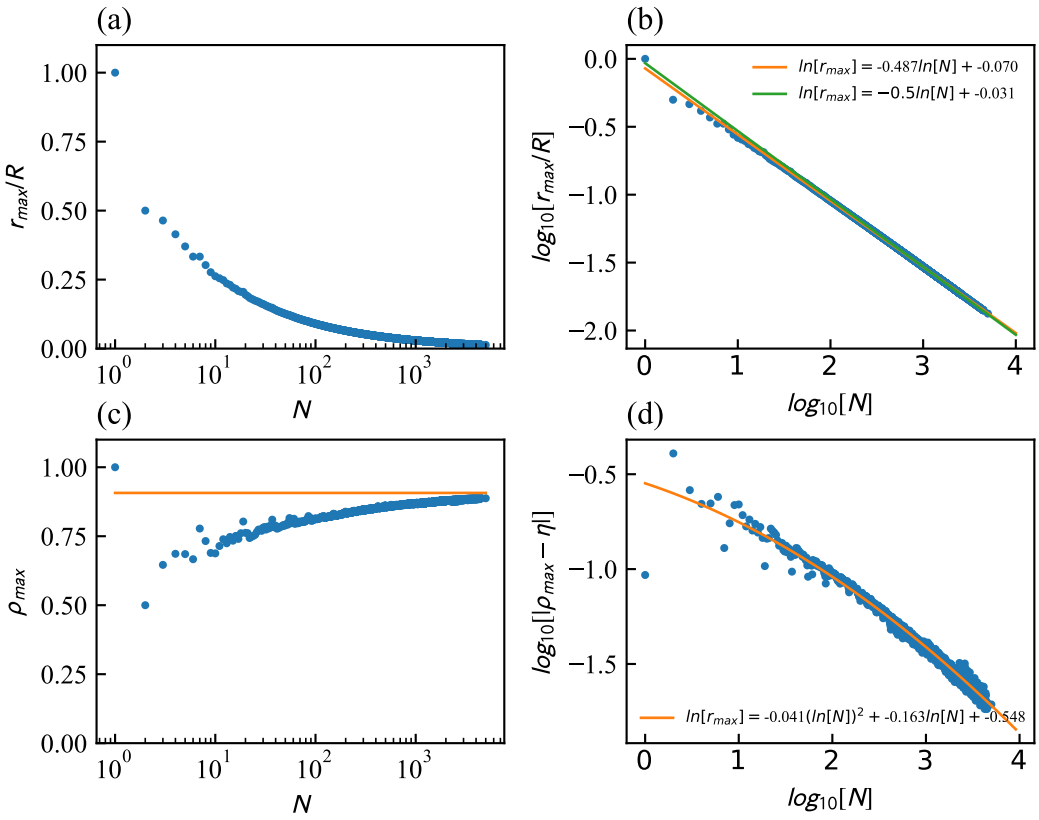

Fig. 3.8 Radius $r_{\max}$ and density $\rho_{\max} = Nr_{\max}^2/R^2$ of the circles close-packed in a circle with a radius R. (a) The dependence of $r_{\max}$ on the number of the packed circles N. (b) The log-log plot of the N dependence of $r_{\max}$. The radius $r_{\max}/R$ is proportional to $1/\sqrt{N}$. The orange line is drawn by the polynomial fitting, and the slope is ~ -0.5. Assumed that the area density approaches to the close packing value, the radius is necessary to be $\propto 1/\sqrt{N}$. The green line is a linear line with the slope -0.5, which agrees well with the scattered points. (c) The N dependence of the area density $\rho_{\max}$. The area density approaches to the close packing ratio $\eta = \pi/\sqrt{12}$ as N increases. (d) The log-log plot of the figure (c).

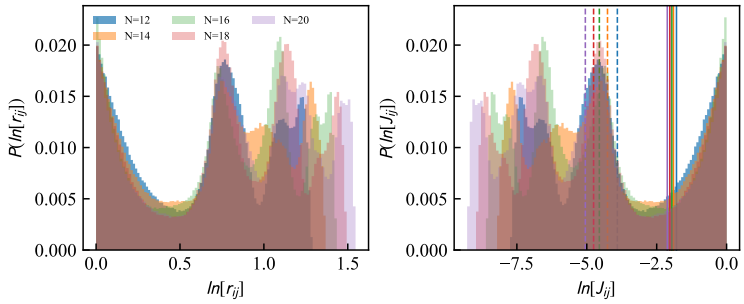

(a) $W = 0.25$

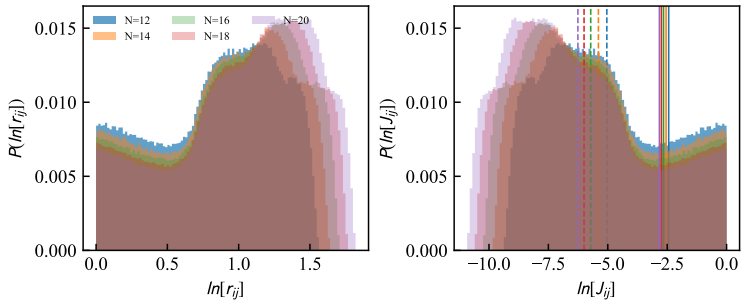

(b) $W = 0.43$

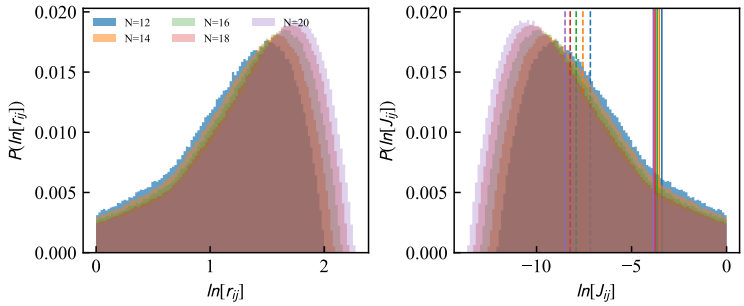

(c) $W = 1.07$

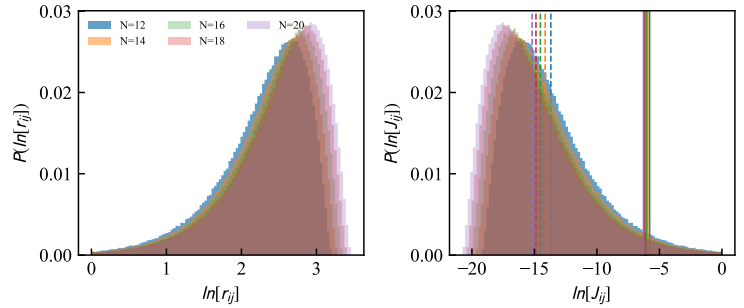

(d) $W = 11.5$

Fig. 3.9 Distributions of the distances between the centers of the mass of the Rydberg atoms and the strength of the interactions between the spins for $N = 12, 14, 16, 18, 20$. The distribution of the distance (the interactions) has a cut off at the left (right) edge corresponding to the fact that the nearest distance of the atoms is bounded by r_{b}. At the other edge, the both distributions extends to the outwards of the distribution as N increases because the diameter is scaled as $\propto \sqrt{N}$ to fix W and r_{b}. The solid lines and the solid lines denote the arithmetic means and the geometric means of the interactions. (a) Distributions for $W = 0.25$. The random configuration is close to the close packing configuration in the sense of area density as in Fig. 3.6(a). The both distributions have spikes reflecting the configuration close to the close packing. (b) Distributions for $W = 0.43$. The both distribution forms two mountains around the edges of the distribution. In the distribution of the distances (interactions), the left (right) one comes from the atoms almost contacting, i.e., $r_{ij} \sim r_{\mathrm{b}}$, and the right (left) one comes from the atoms remote from the other in the scale of the radius of the enclosing circle, i.e., $r_{ij} \sim L$. (c) Distributions for $W = 1.07$. The both distributions have a single mountain. (d) Distributions for $W = 11.5$. The cut off at the left (right) edge almost disappears, which corresponds to the uniform distribution of the atoms in the enclosing circle.

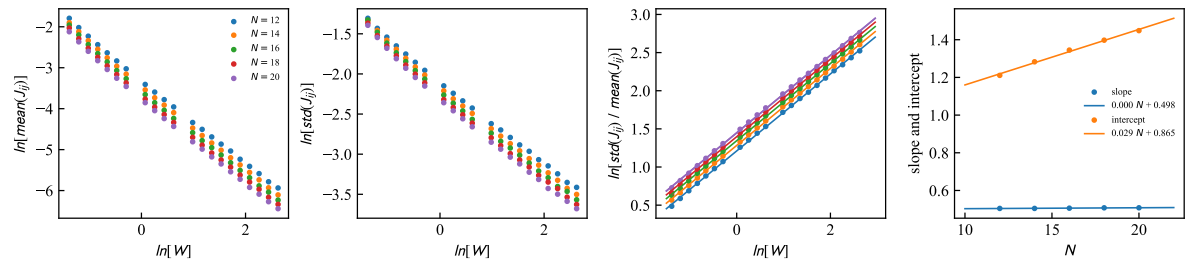

(a) Arithmetic mean and standard deviation

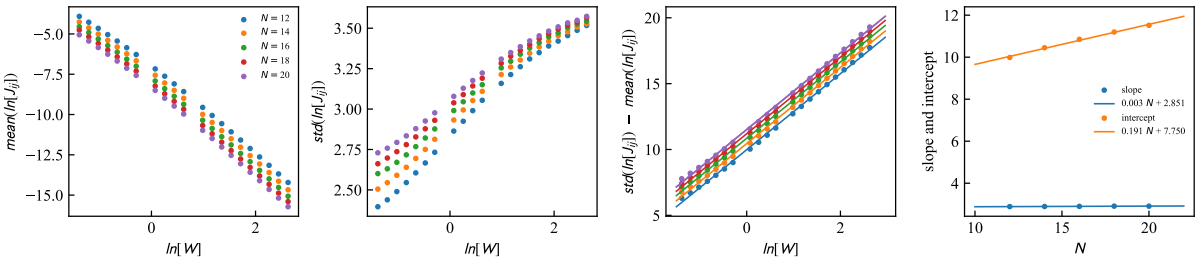

(b) Geometric mean and standard deviation of $\ln[J_{ij}]$

Fig. 3.10 (a) The arithmetic mean and the standard deviation of J_{ij}. The mean and standard deviation decay exponentially with N. The ratio of the standard deviation to the mean $\mathrm{std}(J_{ij})/\mathrm{mean}(J_{ij})$ exponentially increases with N. Since the third figure counted from the left side is shown in the log-log plot, the slope in the figure corresponds to the power of $\mathrm{std}(J_{ij})/\mathrm{mean}(J_{ij})$ with respect to W. The slope has no dependence on N while the intercept has the linear dependence on N as in the last figure. (b) The geometric mean and the standard deviation of $\ln[J_{ij}]$. The difference $\mathrm{std}(\ln[J_{ij}])-\mathrm{mean}(\ln[J_{ij}])$ is almost linear as in the third figure, and the slope and the intercept are as shown in the last figure.

a usual mean given by $\mathrm{mean}(J_{ij}) = \sum_{n_s}\sum_{ij} J_{ij}^{(n_s)}/N_s N_{tot}$, where n_s and $N_s = 10^4$ denote the serial number of the random configurations and the total number of the random configuration. The suffix ij runs all of the pairs without counting the duplicate pairs and the corresponding total number N_{tot} is given by $N(N-1)/2$. The standard deviation is given by $\mathrm{std}(J_{ij}) = \sqrt{\mathrm{mean}(J_{ij}^2) - \mathrm{mean}(J_{ij})^2}$. The W dependences of $\mathrm{mean}(J_{ij})$ and $\mathrm{std}(J_{ij})$ are shown in Fig. 3.10(a), and the both decay as W increases. However, the ratio $\mathrm{std}(J_{ij})/\mathrm{mean}(J_{ij})$ is a increasing function of W. Clearly, the rate obeys the power law of W, which corresponds to the linear line in the log-log plot. The slope in the log-log plot corresponds to the power of $\mathrm{std}(J_{ij})/\mathrm{mean}(J_{ij})$ with respect to W while the intercept corresponds to the multiplier that is irrelevant to W, i.e., $\mathrm{std}(J_{ij})/\mathrm{mean}(J_{ij}) = aN^b$, where a is the multiplier (the intercept) and b is the power (the slope). Specifically, $\mathrm{std}(J_{ij})/\mathrm{mean}(J_{ij}) \simeq a(N)\sqrt{N}$ from the last panel in Fig. 3.10(a). Since the interaction distributes in a wide scale, the log plot would help one to understand the profile of the distribution. The mean in the logarithmic space is called a geometric mean, which is defined as $\exp[\mathrm{mean}(\ln[J_{ij}])]$. The standard deviation in the logarithmic space is also defined as $\exp[\mathrm{std}(\ln[J_{ij}])]$. The ratio $\exp[\mathrm{std}(\ln[J_{ij}])]/\exp[\mathrm{mean}(\ln[J_{ij}])]$ is an increasing function of W as well as the arithmetic one. In this sense, the definition of W works to measure the extent of the variance in the distribution of the interactions.

3.4.3 Density of states

Here, I show the density of states (DOS) for given N and W. DOS is defined as a histogram of the energy levels, whose horizontal axis is separated equidistantly by 50 segments. In the ergodic regime,

DOS is expected to have no gap and be smooth. In the non-ergodic regime, DOS is expected to have gaps, and the positions of gaps depend on the realizations. Some examples of DOS are depicted in Fig. 3.11. At $W = 0.25$, DOS is smooth and has no gap, which implies that the system is ergodic in this regime. On the other hand, at $W = 1.548$, DOS has many gaps, which implies that the system is non-ergodic in this regime. At $W = 0.622$, the disorder strength is within the intermediate regime. One find that the system is ergodic for the small W and is non-ergodic for the large W from viewpoint of the shape of DOS. In this sense, the definition of W in Eq. 3.12 works well to characterize the disorder strength.

3.5 Indicators to detect ergodicity

Here, I introduce some indicators to distinguish the ergodic and non-ergodic phases, and illustrate the method to extract the critical strength of the disorder from the trends of the indicators.

3.5.1 Method to estimate the critical strength of the disorder

I illustrate the scheme to identify the critical disorder strength W^*. After calculation, I have a numerical result of an indicator to distinguish the system ergodic or MBL. In a wide range of W, the indicator denotes a plateau in the smaller W and another plateau in the larger W as in Fig.3.12(a). I call the former regime as the ergodic regime and the latter regime as nonergodic regime. Between these two regimes (in the intermediate regime), the indicator smoothly connects the values in ergodic and nonergodic regimes. The smooth variation of the indicator is not dramatic, and the width of the intermediate regime is finite. For this reason, the critical strength of disorder W^* can not be determined straightforwardly. In this study, I adopt a method to identify the critical strength of disorder W^* as W such that the derivative takes the maximal value (Fig. 3.12(b)). I compute the indicators for $N = 11 - 16$ and average them over the $10^4 - 3 \times 10^4$ random configurations.

3.5.2 Definition of averaging

Since all the indicators are defined for individual eigenstates, I average the indicators over eigenstates within a subset of the eigenstates. The subset consists of eigenstates of $\hat{H}_{Z=1,1/2}$ within 200 eigenstates counting up or down from the mean energy E_{mean}. The mean energy is defined as the mean value over all the eigenenergies of $\hat{H}$ within the sector $\mathcal{H}_{Z=1,1/2}$. Furthermore, since the Hamiltonian is random, I average the indicators over all the random configurations. The averaging is summarized as

$$\overline{I} = \langle \langle I(\alpha, n_s) \rangle_\alpha \rangle_{n_s}, \tag{3.13}$$

where I is an indicator, α and n_s denote the ordinal numbers for eigenstates and realizations respectively, and $\langle \cdot \rangle_\cdot$ denotes averaging.

Additionally, one of the indicators, the bipartite entanglement entropy S_{half} (see below), depends on ways to cut the system into two subsystems. I calculate the bipartite entanglement entropy for

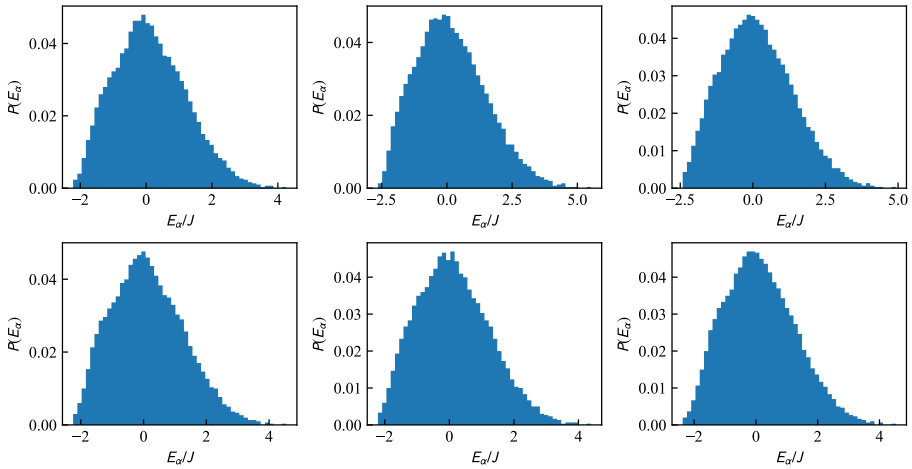

(a) Density of states at $W = 0.250$.

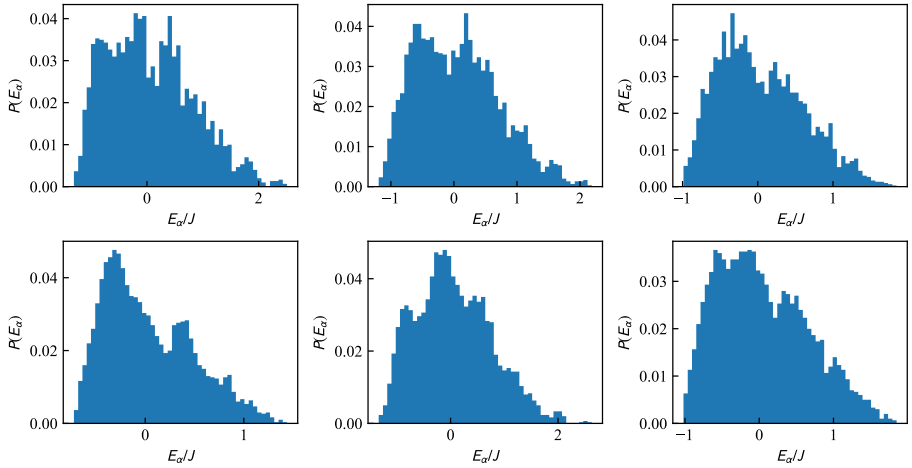

(b) Density of states at $W = 0.622$.

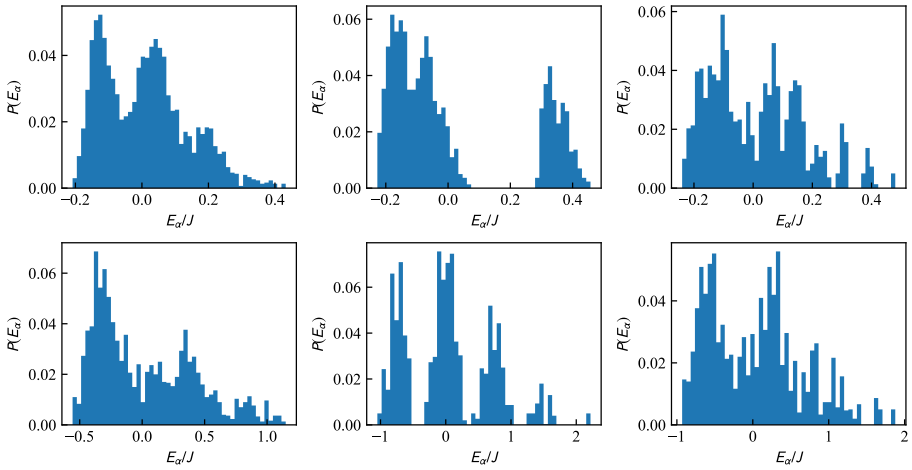

(c) Density of states at $W = 1.548$.

Fig. 3.11 Examples of density of states (DOS) for individual random configuration. The histogram is normalized so that the sum equals to 1. The bins are equidistantly separated into 50 segments. The number of spins is fixed to 14 for all the figures. The DOS is smooth and has no gap At $W = 0.250$ while the DOS has many gaps at $W = 1.548$.

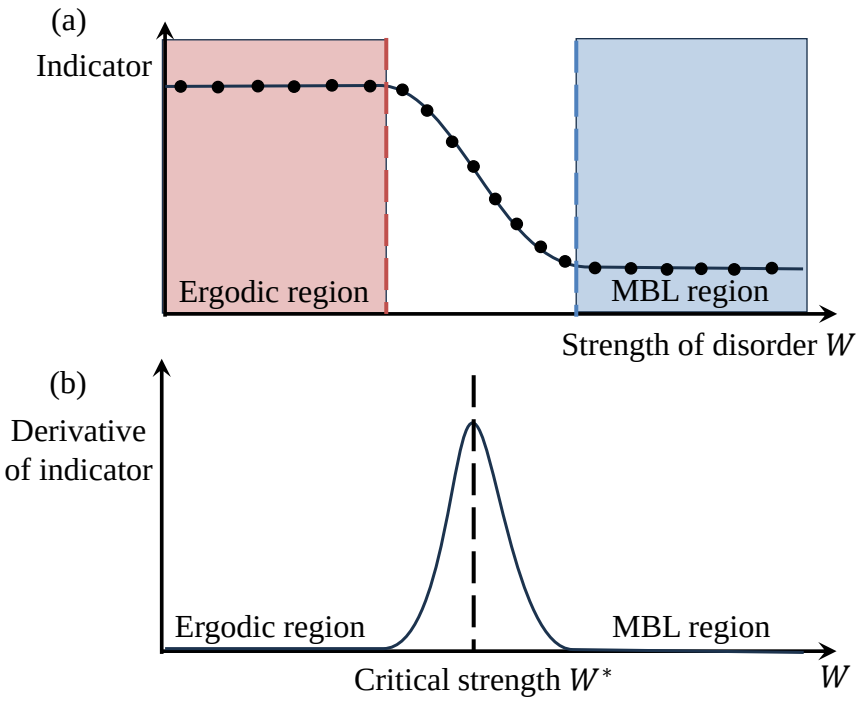

Fig. 3.12 Scheme to estimate the critical strength of disorder W^*. (a) Profile of an ergodic indicator. The scattered dots denote bare results obtained in the computation. The smooth curve is obtained by interpolation. The indicator mainly takes a value in the small W side and a different value in the large W side. I regard the former as the ergodic region and the latter as the MBL region. In the intermediate region, these two values are connected smoothly. (b) Profile of the indicator differentiated with respect to W^*. The derivative takes the largest value in the intermediate regime. I identify the critical strength of disorder W^* as W such that the derivative takes the largest value.

~ 100 ways to cut, and take average it over the ways of bipartition. The averaged $S_{\rm half}$ is defined as

$$\overline{S_{\rm half}} = \langle\langle\langle S_{\rm half}(\alpha, n_s, c)\rangle_\alpha\rangle_{n_s}\rangle_c, \tag{3.14}$$

where c denotes the ordinal number for the ways to cut the system into two subsystems.

3.5.3 Indicators to detect ergodicity

Here, I describe the definition of the indicators to detect the ergodicity, and show the corresponding numerical results.

3.5.3.1 Inverse participation ratio

Here, I introduce the inverse participation ratio (IPR) as

$$\mathrm{IPR}(\alpha, n_s) = \sum_s |\left\langle s|\alpha\right\rangle_{n_s}|^4, \tag{3.15}$$

where $|\alpha\rangle_{n_s}$ is the αth eigenstate for the Hamiltonian at the n_sth realization, and the computational basis $|s\rangle = \{|\uparrow\rangle, |\downarrow\rangle\}^{\otimes N}$. Here, $\hat{S}^z|\uparrow\rangle = +(1/2)|\uparrow\rangle$ and $\hat{S}^z|\downarrow\rangle = -(1/2)|\downarrow\rangle$. In the most localized case where the many-body eigenfunction is localized at a single eiegnbasis (for example $|\uparrow\cdots\uparrow\rangle$), the IPR is 1. On the other hand, if the system satisfies ETH (more specifically the Gaussian orthogonal ensemble, GOE), the eigenfunction extends over the computational space, and IPR is much smaller than 1. In the (GOE) case, an eigenfunction can be regarded as a random and real unit vector in the $\mathcal{D}$-dimensional space, and then the averaged IPR reads

$$\overline{\mathrm{IPR}}(\alpha) = \sum_s \overline{|\left\langle s|\alpha\right\rangle|^4} = \sum_s \frac{3}{\mathcal{D}^2} = \frac{3}{\mathcal{D}}, \tag{3.16}$$

where $\bar{\cdot}$ denotes the average over the random vectors. In the middle of Eq. (3.16), I use $\overline{\langle s|\alpha\rangle\langle\beta|t\rangle} = \delta_{st}\delta_{\alpha\beta}/\mathcal{D}$ and $\overline{(\langle s|\alpha\rangle\langle\beta|t\rangle)^2} = 3\overline{\langle s|\alpha\rangle\langle\beta|t\rangle}^2$, where s, t denotes the computational basis, and α, β denote the serial numbers of the eigenfunctions.

IPR has been used to analyze the behavior of Anderson localization around the critical point [110]. Since Anderson localization has a clear interpretation as localization of wavefunctions, it is natural that IPR can capture the critical point of Anderson localization. On the other hand, since MBL is a many-body problem, MBL has no clear interpretation like Anderson localization. However, IPR has been used to characterize the ergodicity in several references [33, 35–41]. To use IPR in MBL problems, one needs to map MBL problems to Anderson localization problems in the Fock space [31–33]. In general, many-body Hamiltonian can be mapped to single-particle problems in Fock space. In this picture, a many-body state is mapped to a single site. The spin flip-flop terms and Ising terms can be mapped to the hopping between sites and potentials in Fock space, respectively. In this sense, the MBL problem is regarded as Anderson localization in Fock space.

Instead of IPR, I calculate the partition entropy given by

$$S_{\mathrm{P}}(\alpha, n_s) = -\ln[\mathrm{IPR}(\alpha, n_s)]. \tag{3.17}$$

The partition entropy is zero in the case that the eigenfunction is fully localized in the computational basis while it is $\ln[\mathcal{D}/3]$ in the case of ETH. After taking logarithm, I average S_{P} over the eigenstates and the random configurations.

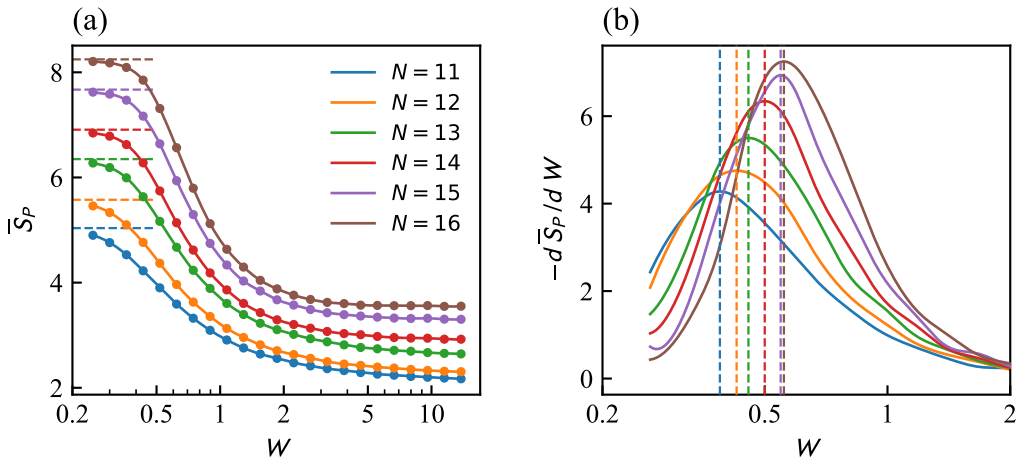

Fig. 3.13 Disorder strength dependence of the partition entropy and its derivative. (a) Dependence of the partition entropy S_{P} on the disorder strength W. In the small W side, S_{P} reaches the maximal value $\ln[\mathcal{D}/3]$ (denoted by the dashed lines). The system in the ergodic (ETH) regime for $W \lesssim 0.4$. As W increases, S_{P} decays and relaxes to smaller values. It is regarded that MBL regime is in $W \gtrsim 2$ for $N = 11 - 16$. (b) Derivative of the partition entropy S_{P} with respect to disorder strength W. The derivative reaches to the maximal value around $W \sim 0.5$, and the disorder strength such that the derivative reaches the maximal is regarded as the critical disorder strength W^* (denoted by the dashed lines). W^* shifts to the larger side as N increases.

I show the numerical result of the partition entropy in Fig. 3.13. The partition entropy S_{P} reaches the ETH value $\ln[\mathcal{D}/3]$ for $W \lesssim 0.4$ for $N = 11 - 16$ as in Fig 3.13(a). The dashed lines in the figure denote the ETH value. The regime $W \lesssim 0.4$ is regarded ergodic within my calculation. S_{P} decays and relaxes to a smaller value as W increases. The regime $W \gtrsim 2$ is regarded as the MBL regime. To determine the critical disorder strength W^*, I differentiate S_{P} with respect to W as in Fig 3.13(b). The derivative has a peak around $W \sim 0.5$, and the maximal W such that the derivative reaches the maximum value is regarded as W^* (denoted as the dashed lines in the figure). On find that the critical disorder strength shift to the larger W side as the number of the spins N increases.

3.5.3.2 Entanglement entropy

Here, I introduce the entanglement entropy (EE) as

$$S_{\mathrm{E}} = -\mathrm{Tr}_A[\hat{\rho}_A \ln \hat{\rho}_A], \tag{3.18}$$

where the trace Tr_A is taken for the degrees of freedom within a subsystem A, and the reduced density matrix $\hat{\rho}_A = \mathrm{Tr}_B[\hat{\rho}]$ with $\hat{\rho} = |\psi\rangle\langle\psi|$. If $S_{\mathrm{E}} = 0$, the subsystem A is not entangled with the remained

subsystem B. The maximum value of the EE is $\ln\mathcal{D}$, and then A and B are fully entangled.

EE is an indicator to detect ergodicity in quntum many-body systems [34–36]. In the beginning of the MBL studies, the main issue was how to distinguish MBL because unlike Anderson localization, MBL has no clear picture in real space and is impossible to define from an intuitive physical insight. For this reason, EE has been used to distinguish MBL systems from ergodic systems. In the ergodic systems, local spins hybridizes to the other spins near them, and the entanglement spread over the whole systems. Thus, EE is large in the ergodic systems. On the other hand, in MBL systems, the hybridization does not spreads over the systems, and EE is suppressed.

Ways to divide the system into two subsystems are important to analyze the entanglement structures. In the following parts, I introduce several types of partition and show the results.

Entanglement entropy of the most uncoupled atom The most simple way to divide a system into two subsystems is picking up an atom and defining it as a subsystem. There are many option to pick up an atom. Here, I pick up the most uncoupled atom. EE of the most uncoupled atom is expected smallest among EEs of a single spin.

I pick up the most uncoupled atom by the following method. The interactions in the Hamiltonian (3.9) are random because of the random configurations of the atoms. Some atoms form clusters of the atoms while the others are scattered. Since the interactions decay with the distance between the atoms, all the interactions within the clusters are comparable. On the other hand, the remote atoms weakly interact with the other atoms. In this sense, I conjecture that an atom that is most remote from all the other atoms corresponds to the most uncoupled atom. There is no reasonable way to define the most remote atom by measuring the distance. I adopt an energetic way to find the most uncoupled atom. Let's start with defining the energetic measure as

$$\hat{H}_i = \frac{1}{2}\sum_{\substack{j=1\\(j\neq i)}}^{N} J_{ij}\Big(\hat{S}_i^x\hat{S}_j^x + \hat{S}_i^y\hat{S}_j^y + \Delta\hat{S}_i^z\hat{S}_j^z\Big). \tag{3.19}$$

Of course, the sum of $\hat{H}_i$ over i equals to the original Hamiltonian (3.9). Furthermore, I average the absolute value of $\hat{H}_i$ over the eigenstates as $\overline{E}_i = |\mathrm{Tr}[\hat{H}_i]|/\mathcal{D}$, where the trace is taken within a sector labeled by $\hat{Z} = 1$ or $\hat{Z} = 1/2$. I refer $\overline{E}_i$ as the mean partial energy. I expect that $\overline{E}_i$ is low for remote atoms from the others.

The mean partial energy can be analytically evaluated. Let's take the trace in the computational basis $|s\rangle = \{|\uparrow\rangle, |\downarrow\rangle\}^{\otimes N}$. In the basis, $\mathrm{Tr}[\hat{S}_i^\alpha\hat{S}_j^\alpha] = 0$ for $\alpha = x, y$ while

$$\mathrm{Tr}[\hat{S}_i^z\hat{S}_j^z] = \sum_s \langle s|\,\hat{S}_i^z\hat{S}_j^z\,|s\rangle = \sum_s\Big(n_i^s - \frac{1}{2}\Big)\Big(n_j^s - \frac{1}{2}\Big), \tag{3.20}$$

where n_i^s is 1 if the ith spin is in $|\uparrow\rangle$ and 0 if it is in $|\downarrow\rangle$, and the summation is taken within the sector $\mathcal{H}_{\hat{Z}=1,1/2}$. In the sector, the number of up spins is $N_\uparrow = \lfloor N/2\rfloor + 1$, and that of down spins is

$N_\downarrow = N - N_\uparrow$. The contribution from the interactions between the parallel spins is evaluated as

$$\frac{1}{4}\Big(\frac{(N-2)!}{(N_\uparrow-2)!N_\downarrow!}+\frac{(N-2)!}{N_\uparrow!(N_\downarrow-2)!}\Big), \tag{3.21}$$

and that from interactions between the anti-parallel spins is evaluated as

$$-\frac{1}{2}\frac{(N-2)!}{(N_\uparrow-1)!(N_\downarrow-2)!}. \tag{3.22}$$

By summing them, the trace for $i \neq j$ reads

$$\begin{aligned}\mathrm{Tr}[\hat{S}_i^z\hat{S}_j^z] &= \frac{1}{4}\Big(\frac{(N-2)!}{(N_\uparrow-2)!N_\downarrow!}+\frac{(N-2)!}{N_\uparrow!(N_\downarrow-2)!}\Big)-\frac{1}{2}\frac{(N-2)!}{(N_\uparrow-1)!(N_\downarrow-2)!}\\ &= \frac{1}{4}\frac{(N-2)!}{(N_\uparrow-2)!(N_\downarrow-2)!}\Big((N_\uparrow-N_\downarrow)^2-N\Big)\\ &= \frac{1}{4}\frac{(N-2)!}{(N_\uparrow-2)!(N_\downarrow-2)!}\Big((2\lfloor N/2\rfloor+2-N)^2-N\Big).\end{aligned} \tag{3.23}$$

Thus, the mean partial energy is evaluated as

$$\overline{E}_i = \Big|\frac{\Delta}{8\mathcal{D}}\frac{(N-2)!}{(N_\uparrow-2)!(N_\downarrow-2)!}\Big((2\lfloor N/2\rfloor+2-N)^2-N\Big)\Big|\sum_{\substack{j=1\\(j\neq i)}}^{N}J_{ij}. \tag{3.24}$$

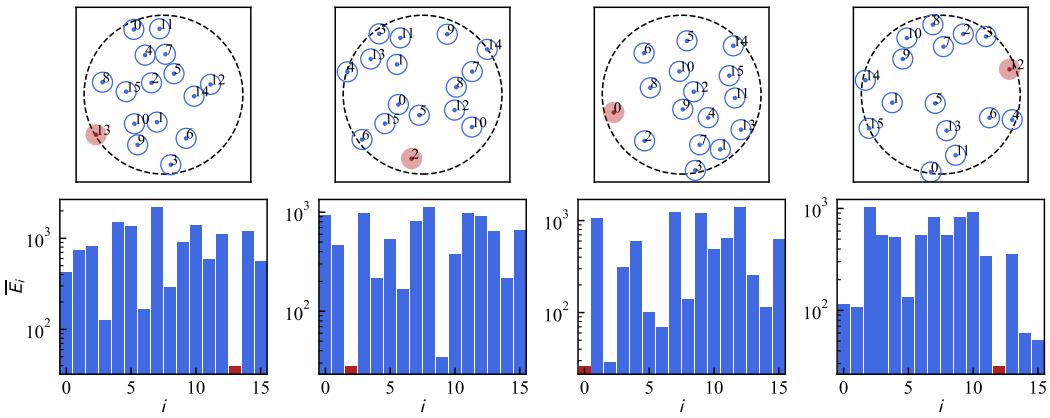

Fig. 3.14 Relation between the remotest atom and its mean partial energy. The upper panel shows random configurations for $N = 16$ and $W = 0.869$, and the lower panel shows the corresponding mean partial energy. Serial numbers labeled to the individual atoms in the upper panel correspond to the x-axis in the lower panel. The smallest mean partial energy (colored in red) coincides to the remotest atom (filled in red) in the configuration.

If $\overline{E}_i$ is smallest than those for the other atoms, the ith atom is expected to be remotest from the cluster of the other atoms. However, it is nontrivial that the most uncoupled atom corresponds to the remotest atom from the clusters. Here, I check the relations between the most uncoupled atom and the remotest atom. I show the several configurations of atoms and the corresponding $\overline{E}_i$ in Fig. 3.14. The upper panel shows random configuration for $N = 16$ and $W = 0.869$, and the lower panel shows

the corresponding mean partial energy. The numbers attached to the rigid circles in the upper panel correspond to the numbers in the x-axis in the lower panel. One find that the remotest atom has the smallest $\overline{E}_i$. Thus, the most remote atom is regarded most uncoupled as far as using the mean partial energy $\overline{E}_i$.

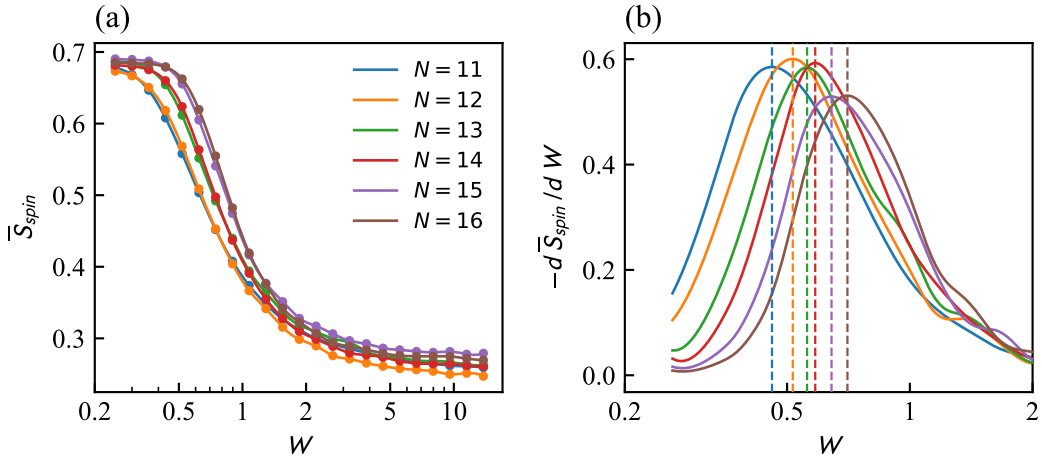

Fig. 3.15 Disorder strength of the entanglement entropy between the most uncoupled spin and the others. (a) The dependence of the entanglement entropy between the most uncoupled spin and the others $\overline{S}_{\rm spin}$ on the strong disorder W. $\overline{S}_{\rm spin}$ is the maximum value $\ln 2$ for $W \lesssim 0.4$ while it decays to the lower value for $W \gtrsim 5$. It is regarded that the transition from the ergodic regime to the MBL regime is observed. (b) Derivative of $\overline{S}_{\rm spin}$. The critical disorder strength W^* (dashed lines) shifts to the larger W side as N increases.

I show the entanglement entropy between the most uncoupled spin and the others $\overline{S}_{\rm spin}$ in Fig. 3.15. The maximal value of $\overline{S}_{\rm spin}$ is $\ln 2$. For $W \lesssim 0.4$, $\overline{S}_{\rm spin}$ reaches to $\ln 2$, that is, fully entangled as in Fig. 3.15(a). $\overline{S}_{\rm spin}$ decays and approaches to the lower value with W increasing. It is regarded that the transition from the ergodic regime (fully entangled regime) to the MBL regime (less entangled regime) is observed. From the derivative of $\overline{S}_{\rm spin}$ with respect to W, I estimate the critical disorder strength W^* as in Fig. 3.15(b) and find that W^* shifts to the larger W as N increases.

Entanglement entropy of the strongest coupled pair of atoms Reference [111] has studied the one-dimensional version of the Hamiltonian (3.9) and proposed the pair model to explain the emergence of non-ergodicity. The pair model is a model that spins form pairs with the nearest spins. In the system where spins position equidistantly, the nearest two spins are hybridized, and then the hybridized spins are again hybridized. After repeating the hybridization, the entanglement spreads over the whole system. In the system where spins position randomly, the spins can be hybridized with the nearest one at once. At that time, the condition that the hybridized spins are again hybridized with the others is not likely to be satisfied. Thus, the entanglement stops when the spins form pairs of the spins, and the pair model is established.

In two dimensions, a spin can be entangled with multiple spins near the spin. Thus, the validity of the pair model is necessary to be checked. To do it, I introduce EE between the strongest coupled pair of the atoms and the others, which is denoted as $S_{\rm pair}$. If the pair picture is valid, the pair is less entangled with the others as W approaches to the non-ergodic region, and equivalently the EE

becomes smaller. I define the strongest coupled pair by finding a pair of the atoms in the closest distance than the other pairs of the atoms.

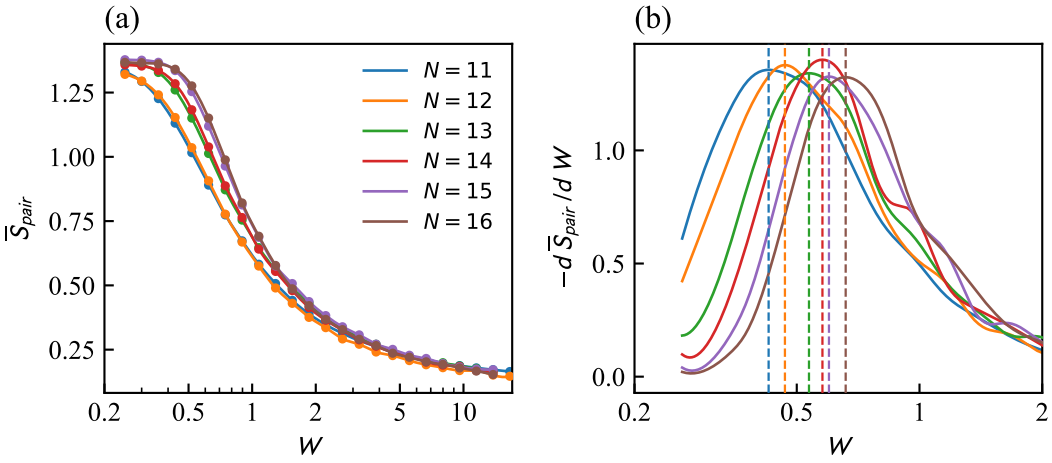

Fig. 3.16 Disorder strength dependence of EE between the most coupled pair and the others. (a) Dependence of EE of the most coupled pair to the others $S_{\rm pair}$ on the disorder strength W. In the small W regime, $S_{\rm pair}$ reaches to the maximum value $\ln 4 \simeq 1.38$, and the system is regarded ergodic. $S_{\rm pair}$ decays as W increases, and approaches the small value for the large W. The relaxed value has no dependence on N. (b) Derivative of $S_{\rm pair}$ with respect to W. The derivative has the maximum around $W \sim 0.5$. The critical disorder strength W^* is denoted as dashed lines. W^* monotonically shifts to the larger W side as N increases.

I show the disorder strength dependence of EE between the strongest pair and the other atoms in Fig. 3.16. $S_{\rm pair}$ decays from the maximal value ($\ln 4$) as W increases as in Fig. 3.16(a). The trend of $S_{\rm pair}$ is regarded to capture the transition from the ergodic side to the non-ergodic side. The derivative reaches to the maximal value around $W \sim 0.5$, and the critical disorder strength W^* is given by W such that the absolute value of the derivative is largest as in Fig. 3.16(b). The critical disorder strength W^* monotonically shifts to the large W side as N increases.

For the small W (the ergodic regime), the pair model is ruined because the strongest coupled pair is well entangled with the others. For the large W (the nonergodic regime), the strongest coupled pair is less entangled with the others, but the entanglement is still finite within the parameter's range of my calculation. The validity of the pair model for the large W cannot be checked by $S_{\rm pair}$. However, I could ensure that $S_{\rm pair}$ works as an ergodicity indicator.

Entanglement entropy of bipartition One of the most used partitions of EE in MBL studies is a way to equally divide a system into two, that is, bipartition. The bipartition is implemented with respect to the number of the atoms, and a bipartitioned subsystem includes a half number of the spins. In other words, the bipartition is not performed with respect to the area in the real space.

It is trivial to define the bipartition in lattice systems. In one dimension, the bipartition can be uniquely determined. In two dimensions, there are many choice of the bipartitions, but their number is limited to few because the spins always locate at the specific positions. On the other hand, in two-dimensional system where the spins locates randomly, the number of the definition of the bipartition is quite large. Furthermore, there is no unique way to automatically determine the bipartition in these

systems. In this way, I adopt two options for the bipartition: geometrically equal half and bipartition by distance.

Before going to the definition of the individual bipartitions, I describe a useful formula with respect to EE. The model in question is a type of $S = 1/2$ XXZ model, the sector where $\hat{Z} = \sum_i \hat{S}_i^z$ is positive and minimum is considered. Specifically, $\hat{Z} = 1$ for the even N, and $\hat{Z} = 1/2$ for the odd N. In the model, the averaged EE of random pure states is given by

$$\begin{aligned}\langle S_{\rm A}\rangle &= -\big(n\ln[n] - (1-n)\ln[1-n]\big)N_{\rm A} - \sqrt{\frac{n(1-n)}{2n}}\left|\ln\left[\frac{1-n}{n}\right]\right|\delta_{N,2N_{\rm A}}\sqrt{N} \\ &\quad + \frac{(N_{\rm A}/N)\big(1-(N_{\rm A}/N)\big)}{2} - \frac{1}{2}\delta_{N,2N_{\rm A}}\delta_{n,1/2} + O(1) \qquad (3.25)\end{aligned}$$

where $n = s^z + 1/2$ with $s^z = \hat{Z}/N$, $N_{\rm A}$ is the number of spins in the subsystem A [112]. I use only the first term to scale the bipartite EE.

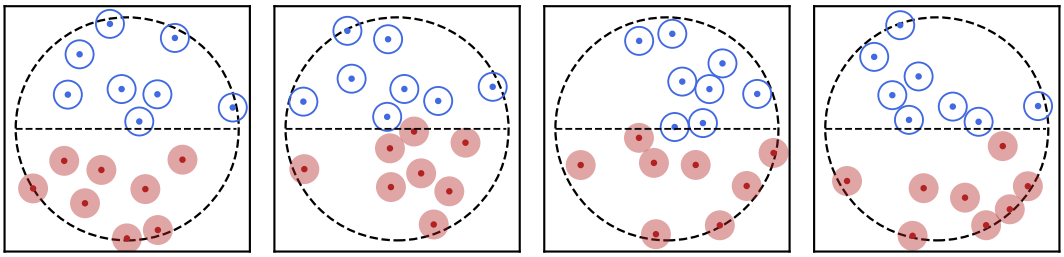

Fig. 3.17 Examples of the geometrically equal half. The unfilled and filled circles participate to the upper and lower halves, respectively. The two halves is divided by a dashed line passing the center of the enclosing circle.

Geometrically equal half The first type of the bipartitions is geometrically equal half. The atoms distribute within the enclosing circle and are subject to the Rydberg blockade. I divide the enclosing circle into two parts by drawing a line passing the center of the enclosing circle as in Fig. 3.17. Here, it is necessary that the half of the atoms and the others participate to the upper and lower half, respectively. The geometrical equal bipartition is implemented as follows. Before generating random configurations of the atoms, the half of the atoms are initialized within the upper (lower) half part of the enclosing circle. When they are displaced, the atoms in the upper (lower) half are imposed not to stick out to the other side. In other words, the atoms are displaced within the semicircles. At the same time that the random configurations are obtained, one obtains lines to divide the systems into two. This bipartition is applied only for the system with a even number of the atoms.

Bipartition by distance The second method of the bipartitions is a bipartition by distance. In the geometrically equal half, the boundaries between the subsystems are drawn by lines. The aim of the bipartition by distance is to pick up bipartitions with various types of the boundaries. To achieve it, I adopt a following method. The main idea is picking up a half number of atoms with smaller distance from a certain point within the enclosing circle. The atoms picked up construct a subsystem.

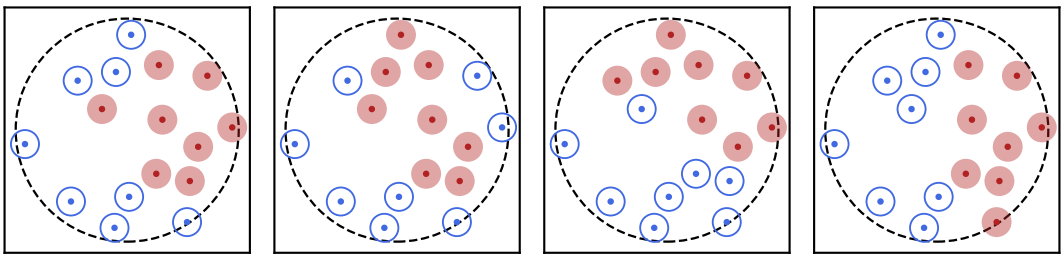

Fig. 3.18 Examples of the bipartition by distance. The unfilled circles denote the atoms participating a subsystem, and the others participate to another subsystem.

When one uses a usual Euclid distance, the shape of the subsystem is close to a circle. Before measuring the distances, I stretch the coordinates of the atoms along with a certain direction (see Appendix). The shape of the subsystems is affected by the direction and the extent in the stretching. The examples of the bipartition by distance are shown in Fig. 3.18. The number of the bipartitions in a random configuration increases as the number of the atoms N increases, and it takes quite long time to calculate EE for all of them. Thus, I set an upper bound to 100 in the number of bipartition in a random configuration.

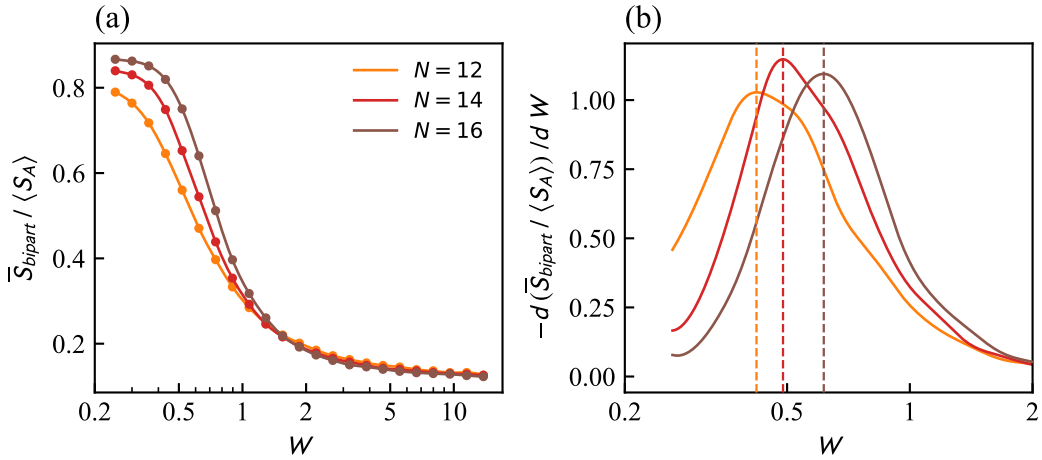

Fig. 3.19 Dependence of EE for the geometrically equal half on the disorder strength and its derivative with respect to the disorder strength. (a) Dependence of the bipartite EE $S_{\rm half}$ on the disorder strength W for $N = 12, 14, 16$ and $N_s = 10^4$. $\overline{S}_{\rm half}$ reaches to $\sim 80\%$ of the averaged EE $\langle S_A \rangle$ for $W \lesssim 0.4$. $S_{\rm half}/\langle S_A \rangle$ decays to a certain value independent on N. (b) Derivative of $S_{\rm half}$ with respect to W. The dashed lines denote the estimated critical disorder strength W^*, which shift to the larger W side as N increases.

I show the results of EE for the two types of the bipartitions in Figs. 3.19 and 3.20. The both bipartite EEs reach higher values for $W \lesssim 0.4$ and decay as W increases. The rescaled EE for the geometrically equal half $\overline{S}_{\rm half}/\langle S_A \rangle$ collapses to a single curve for the sufficiently large disorder strength $W \gtrsim 1.5$ as in Fig.3.19(a). On the other hand, the rescaled EE for the bipartition by distance $\overline{S}_{\rm bipart}/\langle S_A \rangle$ does not collapse a single curve for the large W but has a crossing point at $W \sim 1$ as in Fig. 3.20(a). The corresponding derivatives are shown in Figs. 3.19(b) and 3.20(b). The disorder strength where the derivative is maximum is denoted as the dashed line and is estimated as the critical disorder strength W^*. In the both figures, W^* shifts larger as N increases. The crossing point in

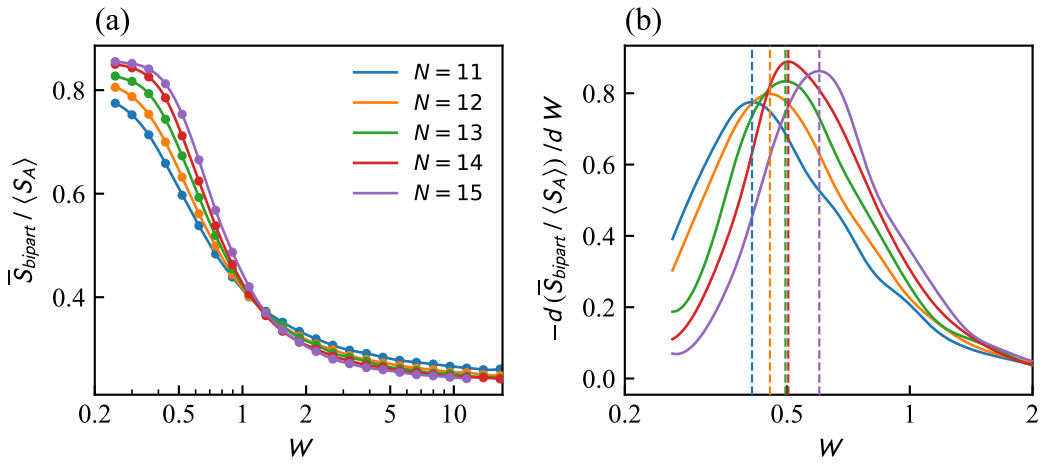

Fig. 3.20 Dependence of EE for the bipartition by distance on the disorder strength and its derivative with respect to the disorder strength. (a) Dependence of the bipartite EE $S_{\rm bipart}$ on the disorder strength W for $N = 11-15$ and $N_s = 5000$. $\overline{S}_{\rm bipart}$ reaches to $\sim 80\%$ of the averaged EE $\langle S_A \rangle$ for $W \lesssim 0.4$. $S_{\rm half}/\langle S_A \rangle$ decays to a lower value. One find a crossing point of the rescaled bipartite EE at $W \sim 1$. W at crossing point does not correspond to the critical disorder strength W^*. (b) Derivative of $S_{\rm bipart}$ with respect to W. The dashed lines denote the estimated critical disorder strength W^*, which shift to the larger W side as N increases.

Fig. 3.20(a) does not correspond to the critical disorder strength W^*.

3.6 Critical disorder strength

In the previous section, I calculate the several indicators and estimate the critical disorder strength W^*. Here, I discuss the dependence of W^* on the number of the spins N. I show the trend of the critical points estimated from the several indicators with respect to N in Fig. 3.21. The suffices of the critical disorder strength in the legend of the figure denote what indicator is used to estimate the critical disorder strength. Specifically, $W^*_{\rm spin}, W^*_{\rm pair}, W^*_{\rm half}$ and $W^*_{\rm bipart}$ are estimated from EEs for the most uncoupled spin, the strongest coupled pair of the spins, the geometrically equal half bipartition and the bipartition by distance, respectively. $W^*_{\rm P}$ is estimated from the partition entropy $S_{\rm P}$. The dots in the figure denote the critical disorder strengths, and the linear lines denote the polynomially fitting lines to W^*. The fitting is performed by the least squares method. The shade is for guide of sight. The y- and x-axis in the figure are taken as the inverses of W^* and N to presume the trend around the infinity W^* and N. One find that all of $1/W^*$ linearly decrease as $1/N$ decreases within the accessible data points by the ED calculation.

The fitting lines provide the presumed trend in the limit $1/N \to 0$ (thermodynamic limit), and $1/W^*$ approaches to 0 in the limit. At $1/N = 0$, $1/W^*$ is smaller than zero, which is an artifact caused from the strong limitation of the system sizes in the ED calculation. I expect that at $1/N = 0$ the fitting line of $1/W^*$ converges to 0 or a positive and finite value if one can calculate the system with a much larger number of the spins. If $1/W^*$ converges to 0 in the thermodynamic limit, the system is ergodic for any strength of disorder, that is, there is no MBL. If $1/W^*$ converges to a positive and finite value in the thermodynamic limit, the system is able to possess MBL for W more than the

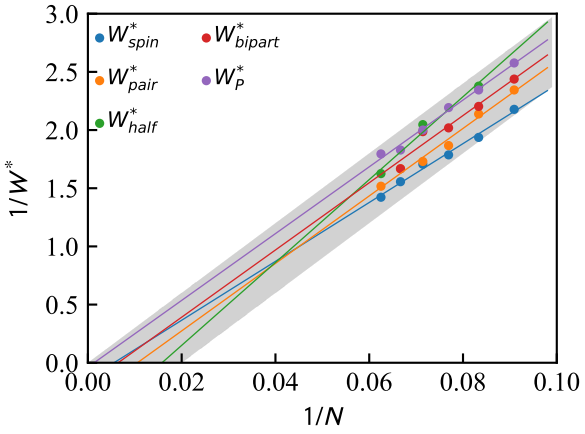

Fig. 3.21 Presumed trend of the critical disorder strength on the number of the spins. $W^*_{\mathrm{spin}}, W^*_{\mathrm{pair}}, W^*_{\mathrm{half}}$ and W^*_{bipart} are estimated from EEs for the most uncoupled spin, the strongest coupled pair of the spins, the geometrically equal half bipartition and the bipartition by distance, respectively. W^*_{P} is estimated from the partition entropy S_{P}. The x-axis and y-axis are set to the inverse number of the spins $1/N$ and the inverse critical disorder strength $1/W^*$, respectively. The dots are the critical disorder strength estimated from the analysis in the last section. The linear lines are fitting lines of the dots by the least squares method.

critical disorder strength. In the case, the critical disorder strength is presumed to be quite large.

3.7 Summary

According to the argument in the thermal avalanche, MBL cannot exist in thermodynamic limit in dimensions higher than one. However, the verification to that is still not sufficient due to the technical bottlenecks in MBL studies. In this study, to study the fate of MBL in thermodynamic limit, I employed the two-dimensional anisotropic Heisenberg model with long-range interaction inspired by the experiments in the Rydberg atoms and calculated the model by ED method.

I analyzed the dependence of the ergodic indicators on the disorder strength and found that the critical disorder strength W^* shifts larger with increasing N. Within the system size in my calculation, the system exhibits the nonergodic crossover. From the trend of $1/W^*$, W^* is presumed to be diverge in the thermodynamic limit or to be quite large. Two scenarios of the fate of MBL in thermodynamic limit can be considered. One is that MBL does not exist in thermodynamic limit. If it is the case, the prediction from the thermal avalanche is supported. The other is that MBL exist but the critical disorder strength is quite large. In the case, the system violates to the argument in the thermal avalanche, and some corrections are required in the theory of the thermal avalanche.

This study is one of the few examples to apply the ED calculation to two-dimensional MBL systems. Nevertheless, the results obtained in this study do not provide a conclusive evidence to answer the question whether MBL exists in thermodynamic limit. Although there is no straightforward method to overcome the technical bottlenecks, further calculations and experiments in the system are required to provide further evidences.

As a future perspective, it is worthwhile to study the matrix elements of observables in the same system. The behavior of the matrix elements of observables directly relates to the validity of ETH.

Another perspective is to study the effect of the power in the interaction. The relation between the space dimension and the power in the interaction would affect to the nonergodicty of the system.

CHAPTER 4

Summary

Studying quantum systems with randomness is tough and undergoing. Roughly speaking, spatial randomness leads to localization, and temporal randomness leads to decoherence. Randomness considered in the past studies is typically idealized and easy to deal with. To understand the effect of randomness to quantum systems, studying systems with special types of randomness is demanded. In this thesis, I have studied two issues relating the relaxation in quantum systems with spatial or temporal randomness.

In Chap. 2, I have studied the relaxation process of the propagation of domain walls. The propagation of the domain walls directly relate to the dynamics of correlation functions and entanglement in the one-particle system. I have analyzed the quasi-periodic Ising model under binary and temporally fluctuating transverse field by the stroboscopic time evolution. As obtained in the paper written by Roósz *et al.*, a domain wall propagates diffusively under the fast fluctuating field while nearly ballistically for a certain interval of the fluctuating field in the uniform model (without quasi-periodicity) [60]. In the system with the quasi-periodicity, the domain wall propagates super-diffusively in short time scale and diffusively in long time. The long time behavior has no dependence on the interval of the fluctuating field. This result can be explained by the stroboscopic eigenstates of the time evolution operators. The time evolution under the binary and temporal random field can be reduced into operating two types of the time evolution operators. For TFIM ($A_J = 0$), a certain state is an eigenstate of both time evolution operators at the same time. Due to the mathematical structure, a specific eigenstate is preserved even under the binary and temporal random field. In contrast, for finite quasi-periodicity ($A_J \neq 0$), such a state no longer exists. As a result, the propagation of a domain wall loses its coherence in long time under the temporal randomness. The spin-spin correlation functions and the half chain entanglement entropy have been checked to have same exponent as that of the propagation of the domain wall.

In Chap. 3, I have studied ergodicity breaking crossover in the anisotropic Heisenberg model inspired by the experiment in the Rydberg atoms [27]. The model has long range interaction decaying with distance between spins. The positions of the spins are random but are subject to the Rydberg blockade, which make the interactions random. Producing random configurations of the spins is implemented by a method based on iterative displacement and gradually expansion of the blockade radius. I have calculated some types of the ergodic indicators and the corresponding derivatives by ED method. As a result, I have found the ergodic-nonergodic crossover and the critical disorder strength shifts larger as the numbers of the spins N increases. By extrapolating the obtained results for the

small numbers of spins ($N = 11 - 16$), I have estimated the behavior of the critical disorder strength in the thermodynamic limit. Of course, I cannot deny that the extrapolation leads to the wrong result. However, since the results in the previous studies of MBL in two dimensions are questionable because of the methodological bottlenecks in the MBL studies, I believe that this study would contributes to studies of the fate of MBL in two dimensions.

I have studied quantum systems with randomness in either spatial or temporal domain. In Chap. 2, I have studied the super-diffusive propagation, which is a conclusion from the mathematical structure of the system. The most naive question is what types of systems possess the super-diffusive propagation protected by eigenvectors of time evolution operators. Apparently, the chiral symmetry is necessary to have symmetric eigenenergies. What is another condition? Is the super-diffusive propagation also seen in many-body systems? In Chap. 3, I have studied MBL in two-dimensional Rydberg atoms. The type of the spatial randomness is configurational and has not yet intensively studied. The uniform randomness or Gaussian randomness have dominantly used for the MBL studies. The strength of these types of randomness is easy to control. On the other hand, the randomness in this study has the distribution depending on the system size, and the statistical property is quite less understood. The maximal systems size in my calculation is limited up to $N = 17$. Since the Rydberg atoms have possibility to be a good testing system of MBL in ED calculation, revealing the statistical properties of that type of randomness is demanded. The ultimate goal of random quantum systems is revealing the universal properties in quantum systems with randomness in spatial/temporal or spatio-temporal domain. Such special types of randomness would provide insight to solve the problem.

Bibliography

[1]P. W. Anderson, "Absence of diffusion in certain random lattices", Phys. Rev. **109**, 1492 (1958).

[2]D. C. Licciardello and D. J. Thouless, "Constancy of minimum metallic conductivity in two dimensions", Phys. Rev. Lett. **35**, 1475 (1975).

[3]D. J. Thouless, "Maximum metallic resistance in thin wires", Phys. Rev. Lett. **39**, 1167 (1977).

[4]E. Abrahams, P. W. Anderson, D. C. Licciardello, and T. V. Ramakrishnan, "Scaling theory of localization: absence of quantum diffusion in two dimensions", Phys. Rev. Lett. **42**, 673 (1979).

[5]F. Evers and A. D. Mirlin, "Anderson transitions", Rev. Mod. Phys. **80**, 1355 (2008).

[6]A. Caldeira and A. Leggett, "Path integral approach to quantum brownian motion", Physica A: Statistical Mechanics and its Applications **121**, 587 (1983).

[7]G. Abal, R. Donangelo, F. Severo, and R. Siri, "Decoherent quantum walks driven by a generic coin operation", Physica A: Statistical Mechanics and its Applications **387**, 335 (2008).

[8]C. M. Chandrashekar, R. Srikanth, and S. Banerjee, "Symmetries and noise in quantum walk", Phys. Rev. A **76**, 022316 (2007).

[9]J. Ko šík, V. Bu žek, and M. Hillery, "Quantum walks with random phase shifts", Phys. Rev. A **74**, 022310 (2006).

[10]D. Shapira, O. Biham, A. J. Bracken, and M. Hackett, "One-dimensional quantum walk with unitary noise", Phys. Rev. A **68**, 062315 (2003).

[11]A. Romanelli, R. Siri, G. Abal, A. Auyuanet, and R. Donangelo, "Decoherence in the quantum walk on the line", Physica A: Statistical Mechanics and its Applications **347**, 137 (2005).

[12]G. Leung, P. Knott, J. Bailey, and V. Kendon, "Coined quantum walks on percolation graphs", New Journal of Physics **12**, 123018 (2010).

[13]A. Ahlbrecht, C. Cedzich, R. Matjeschk, V. B. Scholz, A. H. Werner, and R. F. Werner, "Asymptotic behavior of quantum walks with spatio-temporal coin fluctuations", Quantum Inf. Process **11**, 1219 (2012).

[14]M. Montero, "Classical-like behavior in quantum walks with inhomogeneous, time-dependent coin operators", Phys. Rev. A **93**, 062316 (2016).

[15]C. K. Burrell, J. Eisert, and T. J. Osborne, "Information propagation through quantum chains with fluctuating disorder", Phys. Rev. A **80**, 052319 (2009).

[16]R. Nandkishore and D. A. Huse, "Many-body localization and thermalization in quantum statistical mechanics", Annual Review of Condensed Matter Physics **6**, 15 (2015).

[17]F. Alet and N. Laflorencie, "Many-body localization: an introduction and selected topics", Comptes Rendus Physique **19**, Quantum simulation / Simulation quantique, 498 (2018).

[18]D. A. Abanin, E. Altman, I. Bloch, and M. Serbyn, "Colloquium: many-body localization, thermalization, and entanglement", Rev. Mod. Phys. **91**, 021001 (2019).

[19]M. Schreiber, S. S. Hodgman, P. Bordia, H. P. Lüschen, M. H. Fischer, R. Vosk, E. Altman, U. Schneider, and I. Bloch, "Observation of many-body localization of interacting fermions in a quasirandom optical lattice", Science **349**, 842 (2015).

[20]P. Bordia, H. P. Lüschen, S. S. Hodgman, M. Schreiber, I. Bloch, and U. Schneider, "Coupling identical one-dimensional many-body localized systems", Phys. Rev. Lett. **116**, 140401 (2016).

[21]J.-y. Choi, S. Hild, J. Zeiher, P. Schauß, A. Rubio-Abadal, T. Yefsah, V. Khemani, D. A. Huse, I. Bloch, and C. Gross, "Exploring the many-body localization transition in two dimensions", Science **352**, 1547 (2016).

[22]J. Smith, A. Lee, P. Richerme, B. Neyenhuis, P. W. Hess, P. Hauke, M. Heyl, D. A. Huse, and C. Monroe, "Many-body localization in a quantum simulator with programmable random disorder", Nature Physics **12**, 907 (2016).

[23]P. Roushan, C. Neill, J. Tangpanitanon, V. M. Bastidas, A. Megrant, R. Barends, Y. Chen, Z. Chen, B. Chiaro, A. Dunsworth, A. Fowler, B. Foxen, M. Giustina, E. Jeffrey, J. Kelly, E. Lucero, J. Mutus, M. Neeley, C. Quintana, D. Sank, A. Vainsencher, J. Wenner, T. White, H. Neven, D. G. Angelakis, and J. Martinis, "Spectroscopic signatures of localization with interacting photons in superconducting qubits", Science **358**, 1175 (2017).

[24]A. Lukin, M. Rispoli, R. Schittko, M. E. Tai, A. M. Kaufman, S. Choi, V. Khemani, J. Léonard, and M. Greiner, "Probing entanglement in a many-body–localized system", Science **364**, 256 (2019).

[25]Q. Guo, C. Cheng, H. Li, S. Xu, P. Zhang, Z. Wang, C. Song, W. Liu, W. Ren, H. Dong, R. Mondaini, and H. Wang, "Stark many-body localization on a superconducting quantum processor", Phys. Rev. Lett. **127**, 240502 (2021).

[26]A. Signoles, T. Franz, R. F. Alves, M. Gärttner, S. Whitlock, G. Zürn, and M. Weidemüller, "Glassy dynamics in a disordered heisenberg quantum spin system", Physical Review X **11**, 011011 (2021).

[27]T. Franz, S. Geier, C. Hainaut, A. Signoles, N. Thaicharoen, A. Tebben, A. Salzinger, A. Braemer, M. Gärttner, G. Zürn, and M. Weidemüller, "Absence of thermalization in an interacting system of thousands of quantum spins", arXiv e-prints, arXiv:2207.14216, arXiv:2207.14216 (2022).

[28]V. Oganesyan and D. A. Huse, "Localization of interacting fermions at high temperature", Phys. Rev. B **75**, 155111 (2007).

[29]M. Žnidarič, T. ž. Prosen, and P. Prelov šek, "Many-body localization in the heisenberg XXZ magnet in a random field", Phys. Rev. B **77**, 064426 (2008).

[30]J. Z. Imbrie, V. Ros, and A. Scardicchio, "Local integrals of motion in many-body localized systems", Annalen der Physik **529**, 1600278 (2017).

[31]C. Monthus and T. Garel, "Many-body localization transition in a lattice model of interacting fermions: statistics of renormalized hoppings in configuration space", Phys. Rev. B **81**, 134202 (2010).

[32]S. Welsh and D. E. Logan, "Simple probability distributions on a fock-space lattice", Journal of Physics: Condensed Matter **30**, 405601 (2018).

[33]S. Roy and D. E. Logan, "Fock-space anatomy of eigenstates across the many-body localization transition", Phys. Rev. B **104**, 174201 (2021).

[34]B. Bauer and C. Nayak, "Area laws in a many-body localized state and its implications for topological order", Journal of Statistical Mechanics: Theory and Experiment **2013**, P09005 (2013).

[35]M. Serbyn, Z. Papi ć, and D. A. Abanin, "Local conservation laws and the structure of the many-body localized states", Phys. Rev. Lett. **111**, 127201 (2013).

[36]D. J. Luitz, N. Laflorencie, and F. Alet, "Many-body localization edge in the random-field heisenberg chain", Phys. Rev. B **91**, 081103 (2015).

[37]C. L. Baldwin, C. R. Laumann, A. Pal, and A. Scardicchio, "The many-body localized phase of the quantum random energy model", Phys. Rev. B **93**, 024202 (2016).

[38]K. S. Tikhonov and A. D. Mirlin, "Many-body localization transition with power-law interactions: statistics of eigenstates", Phys. Rev. B **97**, 214205 (2018).

[39]N. Macé, F. Alet, and N. Laflorencie, "Multifractal scalings across the many-body localization transition", Phys. Rev. Lett. **123**, 180601 (2019).

[40]D. Vu, K. Huang, X. Li, and S. Das Sarma, "Fermionic many-body localization for random and quasiperiodic systems in the presence of short- and long-range interactions", Phys. Rev. Lett. **128**, 146601 (2022).

[41]Y. Zhang, B. Zhou, H. Hu, and S. Chen, "Localization, multifractality, and many-body localization in periodically kicked quasiperiodic lattices", Phys. Rev. B **106**, 054312 (2022).

[42]P. Bocchieri and A. Loinger, "Quantum recurrence theorem", Phys. Rev. **107**, 337 (1957).

[43]S. Sachdev and A. P. Young, "Low temperature relaxational dynamics of the ising chain in a transverse field", Phys. Rev. Lett. **78**, 2220 (1997).

[44]H. Rieger and F. Iglói, "Semiclassical theory for quantum quenches in finite transverse ising chains", Phys. Rev. B **84**, 165117 (2011).

[45]M.-C. Chung and I. Peschel, "Density-matrix spectra of solvable fermionic systems", Phys. Rev. B **64**, 064412 (2001).

[46]G. Vidal, J. I. Latorre, E. Rico, and A. Kitaev, "Entanglement in quantum critical phenomena", Phys. Rev. Lett. **90**, 227902 (2003).

[47]J. H. Bardarson, F. Pollmann, and J. E. Moore, "Unbounded growth of entanglement in models of many-body localization", Phys. Rev. Lett. **109**, 017202 (2012).

[48]M. Serbyn, Z. Papi ć, and D. A. Abanin, "Local conservation laws and the structure of the many-body localized states", Phys. Rev. Lett. **111**, 127201 (2013).

[49]M. Knap, "Entanglement production and information scrambling in a noisy spin system", Phys. Rev. B **98**, 184416 (2018).

[50]A. Nahum, J. Ruhman, S. Vijay, and J. Haah, "Quantum entanglement growth under random unitary dynamics", Phys. Rev. X **7**, 031016 (2017).

[51]M. P. Fisher, V. Khemani, A. Nahum, and S. Vijay, "Random quantum circuits", Annual Review of Condensed Matter Physics **14**, 335 (2023).

[52]Y. Aharonov, L. Davidovich, and N. Zagury, "Quantum random walks", Phys. Rev. A **48**, 1687 (1993).

[53]A. Joye and M. Merkli, "Dynamical localization of quantum walks in random environments", J. Stat. Phys **140**, 1025 (2010).

[54]N. Konno, "One-dimensional discrete-time quantum walks on random environments", Quantum Inf. Process **8**, 387 (2009).

[55]N. Konno, "Localization of an inhomogeneous discrete-time quantum walk on the line", Quantum Inf. Process **9**, 405 (2010).

[56]H. Obuse and N. Kawakami, "Topological phases and delocalization of quantum walks in random environments", Phys. Rev. B **84**, 195139 (2011).

[57]A. Ahlbrecht, H. Vogts, A. H. Werner, and R. F. Werner, "Asymptotic evolution of quantum walks with random coin", Journal of Mathematical Physics **52**, 042201 (2011).

[58]O. Mülken and A. Blumen, "Continuous-time quantum walks: models for coherent transport on complex networks", Physics Reports **502**, 37 (2011).

[59]F. Iglói, G. Roósz, and Y.-C. Lin, "Non-equilibrium quench dynamics in quantum quasicrystals", New Journal of Physics **15**, 023036 (2013).

[60]G. ő. Roósz, R. Juhász, and F. Iglói, "Nonequilibrium dynamics of the ising chain in a fluctuating transverse field", Phys. Rev. B **93**, 134305 (2016).

[61]M. Y. Azbel, "Quantum particle in one-dimensional potentials with incommensurate periods", Phys. Rev. Lett. **43**, 1954 (1979).

[62]S. Aubry, and G. André, Ann. Isr. Phys. Soc. **3**, 133 (1980).

[63]S. Ostlund, R. Pandit, D. Rand, H. J. Schellnhuber, and E. D. Siggia, "One-dimensional schrödinger equation with an almost periodic potential", Phys. Rev. Lett. **50**, 1873 (1983).

[64]D. R. Hofstadter, "Energy levels and wave functions of bloch electrons in rational and irrational magnetic fields", Phys. Rev. B **14**, 2239 (1976).

[65]R. Ketzmerick, K. Kruse, F. Steinbach, and T. Geisel, "Covering property of hofstadter's butterfly", Phys. Rev. B **58**, 9881 (1998).

[66]H. Hiramoto and S. Abe, "Dynamics of an electron in quasiperiodic systems. i. fibonacci model", Journal of the Physical Society of Japan **57**, 230 (1988).

[67]F. Piéchon, "Anomalous diffusion properties of wave packets on quasiperiodic chains", Phys. Rev. Lett. **76**, 4372 (1996).

[68]G. ő. Roósz, U. Divakaran, H. Rieger, and F. Iglói, "Nonequilibrium quantum relaxation across a localization-delocalization transition", Phys. Rev. B **90**, 184202 (2014).

[69]S. Ganeshan, J. H. Pixley, and S. Das Sarma, "Nearest neighbor tight binding models with an exact mobility edge in one dimension", Phys. Rev. Lett. **114**, 146601 (2015).

[70]J. Biddle and S. Das Sarma, "Predicted mobility edges in one-dimensional incommensurate optical lattices: an exactly solvable model of anderson localization", Phys. Rev. Lett. **104**, 070601 (2010).

[71]J. Biddle, D. J. Priour, B. Wang, and S. Das Sarma, "Localization in one-dimensional lattices with non-nearest-neighbor hopping: generalized anderson and aubry-andré models", Phys. Rev. B **83**, 075105 (2011).

[72]S. Iyer, V. Oganesyan, G. Refael, and D. A. Huse, "Many-body localization in a quasiperiodic system", Phys. Rev. B **87**, 134202 (2013).

[73]A. Chandran and C. R. Laumann, "Localization and symmetry breaking in the quantum quasiperiodic ising glass", Phys. Rev. X **7**, 031061 (2017).

[74]P. J. D. Crowley, A. Chandran, and C. R. Laumann, "Quasiperiodic quantum ising transitions in 1d", Phys. Rev. Lett. **120**, 175702 (2018).

[75]U. Divakaran, "Sudden quenches in a quasiperiodic ising model", Phys. Rev. E **98**, 032110 (2018).

[76]J. von Neumann, "Beweis des Ergodensatzes und des H-Theorems", Z. Phys. **57**, 30 (1929).

[77]J. L. Lebowitz, "Boltzmann's Entropy and Time's Arrow", Physics Today **46**, 32 (1993).

[78]H. Tasaki, "From quantum dynamics to the canonical distribution: general picture and a rigorous example", Phys. Rev. Lett. **80**, 1373 (1998).

[79]L. D'Alessio, Y. Kafri, A. Polkovnikov, and M. Rigol, "From quantum chaos and eigenstate thermalization to statistical mechanics and thermodynamics", Adv. Phys. **65**, 239 (2016).

[80]J. M. Deutsch, "Quantum statistical mechanics in a closed system", Phys. Rev. A **43**, 2046 (1991).

[81]M. Srednicki, "Chaos and quantum thermalization", Phys. Rev. E **50**, 888 (1994).

[82]M. Rigol, V. Dunjko, V. Yurovsky, and M. Olshanii, "Relaxation in a completely integrable many-body quantum system: an ab initio study of the dynamics of the highly excited states of 1d lattice hard-core bosons", Phys. Rev. Lett. **98**, 050405 (2007).

[83]A. C. Cassidy, C. W. Clark, and M. Rigol, "Generalized thermalization in an integrable lattice system", Phys. Rev. Lett. **106**, 140405 (2011).

[84]D. Basko, I. Aleiner, and B. Altshuler, "Metal–insulator transition in a weakly interacting many-electron system with localized single-particle states", Annals of Physics **321**, 1126 (2006).

[85]C. J. Turner, A. A. Michailidis, D. A. Abanin, M. Serbyn, and Z. Papić, "Weak ergodicity breaking from quantum many-body scars", Nature Physics **14**, 745 (2018).

[86]A. Pal and D. A. Huse, "Many-body localization phase transition", Phys. Rev. B **82**, 174411 (2010).

[87]J. A. Kjäll, J. H. Bardarson, and F. Pollmann, "Many-body localization in a disordered quantum ising chain", Phys. Rev. Lett. **113**, 107204 (2014).

[88]V. Khemani, S. P. Lim, D. N. Sheng, and D. A. Huse, "Critical properties of the many-body localization transition", Phys. Rev. X **7**, 021013 (2017).

[89]P. T. Dumitrescu, R. Vasseur, and A. C. Potter, "Scaling theory of entanglement at the many-body localization transition", Phys. Rev. Lett. **119**, 110604 (2017).

[90]A. Chandran, C. R. Laumann, and V. Oganesyan, "Finite size scaling bounds on many-body localized phase transitions", arXiv: 1509.04285 (2015).

[91]P. T. Dumitrescu, A. Goremykina, S. A. Parameswaran, M. Serbyn, and R. Vasseur, "Kosterlitz-thouless scaling at many-body localization phase transitions", Phys. Rev. B **99**, 094205 (2019).

[92]A. Goremykina, R. Vasseur, and M. Serbyn, "Analytically solvable renormalization group for the many-body localization transition", Phys. Rev. Lett. **122**, 040601 (2019).

[93]A. Morningstar and D. A. Huse, "Renormalization-group study of the many-body localization transition in one dimension", Phys. Rev. B **99**, 224205 (2019).

[94]J. Šuntajs, J. Bon ča, T. ž. Prosen, and L. Vidmar, "Ergodicity breaking transition in finite disordered spin chains", Phys. Rev. B **102**, 064207 (2020).

[95]J. Šuntajs, J. Bon ča, T. ž. Prosen, and L. Vidmar, "Quantum chaos challenges many-body localization", Phys. Rev. E **102**, 062144 (2020).

[96]B. Swingle, "A simple model of many-body localization", arXiv: 1307.0507 (2013).

[97]D. A. Huse, R. Nandkishore, and V. Oganesyan, "Phenomenology of fully many-body-localized systems", Phys. Rev. B **90**, 174202 (2014).

[98]W. De Roeck and F. ç. Huveneers, "Stability and instability towards delocalization in many-body localization systems", Phys. Rev. B **95**, 155129 (2017).

[99]S. Gopalakrishnan and D. A. Huse, "Instability of many-body localized systems as a phase transition in a nonstandard thermodynamic limit", Phys. Rev. B **99**, 134305 (2019).

[100]I.-D. Potirniche, S. Banerjee, and E. Altman, "Exploration of the stability of many-body localization in $d; 1$", Phys. Rev. B **99**, 205149 (2019).

[101]A. Kshetrimayum, M. Goihl, and J. Eisert, "Time evolution of many-body localized systems in two spatial dimensions", Physical Review B **102**, 235132 (2020).

[102]H.-K. Tang, N. Swain, D. C. W. Foo, B. J. J. Khor, G. Lemarié, F. F. Assaad, S. Adam, and P. Sengupta, "Evidence of many-body localization in 2D from quantum Monte Carlo simulation", arXiv e-prints, arXiv:2106.08587, arXiv:2106.08587 (2021).

[103]T. B. Wahl, A. Pal, and S. H. Simon, "Signatures of the many-body localized regime in two dimensions", **15**, 164 (2019).

[104]E. Chertkov, B. Villalonga, and B. K. Clark, "Numerical evidence for many-body localization in two and three dimensions", Phys. Rev. Lett. **126**, 180602 (2021).

[105]K. S. C. Decker, D. M. Kennes, and C. Karrasch, "Many-body localization and the area law in two dimensions", Physical Review B **106**, L180201 (2022).

[106]H. Théveniaut, Z. Lan, G. Meyer, and F. Alet, "Transition to a many-body localized regime in a two-dimensional disordered quantum dimer model", Physical Review Research **2**, 033154 (2020).

[107]F. Pietracaprina and F. Alet, "Probing many-body localization in a disordered quantum dimer model on the honeycomb lattice", SciPost Phys. **10**, 044 (2021).

[108]X. Wu, X. Liang, Y. Tian, F. Yang, C. Chen, Y.-C. Liu, M. K. Tey, and L. You, "A concise review of rydberg atom based quantum computation and quantum simulation*", Chinese Physics B **30**, 020305 (2021).

[109]*The best known packings of equal circles in a circle (complete up to n = 2600)*, `http://hydra.nat.uni-magdeburg.de/packing/cci/cci.html`, 2023.

[110]J. T. Edwards and D. J. Thouless, "Numerical studies of localization in disordered systems", Journal of Physics C: Solid State Physics **5**, 807 (1972).

[111]A. Braemer, T. Franz, M. Weidemüller, and M. Gärttner, "Pair localization in dipolar systems with tunable positional disorder", Phys. Rev. B **106**, 134212 (2022).

[112]E. Bianchi and P. Donà, "Typical entanglement entropy in the presence of a center: page curve and its variance", Phys. Rev. D **100**, 105010 (2019).

Appendices

Appendix A

Basic analysis of transverse field Ising model

The Hamiltonian of transverse field Ising model in one-dimension is

$$\hat{H} = -\frac{J}{2}\sum_{i=1}^{L}\hat{\sigma}_i^x\hat{\sigma}_{i+1}^x - \frac{h}{2}\sum_{i=1}^{L}\hat{\sigma}_i^z, \tag{A.1}$$

where $\hat{\sigma}_i^\alpha$ $(\alpha = x, y, z)$ is a Pauli matrix describing the ith spin, and L is a length of the system. The boundary condition of the system is periodic, that is, $\hat{\sigma}_1^\alpha = \hat{\sigma}_{L+1}^\alpha$.

A.1 Diagonalization

The Hamiltonian can be transformed into a quadratic form of Majorana fermions. The detail transformation is shown as follows. It is well known that Hamiltonian of one-dimensional spin-$1/2$ systems can be written as that of (complex) fermions by Jordan-Wigner transformation. The definition of the fermions is

$$\hat{c}_i = \left(\prod_{k=1}^{i-1}[-\hat{\sigma}_k^z]\right)\hat{\sigma}_i^-, \quad \hat{c}_i^\dagger = \hat{\sigma}_i^+\left(\prod_{k=1}^{i-1}[-\hat{\sigma}_k^z]\right). \tag{A.2}$$

The operators $\hat{c}_i, \hat{c}_i^\dagger$ satisfy anticommutation relation: $\{\hat{c}_i, \hat{c}_j\} = 0$, $\{\hat{c}_i, \hat{c}_j^\dagger\} = \delta_{ij}$. Since $\hat{c}_i^\dagger\hat{c}_i = (1+\hat{\sigma}_i^z)/2$, the inverse transformation of Eq. (A.2) is

$$\hat{\sigma}_i^- = \left(\prod_{k=1}^{i-1}[1-2\hat{c}_k^\dagger c_k]\right)\hat{c}_i, \quad \hat{\sigma}_i^+ = \hat{c}_i^\dagger\left(\prod_{k=1}^{i-1}[1-2\hat{c}_k^\dagger c_k]\right). \tag{A.3}$$

Consider a fermionic form of the first term in Eq. (A.1).

$$\begin{aligned}\hat{\sigma}_i^x\hat{\sigma}_{i+1}^x &= (\hat{\sigma}_i^- + \hat{\sigma}_i^+)(\hat{\sigma}_{i+1}^- + \hat{\sigma}_{i+1}^+) \\ &= (\hat{c}_i + \hat{c}_i^\dagger)(1-2\hat{c}_i^\dagger\hat{c}_i)(\hat{c}_{i+1} + \hat{c}_{i+1}^\dagger) \\ &= (-\hat{c}_i + \hat{c}_i^\dagger)(\hat{c}_{i+1} + \hat{c}_{i+1}^\dagger)\end{aligned} \tag{A.4}$$

Even though the Hamiltonian in the spin language is periodic, the Hamiltonian after transformed is not necessarily periodic. The term spanning over the boundary is $\hat{\sigma}_L^x\hat{\sigma}_{L+1}^x$ in the Hamiltonian, which is equvalent to $\hat{\sigma}_L^x\hat{\sigma}_1^x$ because of the periodic boundary condition. This equality determines the

boundary condition for the spinless fermions. $\hat{\sigma}^x_L\hat{\sigma}^x_{L+1}$ is transformed as

$$\hat{\sigma}^x_L\hat{\sigma}^x_{L+1} = -(\hat{c}_i - \hat{c}^\dagger_i)(\hat{c}_{L+1} + \hat{c}^\dagger_{L+1}), \tag{A.5}$$

while

$$\hat{\sigma}^x_L\hat{\sigma}^x_1 = \left(\prod_{k=1}^{L}[1 - 2\hat{c}^\dagger_k c_k]\right)(\hat{c}_i - \hat{c}^\dagger_i)(\hat{c}_1 + \hat{c}^\dagger_1). \tag{A.6}$$

By comparing Eqs. (A.5) and (A.6), one find

$$(\hat{c}_{L+1} + \hat{c}^\dagger_{L+1}) = -\left(\prod_{k=1}^{L}[1 - 2\hat{c}^\dagger_k c_k]\right)(\hat{c}_1 + \hat{c}^\dagger_1). \tag{A.7}$$

The product $\prod_{k=1}^{L}[1 - 2\hat{c}^\dagger_k c_k]$ works as multiplying -1 if the total number of the spins (spinless fermions) $\hat{N} = \sum_{i=1}^{L}\hat{c}^\dagger_i\hat{c}_i$ is odd. Thus, the boundary condition for the spinless fermions is $\hat{c}_1 = \hat{c}_{L+1}$ for odd $\hat{N}$ or $\hat{c}_1 = -\hat{c}_{L+1}$ for even $\hat{N}$.

After substituting Eq. (A.4) and $\hat{\sigma}^z_i = \hat{c}^\dagger_i\hat{c}_i - \hat{c}_i\hat{c}^\dagger_i$ into Eq. (A.1), one find the spinless fermionic form of the Hamiltonian as

$$\hat{H} = \frac{J}{2}\sum_{i=1}^{L-1}(\hat{c}_i - \hat{c}^\dagger_i)(\hat{c}_{i+1} + \hat{c}^\dagger_{i+1}) + \frac{J}{2}(-1)^{\hat{N}+1}(\hat{c}_L - \hat{c}^\dagger_L)(\hat{c}_1 + \hat{c}^\dagger_1) - \frac{h}{2}\sum_{i=1}^{L}(\hat{c}^\dagger_i\hat{c}_i - \hat{c}_i\hat{c}^\dagger_i). \tag{A.8}$$

The Fourier transformation makes the Hamiltonian simpler as

$$\tilde{c}_k = \frac{\mathrm{e}^{-i\phi}}{\sqrt{L}}\sum_{j=1}^{L}\mathrm{e}^{-i\tilde{k}j}\hat{c}_j, \tag{A.9}$$

where $\tilde{k} = 2\pi k/L$ $(k = -L/2+1, \cdots, L/2)$ for odd $\hat{N}$ or $\tilde{k} = \pm\pi(2k-1)/L$ $(k = 1, \cdots, L/2)$ for even $\hat{N}$. Here, I consider the situation where $\hat{N}$ is even through this sector. The Hamiltonian is transformed into

$$\begin{aligned}\hat{H} = \sum_{k=1}^{L/2}\{&-J\cos\tilde{k}\ \tilde{c}^\dagger_k\tilde{c}_k + J\cos\tilde{k}\ \tilde{c}_{-k}\tilde{c}^\dagger_{-k} - i\mathrm{e}^{-i2\phi}\sin\tilde{k}\ \tilde{c}^\dagger_k\tilde{c}^\dagger_{-k} + i\mathrm{e}^{i2\phi}\sin\tilde{k}\ \tilde{c}_{-k}\tilde{c}_k \\ &-h\ \tilde{c}^\dagger_k\tilde{c}_k + h\ \tilde{c}_{-k}\tilde{c}^\dagger_{-k}\}.\end{aligned} \tag{A.10}$$

After implementing a Bogoliubov transformation by using a fermionic two-component spinor defined as

$$\Psi_k = \begin{bmatrix}\tilde{c}_k \\ \tilde{c}^\dagger_{-k}\end{bmatrix}, \quad \Psi^\dagger_k = \begin{bmatrix}\tilde{c}^\dagger_k & \tilde{c}_{-k}\end{bmatrix}, \tag{A.11}$$

the Hamiltonian is reduced as

$$\hat{H} \;=\; \sum_{k=1}^{L/2} \Psi_k^\dagger \mathrm{H}_k \Psi_k, \tag{A.12}$$

where the matrix

$$\mathrm{H}_k = \begin{bmatrix} -J\cos\tilde{k} - h & -i\mathrm{e}^{-i2\phi} J\sin\tilde{k} \\ i\mathrm{e}^{i2\phi} J\sin\tilde{k} & J\cos\tilde{k} + h \end{bmatrix}. \tag{A.13}$$

From here, ϕ is set to 0 for simplicity. The matrix H_k is diagonalized into

$$\mathrm{H}_k = \mathrm{U}_k \Lambda_k \mathrm{U}_k^\dagger, \tag{A.14}$$

where

$$\mathrm{U}_k = \frac{1}{\sqrt{2\epsilon_k(\epsilon_k + J\cos\tilde{k} + h)}} \begin{bmatrix} -iJ\sin\tilde{k} & \epsilon_k + (J\cos\tilde{k} + h) \\ \epsilon_k + (J\cos\tilde{k} + h) & -iJ\sin\tilde{k} \end{bmatrix}, \tag{A.15}$$

and $\Lambda_k = \mathrm{diag}[+\epsilon_k, -\epsilon_k]$ for $\epsilon_k = \sqrt{J^2 + 2Jh\cos\tilde{k} + h^2}$. One can get the final form of the Hamiltonian is

$$\hat{H} = \sum_{k=1}^{L/2} \Phi_k^\dagger \Lambda_k \Phi_k = \sum_{k=1}^{L/2} \epsilon_k \{\hat{b}_k^\dagger \hat{b}_k + \hat{b}_{-k}^\dagger \hat{b}_{-k} - 1\}, \tag{A.16}$$

where $\Phi_k = [\hat{b}_k, \hat{b}_{-k}^\dagger]^{\mathrm{t}} = \mathrm{U}_k^\dagger \Psi_k$.

A.2 Eigenstates

The eigenstates of the Hamiltonian are characterized by the number of the particle labeled by k.

The groundstate of the Hamiltonian is a vacuum state for the Bogoliubov particle. Here, the vacuum state is denoted as $|\emptyset\rangle_{\mathrm{B}}$ and satisfies

$$\hat{b}_k |\emptyset\rangle_{\mathrm{B}} = 0, \quad \text{for} \quad k = 1, \cdots, L/2. \tag{A.17}$$

The corresponding eigenenergy is

$$E_{\mathrm{G}} = -\sum_{k=1}^{L/2} \epsilon_k. \tag{A.18}$$

The vacuum state $|\emptyset\rangle_{\mathrm{B}}$ can be written in an explicit form as

$$|\emptyset\rangle_{\mathrm{B}} \propto \prod_{k=1}^{L/2} \hat{b}_k \hat{b}_{-k} |\emptyset\rangle\,, \tag{A.19}$$

where $|\emptyset\rangle$ is a vacuum state for the original spin operators.

A.3 Description of Majorana fermion

Here, I introduce Majorana fermions defined as

$$\hat{\gamma}_{2j-1} = \hat{c}_i + \hat{c}_i^\dagger, \quad \hat{\gamma}_{2j} = -i(\hat{c}_i - \hat{c}_i^\dagger). \tag{A.20}$$

The Majorana fermions satisfy the anti-commutation relation

$$\{\hat{\gamma}_i, \hat{\gamma}_j\} = 2\delta_{ij}, \tag{A.21}$$

and the boundary condition holds after the Majoranization:

$$\gamma_1 = (-1)^{\hat{N}}\gamma_{2L-1}, \quad \gamma_2 = (-1)^{\hat{N}}\gamma_{2L}. \tag{A.22}$$

The Hamiltonian can be written by the Majorana fermions as

$$\begin{aligned} \hat{H} &= i\frac{J}{2}\sum_{i=1}^{L-1}\hat{\gamma}_{2i}\hat{\gamma}_{2i+1} + i\frac{J}{2}(-1)^{\hat{N}+1}\hat{\gamma}_{2L}\hat{\gamma}_1 - i\frac{h}{2}\sum_{i=1}^{L}\hat{\gamma}_{2i-1}\hat{\gamma}_{2i} \\ &= \frac{1}{4}\sum_{m,n=1}^{2L}\hat{\gamma}_m\mathbb{H}_{mn}\hat{\gamma}_n, \end{aligned} \tag{A.23}$$

where the tridiagonal and skew matrix whose dimension is $2L$

$$\mathbb{H} = \begin{bmatrix} 0 & +ih & 0 & 0 & 0 & \cdots & 0 & (-1)^{\hat{N}+2}iJ \\ -ih & 0 & -iJ & 0 & 0 & \cdots & 0 & 0 \\ 0 & +iJ & 0 & +ih & 0 & \cdots & 0 & 0 \\ 0 & 0 & -ih & 0 & -iJ & \cdots & 0 & 0 \\ 0 & 0 & 0 & +iJ & 0 & \cdots & 0 & 0 \\ \vdots & \vdots & \vdots & \vdots & \vdots & \ddots & \vdots & \vdots \\ 0 & 0 & 0 & 0 & 0 & \cdots & 0 & +ih \\ (-1)^{\hat{N}+1}iJ & 0 & 0 & 0 & 0 & \cdots & -ih & 0 \end{bmatrix}. \tag{A.24}$$

The matrix can be diagonalized by using eigenvectors

$$\vec{v}_k^{\pm} = \mathcal{A}\begin{bmatrix} \mathrm{e}^{i\Theta_k}\mathrm{e}^{i\tilde{k}} \\ \pm\mathrm{e}^{-i\Theta_k}\mathrm{e}^{i\tilde{k}} \\ \mathrm{e}^{i\Theta_k}\mathrm{e}^{i2\tilde{k}} \\ \pm\mathrm{e}^{-i\Theta_k}\mathrm{e}^{i2\tilde{k}} \\ \mathrm{e}^{i\Theta_k}\mathrm{e}^{i3\tilde{k}} \\ \pm\mathrm{e}^{-i\Theta_k}\mathrm{e}^{i3\tilde{k}} \\ \vdots \\ \mathrm{e}^{i\Theta_k}\mathrm{e}^{iL\tilde{k}} \\ \pm\mathrm{e}^{-i\Theta_k}\mathrm{e}^{iL\tilde{k}} \end{bmatrix}, \quad \tan(2\Theta_k) = -\frac{J\sin\tilde{k}}{J\cos\tilde{k}+h}, \quad \mathcal{A} = \frac{1}{2\sqrt{L}}, \tag{A.25}$$

and the corresponding eigenenergy is $\pm\epsilon_k = \pm\sqrt{J^2 + 2Jh\cos\tilde{k} + h^2}$. All of the eigenfunctions are labeled by wave-number k and fully delocalized.

A.4 Quasi-periodic transverse field Ising model (QP-TFIM)

The Hamiltonian describing QP-TFIM is defined in Eq. 2.21. To calculate the time evolution of the Majorana fermion $\hat{\gamma}_\mu$, one need to obtain the quadratic form of the Majorana fermion from the Hamiltonian in Eq. 2.21

$$\hat{H} = \frac{1}{4}\sum_{\mu=1}^{2L}\hat{\gamma}_\mu[\mathsf{H}]_{\mu\nu}\hat{\gamma}_\nu, \tag{A.26}$$

where

$$\mathsf{H} = \begin{bmatrix} 0 & +ih & 0 & 0 & 0 & \cdots & 0 & 0 \\ -ih & 0 & -iJ_{1+1/2} & 0 & 0 & \cdots & 0 & 0 \\ 0 & +iJ_{1+1/2} & 0 & +ih & 0 & \cdots & 0 & 0 \\ 0 & 0 & -ih & 0 & -iJ_{2+1/2} & \cdots & 0 & 0 \\ 0 & 0 & 0 & +iJ_{2+1/2} & 0 & \cdots & 0 & 0 \\ \vdots & \vdots & \vdots & \vdots & \vdots & \ddots & \vdots & \vdots \\ 0 & 0 & 0 & 0 & 0 & \cdots & 0 & +ih \\ 0 & 0 & 0 & 0 & 0 & \cdots & -ih & 0 \end{bmatrix}. \tag{A.27}$$

Since the Hamiltonian in Eq. 2.21 is in open boundary condition, the components at $(1, 2L)$ and $(2L, 1)$ are zero. The matrix H cannot by diagonalized analytically.

Appendix B

Thermalization in Isolated Quantum Systems

Here, I describe a standard formalism of thermalization in isolated quantum systems. The description here are mainly quoted from Refs. **??** and **??**. In Sec. B.1, I review the microcanonical ensemble to describe equilibrium states in isolated systems. In Sec. **??**, I introduce random matrix theory (RMT) that provides an example of a thermalizing system. However, observables described in RMT have no dependence on energy, and the thermalizing time does not depend on observables. These points do not fit with the features in the microcanonical ensemble. In Sec. **??**, I introduce eigenstate thermalization hypothesis (ETH) to overcome these points.

B.1 Statistical mechanics

Here, I outline a standard part of the statistical mechanics, especially microcanonical ensemble (MCE). To obtain observables in macroscopic quantum systems, one needs to diagonalize the Hamiltonian with exponentially large dimensions with the system sizes. However, it is almost impossible to implement numerical computations of these systems because the dimension of Hamiltonian is much larger than that one can deal with. In the case, one can utilize statistical mechanics, which describes macroscopic observables without dealing with the details of the systems.

For concreteness, consider an isolated quantum system whose Hamiltonian is denoted as $\hat{H}$. I denote the nth eigenstate as $|n\rangle$ of $\hat{H}$ and the corresponding eigenenergy as E_n for $n = 1, \cdots, \mathcal{D}$ with the Hilbert space dimension $\mathcal{D}$. Any quantum state can be decomposed into a linear combination of the eigenstates as $|\psi\rangle = \sum_{n=1}^{\mathcal{D}} \psi_n |n\rangle$. An expectation value of an observable to the state $|\psi\rangle$ can be calculated as $\langle \hat{O} \rangle = \langle \psi | \hat{O} | \psi \rangle = \sum_{m,n=1}^{\mathcal{D}} \psi_m^* \psi_n \langle m | \hat{O} | n \rangle$. Calculation of $\langle \hat{O} \rangle$ is a easy task in small sized systems (D is small) but is quite difficult in large sized systems.

One can overcome the difficulty by assuming MCE. A central principle in MCE is the principle of equal weight. The principle states that quantum states within an energy window with the center E and the width δE appear with a same probability $p(E)$. Providing the number of quantum states within the window $W(E, \delta E)$, the probability is $p(E) = 1/W(E, \delta E)$ By using the principle, the expectation value in a system with energy E is give by

$$O_{\mathrm{MCE}}(E) = \frac{1}{W(E, \delta E)} \sum_{|E_n - E| < \delta E} \langle n | \hat{O} | n \rangle . \tag{B.1}$$

The microcanonical description can also be written in

$$O_{\mathrm{MCE}}(E) = \mathrm{Tr}[\hat{O}\hat{\rho}_{\mathrm{MCE}}], \tag{B.2}$$

where $\hat{\rho}_{\mathrm{MCE}} = \frac{1}{W(E,\delta E)} \sum_{|E_n - E| < \delta E} |n\rangle \langle n|$ is a density matrix corresponding to the uniform probability distribution within the energy shell. Note that $\hat{\rho}_{\mathrm{MCE}}$ is a mixed state.

MCE in Eq. (B.1) successfully works for many situations, for example condensed matter physics. However, there is no rigorous proof for the validity of the principle of equal weight, and there are different types of formalism without assuming the principle of equal weight.

B.2 Thermalization

Thermalization is relaxation of observables to thermal values predicted by statistical mechanics. Specifically, in isolated quantum systems, the thermal values are derived from MCE above mentioned. In this section, I describe thermalization from view point of quantum mechanics.

Let us consider time evolution starting from an initial state $|\psi\rangle$ under Hamiltonian $\hat{H} = \sum_{n=1}^{\mathcal{D}} E_n |n\rangle \langle n|$. The state at time t can be written in

$$|\psi(t)\rangle = \sum_{n=1}^{\mathcal{D}} \psi_n \mathrm{e}^{-iE_n t} |n\rangle , \tag{B.3}$$

where $\langle n|\psi\rangle = \psi_n$. Apparently, a quantum state $|\psi\rangle$ itself never becomes a mixed state like MCE under unitary time evolution $\mathrm{e}^{-\mathrm{i}\hat{H}t}$ because the purity of the state $\gamma = \mathrm{Tr}[(|\psi\rangle \langle\psi|)^2]$ is conserved in 1. (The purity γ is an indicator to distinguish a state is pure or mixed. The state is pure for $\gamma = 1$ while is mixed for $\gamma < 1$.) Although a quantum state describing a whole system never relaxes to a mixed state, it is possible that an expectation value of a local observable coincides to a prediction by MCE. When observing a local observable, it possibly happens that two quantum states are indistinguishable in the sense of local quantities. For concreteness, the subsystem where the local observables belongs is denoted as A, and the remained part of the whole system is denoted as $\bar{A}$. After tracing out degrees of freedom in $\bar{A}$, one obtain the partial density matrix

$$\hat{\rho}_A = \mathrm{Tr}_{\bar{A}}[|\psi\rangle \langle\psi|]. \tag{B.4}$$

$\hat{\rho}$ contains all information to describe the observables within the subsystem A. Unlike the quantum state in the whole system $|\psi\rangle$, the purity of $\hat{\rho}_A$ can be less than 1, and the subsystem A is entangled with the remained part $\bar{A}$. If $\hat{\rho}_A \simeq \mathrm{Tr}_{\bar{A}}[\hat{\rho}_{\mathrm{MCE}}]$, MCE is justified within the local degrees of freedom. It has been proved that almost all states within the energy shell coincide with ρ_{MCE} in the sense of local subsystems if the size of the local subsystems is much smaller than the size of the whole system. Such property that almost all quantum states coincide with a thermal state is called as thermal typicality. I emphasize that the thermal typicality does not solve the problem of thermalization. The thermal typicality is proved to hold for any systems with a large number of degrees of freedom, which is inconsistent with the fact that macroscopic systems do not necessarily thremalize.

To obtain insights about thermalization in isolated quantum systems, let us start with an expectation value of an observable $\hat{O} = \sum_{i=1}^{\mathcal{D}} O_i \left|i\right\rangle \left\langle i\right|$ at time t

$$\langle \hat{O}(t) \rangle \quad = \quad \langle \psi(t) | \hat{O} | \psi(t) \rangle = \sum_{m=1}^{\mathcal{D}} \sum_{n=1}^{\mathcal{D}} \psi_m^* \psi_n \mathrm{e}^{i(E_m - E_n)t} O_{mn}, \tag{B.5}$$

where $O_{mn} = \langle m | \hat{O} | n \rangle$. Note that the basis $|i\rangle$ is not necessarily same as $|n\rangle$. $\langle \hat{O}(t) \rangle$ can be divided into a stationary and dynamical terms as

$$\langle \hat{O}(t) \rangle = \sum_{m=1}^{\mathcal{D}} |\psi_m|^2 O_{mm} + \sum_{m=1}^{\mathcal{D}} \sum_{\substack{n=1 \\ n \neq m}}^{\mathcal{D}} \psi_m^* \psi_n \mathrm{e}^{i(E_m - E_n)t} O_{mn}. \tag{B.6}$$

The problem of thermalization is equivalent to whether a long time limit $\lim_{t\to\infty} \langle \hat{O}(t) \rangle$ coincides to a prediction from MCE. Instead of taking the long time limit, consider a long time average

$$\overline{O} := \lim_{T\to\infty} \frac{1}{T} \int_0^T \mathrm{d}t \, \langle \hat{O}(t) \rangle. \tag{B.7}$$

It is obvious that, if $\langle \hat{O}(t) \rangle$ converges a certain value in long time limit, the long time average $\overline{O}$ also converges to the same value.

The explicit form of the long time average is

$$\overline{O} = \sum_{m=1}^{\mathcal{D}} |\psi_m|^2 O_{mm} + \sum_{m=1}^{\mathcal{D}} \sum_{\substack{n=1 \\ n \neq m}}^{\mathcal{D}} \psi_m^* \psi_n O_{mn} \left\{ \lim_{T\to\infty} \frac{1}{T} \int_0^T \mathrm{d}t \, \mathrm{e}^{i(E_m - E_n)t} \right\}. \tag{B.8}$$

The second term vanished after taking the limit for generic quantum systems after removing all trivial symmetries. In the case, Eq. B.8 is reduced to

$$\overline{O} = \sum_{m=1}^{\mathcal{D}} |\psi_m|^2 O_{mm} = \mathrm{Tr}[\hat{O}\hat{\rho}_{\mathrm{DE}}], \tag{B.9}$$

where the density matrix of the diagonal ensemble (DE) $\hat{\rho}_{\mathrm{DE}} = \sum_m |\psi_m|^2 \left|m\right\rangle \left\langle m\right|$. The statement of thermalization of an observable $\hat{O}$ is equivalent to

$$\overline{O} \simeq O_{\mathrm{MCE}}. \tag{B.10}$$

To check the convergence of the observable $\hat{O}$, calculate a variance in the sense of the long time averaging

$$\delta O^2 := \overline{O^2} - \overline{O}^2. \tag{B.11}$$

$\bar{\cdot}$ denotes the long time average. If δO^2 converges to infinitesimal value, the observable is regarded as

converges. The variance is calculated as

$$\begin{aligned}\delta O^2 &= \sum_{m\neq n}\sum_{k\neq l}\psi_m^*\psi_n\psi_k^*\psi_l O_{mn}O_{kl}\overline{\mathrm{e}^{\mathrm{i}(E_m-E_n+E_k-E_l)t}} = \sum_{m\neq n}\sum_{k\neq l}\psi_m^*\psi_n\psi_k^*\psi_l O_{mn}O_{kl}\delta_{E_m,E_n}\delta_{E_k,E_l} \\ &= \sum_{m\neq n}|\psi_m|^2|\psi_n|^2|O_{mn}|^2. \end{aligned} \tag{B.12}$$

When taking the long time average, the nonresonant condition

$$E_m - E_n = E_k - E_l \neq 0 \Rightarrow m = k \text{ and } n = l \tag{B.13}$$

is assumed. Furthermore, the variance is bounded as

$$\delta O^2 \leqslant \sum_m |\psi_m|^4 \langle n|\hat{O}\hat{O}^\dagger|n\rangle \leqslant \frac{||\hat{O}||^2}{\mathcal{D}_{\text{eff}}} \tag{B.14}$$

by using the inequality of the arithmetic mean and the geometric mean. The effective dimension $\mathcal{D}_{\text{eff}}$ is defined as $\left(\sum_m |\psi_m|^4\right)^{-1}$. The effective dimension is typically quite large for many-body systems, therefore an observable converges in long time for a majority of initial states in quantum many-body systems satisfying the nonresonant condition.

However, there is two natural questions in the above discussion: (1) Since $|\psi_m|^2$ is conserved through unitary time evolution, how does DE coincide with MCE? (2) In many-body systems, since the difference of the energy levels are exponentially small with the system sizes,the time that the second term vanishes is exponentially large. How do systems in nature overcome that problem of time to take thermalization.

B.3 Random matrix theory

Here, I introduce random matrix theory. In systems described by random matrix theory, the long time average of an observable converges without the difficulty in taking time.

B.3.1 Introduction of random matrix theory

The main idea of RMT can be understood using 2×2 matrix

$$\hat{H} = \begin{bmatrix} \epsilon_1 & \frac{V}{\sqrt{2}} \\ \frac{V^*}{\sqrt{2}} & \epsilon_2 \end{bmatrix}, \tag{B.15}$$

where the individual matrix elements $\epsilon_1, \epsilon_2, \mathrm{Re}(V)$ and $\mathrm{Im}(V)$ are random variables of a Gaussian distribution. After diagonalization, one obtain the eigenvalues

$$E_{1,2} = \frac{\epsilon_1+\epsilon_2}{2} \pm \frac{1}{2}\sqrt{(\epsilon_1-\epsilon_2)^2+2|V|^2}. \tag{B.16}$$

A statistical property of a gap of the eigenenergies is important and depends highly on a symmetry of the system. If the system has time reversal symmetry, $V = V^*$. For simplicity, all the random variables ϵ_1, ϵ_2 and V follow a Gaussian distribution with zero mean and variance σ^2. The probability that the energy gap $E_1 - E_2$ equals ω can be evaluated as

$$P(\omega) = \frac{1}{(2\pi)^{3/2}\sigma^3} \int \mathrm{d}\epsilon_1 \mathrm{d}\epsilon_2 \mathrm{d}V \delta\Big(\omega - \sqrt{(\epsilon_1 - \epsilon_2)^2 + 2|V|^2}\Big) \exp\Big(-\frac{\epsilon_1^2 + \epsilon_2^2 + V^2}{2\sigma^2}\Big). \quad \text{(B.17)}$$

After calculation the integral and setting σ as the mean level spacing is unite, one can easily obtain

$$P_{\beta=1}(\omega) = \frac{\pi}{2}\omega \exp\Big(-\frac{\pi}{4}\omega^2\Big). \quad \text{(B.18)}$$

If time reversal symmetry is absent, that is, $V \neq V^* \in \mathbb{C}$, the probability distribution is given by

$$P_{\beta=2}(\omega) = \frac{32}{\pi^2}\omega^2 \exp\Big(-\frac{4}{\pi}\omega^2\Big). \quad \text{(B.19)}$$

The indices β in Eqs. (B.18) and (B.19) correspond to the class of symmetry. $\beta = 1$ and 2 correspond to Gaussian orthogonal ensemble (GOE) and Gaussian unitary ensemble (GUE), respectively. I emphasize that the probability distribution is zero at $\omega = 0$. This means that the two energy levels are subject to level repulsion. The eigenenergies are correlated even if the matrix elements are random and uncorrelated.

The above argument is known to hold for larger matrices. To extend the 2×2 random matrix to the larger matrix, one can define an ensemble of matrices whose elements follow a Gaussian distribution:

$$P(\hat{H}) \propto \exp\Big(-\frac{\beta}{2a^2}\sum_{ij} H_{ij}H_{ji}\Big), \quad \text{(B.20)}$$

where a is set to the overall energy scale. $\hat{H}$ satisfies $H_{ij} = H_{ji}$ for GOE and $H_{ij} = H_{ji}^*$ for GUE. I will not discuss the details for the distribution in Eq. (B.20), but $P(\hat{H})$ is qualitatively and quantitatively close to Eqs. (B.18) and (B.19).

B.3.2 Eigenvectors in random matrix theory

In RMT, eigenvectors are defined as random and unit vectors in Hilbert space. The Hilbert space is real (complex) $\mathcal{D}$ dimensional space for GOE (GUE). The eigenvectors are formulated in probabilities as

$$P_{\beta=1}(\psi_1, \cdots, \psi_{\mathcal{D}}) \propto \delta\Big(\sum_{i=1}^{\mathcal{D}} \psi_i^2 - 1\Big), \quad P_{\beta=2}(\psi_1, \cdots, \psi_{\mathcal{D}}) \propto \delta\Big(\sum_{i=1}^{\mathcal{D}} |\psi_i|^2 - 1\Big), \quad \text{(B.21)}$$

where ψ_i is the components in real or complex vectors. Although an eigenvector in Eq. (B.21) is not orthogonalized with each other, it can be regarded as orthogonal in the large dimensions because two eigenvectors become uncorrelated as the dimension increases.

B.3.3 Structure of matrix elements of observables

Since we have eigenvectors of systems described by RMT, we can calculate structure of an observable in the system. Let us denote an observable as

$$\hat{O} = \sum_{i=1}^{\mathcal{D}} O_i \left|i\right\rangle \left\langle i\right|, \tag{B.22}$$

where O_i is an eigenvalue of the observable, and $|i\rangle$ is the corresponding eigenvector. Note that $|i\rangle$ is not necessarily same as the eigenvectors of Hamiltonian. As in Eq. (B.6), the matrix elements $O_{mn} = \langle m| \hat{O} |n\rangle$ play an important role in the time-evolution. Here, $|m\rangle$ is an eigenstate of given Hamiltonian. O_{mn} is given by

$$O_{mn} = \langle m| \hat{O} |n\rangle = \sum_i \langle m|i\rangle \langle i|n\rangle O_i = \sum_i (\psi_i^m)^* \psi_i^n O_i, \tag{B.23}$$

where $\psi_i^m = \langle i|m\rangle$. The eigenstates of random matrices are random and unit vectors that is orthogonal to other vectors in any basis. Thus, after taking the average with respect to the eigenstate $|m\rangle$ and $|n\rangle$, one find

$$\langle (\psi_i^m)^* \psi_j^n \rangle = \frac{1}{\mathcal{D}} \delta_{mn} \delta_{ij}, \tag{B.24}$$

where $\mathcal{D}$ is the dimension of the Hilbert space. $\langle \cdot \rangle$ denotes averaging over the eigenstates of Hamiltonian $|m\rangle$. By using it, O_{mn} averaged over $|m\rangle$ and $|n\rangle$ reads

$$\langle O_{mm} \rangle = \frac{1}{D} \sum_i O_i \equiv \bar{O}, \tag{B.25}$$

$$\langle O_{mm} \rangle = 0 \quad \text{for} \quad m \neq n. \tag{B.26}$$

Note that the notation $\bar{O} = \sum_i O_i / \mathcal{D}$ is different from the notation of the long time average $\overline{O}$. The mean values of O_{mn}, which is denoted as $\bar{O}$ has been determined.

The next step is estimating variance of O_{mn}. For GOE, the variance of the diagonal elements is given by

$$\begin{aligned} \langle O_{mm}^2 \rangle - \langle O_{mm} \rangle^2 &= \sum_{ij} O_i O_j \langle (\psi_i^m)^2 (\psi_j^m)^2 \rangle - \sum_{ij} O_i O_j \langle (\psi_i^m)^2 \rangle \langle (\psi_j^m)^2 \rangle \\ &= \sum_i O_i^2 \Big(\langle (\psi_i^m)^4 \rangle - \langle (\psi_i^m)^2 \rangle^2 \Big) = \frac{2}{\mathcal{D}^2} \sum_i O_i^2, \end{aligned} \tag{B.27}$$

where the relation $\langle (\psi_i^m)^4 \rangle = 3 \langle (\psi_i^m)^2 \rangle^2$ is used. The variance of the off diagonal elements is given by

$$\langle O_{mn}^2 \rangle - \langle O_{mn} \rangle^2 = \sum_{ij} O_i O_j \langle (\psi_i^m)^2 (\psi_j^n)^2 \rangle = \frac{1}{\mathcal{D}^2} \sum_i O_i^2. \tag{B.28}$$

Combining the mean and the variance of O_{mn}, one can obtain

$$O_{mn} \simeq \bar{O}\delta_{mn} + \sqrt{\frac{\bar{O^2}}{\mathcal{D}}} R_{mn}, \tag{B.29}$$

where $\bar{O^2} = \sum_i O_i^2/\mathcal{D}$, and R_{mn} is a random number with zero mean and unit variance (for the diagonal elements the variance of R_{mm} is 2).

Providing Eq. B.29, the dynamical term in Eq. B.8 vanishes after taking the limit of the large system size $\mathcal{D} \to \infty$. In other words, systems described by RMT overcome the problem that the relaxation time is exponentially large with system sizes. Furthermore, the expectation value of the observable in the diagonal ensembles reads

$$\mathrm{Tr}[\hat{O}\hat{\rho}_{\mathrm{DE}}] = \sum_m \psi_m O_{mm} \simeq \bar{O} \sum_m |\psi_m|^2 = \bar{O}. \tag{B.30}$$

The result equals to $\bar{O}$ being independent on the distribution of $\{|\psi_m|^2\}$.

Systems described by RMT still have inconsistent points to MCE. While the statistical mean predicted by MCE depends on energies of the whole systems, the expectation values after relaxed in RMT do not depend on energies. The relaxation time should depend on observables, which can not be reproduced by RMT.

B.4 Eigenstate thermalization hypothesis

Eigenstate themalization hypothesis (ETH) is an ansatz for the matrix elements of observables $O_{mn} = \langle m| \hat{O} |n\rangle$ with the eigenstates of a Hamiltonian $\hat{H}$. ETH argues that O_{mn} follows

$$O_{mn} = O(\bar{E})\delta_{mn} + \mathrm{e}^{-\mathrm{S}(\bar{\mathrm{E}})/2} f_O(\bar{E}, \omega) R_{mn}, \tag{B.31}$$

where the average energy $\bar{E} = (E_m + E_n)/2$, the energy spacing $\omega = E_m - E_n$, and the thermodynamic entropy $S(\bar{E})$. Since from the Boltzmann formula the thermodynamic entropy is give by $\ln[W]$ with the number of the microscopic states W, one find that the factor $\mathrm{e}^{S(\bar{E})}$ represents the number of the energy levels at the vicinity of the energy $\bar{E}$. $O(\bar{E})$ and $f_O(\bar{E}, \omega)$ are smooth functions of their arguments. $O(\bar{E})$ corresponds to the expectation value of MCE at the energy $\bar{E}$. R_{mn} is a real (or complex) random variable with zero mean and unit variance.

Assuming ETH, the second term in Eq. B.8 is suppressed as $\exp[-S(\bar{E})/2]$ and vanishes in the limit of $S(\bar{E}) \to \infty$. As long as the variance of the energy of the initial state $|\psi\rangle$ is sufficiently small, the long time average is equal to $O(\langle E\rangle)$ with $\langle E\rangle = \langle\psi| \hat{H} |\psi\rangle = \sum_m |\psi_m|^2 E_m$ as

$$\overline{O} \simeq O(\langle E\rangle) \simeq O_{\mathrm{MCE}}. \tag{B.32}$$

One can evaluate the difference of the long time average assumed ETH and the expectation value in MCE by the Taylor expansion. A diagonal element O_{mm} is approximately equal to the function $O(E)$

at $E = E_m$ and can be expanded in

$$O_{mm} \simeq O(E_m) \simeq O(\langle E \rangle) + (E_m - \langle E \rangle) \frac{\mathrm{d}O(E)}{\mathrm{d}E}\bigg|_{E=\langle E \rangle} + \frac{1}{2}(E_m - \langle E \rangle)^2 \frac{\mathrm{d}^2 O(E)}{\mathrm{d}E^2}\bigg|_{E=\langle E \rangle} . \quad \text{(B.33)}$$

After substituting it to the long time average, One obtain

$$\overline{O} \simeq O(\langle E \rangle) + \frac{1}{2}(\delta E)^2 \frac{\mathrm{d}^2 O(E)}{\mathrm{d}E^2}\bigg|_{E=\langle E \rangle} , \quad \text{(B.34)}$$

where the fluctuation of the energy for a given initial state $(\delta E)^2 = \sum_m |\psi_m|^2 (E_m - \langle E \rangle)^2$. The first-order expansion vanishes after taking average under the diagonal ensemble.

Appendix C

Preparation of random configurations

Here, I describe the method to prepare the random configurations of the Rydberg atoms. The Rydberg atoms are trapped inside of an enclosing circle with diameter L and are subject to the Rydberg blockade with the blockade distance is $r_{\rm b}$.

A strategy to prepare the random configuration is as follows. (i) The atoms are put on a hexagonal lattice inside of the enclosing circle. (ii) The atoms are iteratively displaced with avoiding sticking out of the enclosing circle and violating the Rydberg blockade. After repeating this process 500 times, one obtain the random configuration of the Rydberg atoms. The detail protocol is provided below.

The position of the center of mass of the ith atom is denoted as $\vec{x}_i = (x_i, y_i)$ for $i = 1, 2, \cdots, N$. Each Rydberg atom is treated as a rigid circle with radius $r_{\rm b}$. The center and the diameter of the enclosing circle is set to origin $O = (0, 0)$ and L, respectively.

In the first step, I put the all atoms on a hexagonal lattice, whose primitive translation vectors are $(r_{\rm b}, 0)$ and $(r_{\rm b}/\sqrt{2}, \sqrt{3}r_{\rm b}/\sqrt{2})$. For $N = 19$, this configuration corresponds to the close-packing configuration.

In the second step, I iteratively displace the atom inside the enclosing circle without violating the Rydberg blockade. The direction and the distance of the displacement is randomly determined at each displacement. The direction is set to $\vec{n} = (\cos\theta, \sin\theta)$, and the angle is a random number drawn from a uniform distribution with the interval $[0, 2\pi]$. The displacement is performed by $\vec{x}_i \to \vec{x'}_i = \vec{x}_i + \Delta x\vec{n}$, where the distance of the displacement $\Delta x = \Delta x_{\rm max} s$ with a random number s drawn from a uniform distribution with the interval $[0, 1]$. $\Delta x_{\rm max}$ denotes the distance that an atom can displace in the direction $\vec{n}$ inside of the enclosing circle without violating the Rydberg blockade. The problem is to find $\Delta x_{\rm max}$.

In calculating the maximal distance $\Delta x_{\rm M}$, I consider only the ith atom and the jth atom. The ith atom displaces in the direction $\vec{n}$ and draws a linear trajectory (green line in Fig. C.1). An arbitrary point on the trajectory can be given by $\vec{x}_l = \vec{x}_i + l\vec{n}$, where the distance from $\vec{x}_i$ to that point $\vec{x}_l$ is l. Here, if the distance from the ith atom to the trajectory is smaller than $r_{\rm b}$, the ith atom stops its displacement when the ith atom is in touch with jth atom. The distance from the jth atom to the trajectory is given by the length of the perpendicular line from the jth atom $\vec{x}_j$ to the trajectory $\vec{n}$. The orthogonal condition of the perpendicular line and the trajectory, that is, $(\vec{x}_l - \vec{x}_j) \cdot \vec{n} = 0$ provides the coordinate of the crossing point of them: $x_{\rm M} = \{(\vec{x}_j - \vec{x}_i) \cdot \vec{n}\}\vec{n} + \vec{x}_i$. The length of the perpendicular line is $\sqrt{|\vec{x}_j - \vec{x}_i|^2 - \{(\vec{x}_j - \vec{x}_i) \cdot \vec{n}\}}$. Thus, the condition that the ith atom is in touch with the jth atom in the displacement is $\sqrt{|\vec{x}_j - \vec{x}_i|^2 - \{(\vec{x}_j - \vec{x}_i) \cdot \vec{n}\}} < r_{\rm b}$. If the

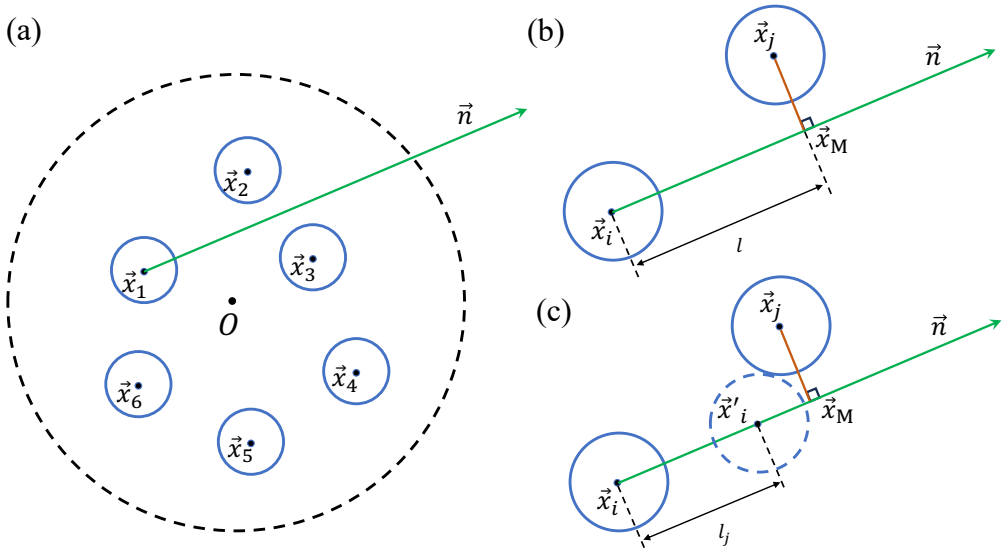

Fig. C.1 (a) Overall picture of configuration of atoms. (b) Enlarged picture of configuration. The ith atom is in touch with the jth atom in the displacement in the direction $\vec{n}$. The orange line is the perpendicular line from $\vec{x}_j$ to the trajectory of the displacement (green line). (c) Enlarged picture after the i atom is temporarily displaced until in touch with the jth atom.

condition is satisfied, one of the candidate of the maximal distance is given in the following way. Consider the situation where $i$the atom moves in the direction $\vec{n}$ until in touch with the jth atom as in Fig. C.1(c). The distance that the ith atom travels is $|\vec{x}_i' - \vec{x}_i| = |\vec{x}_{\rm M} - \vec{x}_i| - |\vec{x}_{\rm M} - \vec{x}_i'|$, where $\vec{x}_i'$ denotes the position of the ith atom after moving until in touch with the jth atom. One directly obtain $l_j \equiv |\vec{x}_i' - \vec{x}_i| = (\vec{x}_j - \vec{x}_i)\cdot\vec{n} - \sqrt{|\vec{x}_j - \vec{x}_i|^2 - \{(\vec{x}_j - \vec{x}_i)\cdot\vec{n}\}^2 - r_{\rm b}^2}$. l_j is the maximal distance if there is no atom other than ith and jth atoms. If the jth atom cannot be in touch with ith atom, i.e., $\sqrt{|\vec{x}_j - \vec{x}_i|^2 - \{(\vec{x}_j - \vec{x}_i)\cdot\vec{n}\}} > r_{\rm b}$, l_j takes the distance from x_i to the edge of the enclosing circle, $x_{\rm E} = \frac{1}{2}\sqrt{(\vec{x}_i\cdot\vec{n})^2 + L^2} - \frac{1}{2}\vec{x}_i\cdot\vec{n}$. After calculating l_j for all $j \neq i$, I define the smallest one in $\{l_j\}$ as the maximal distance $\Delta x_{\rm max}$.

After a single iteration of i, the configuration is expected to still have information about the initial configuration. Thus, I repeat the iteration until this information stochastically disappears. To quantify it, I adopt the Kullback-Leibler divergence

$$D_{\rm KL}(\rho||\sigma) = \int d\boldsymbol{x}\rho(\boldsymbol{x})\log\left[\frac{\rho(\boldsymbol{x})}{\sigma(\boldsymbol{x})}\right], \tag{C.1}$$

where the integral is calculated numerically over the area of the enclosing circle. The distribution $\rho(\boldsymbol{x})$ is selected as a sum of the Lorentz functions centered at the positions of atoms in the initial configuration $\{\boldsymbol{r}_i^0\}$ with widths $\eta = 0.05R$, $\rho(\boldsymbol{x}) = (1/N)\sum_i \eta/\left(|\boldsymbol{x} - \boldsymbol{r}_i^0|^2 + \eta^2\right)$. The distribution $\sigma(\boldsymbol{x})$ has the same form but the maximal value are at the positions of atoms in the updated configuration $\{\boldsymbol{r}_i^{n_{\rm it}}\}$, $\sigma(\boldsymbol{x}) = (1/N)\sum_i \eta/\left(|\boldsymbol{x} - \boldsymbol{r}_i^{n_{\rm it}}|^2 + \eta^2\right)$. I observe that after $M = 500$ iterations, the sample averaged $D_{\rm KL}(\rho||\sigma)$ does not depends on M.

This is the main part of the method to prepare the random configuration. However, for a large blockade radius $r_{\rm b} \gtrsim (L/2)\sqrt{\eta/0.2N}$, the configuration still is similar to the initial one after hundreds of iterations. This attributes to small distances $\Delta x_{\rm Max}$ by which atoms can be displaced in a single iteration. To obtain truly random configurations, I start simulations with a small blockade radius $r_{{\rm bl}^{(i)}} = 0.14L$ and perform 100 iterative displacements of atoms. Then, within the remaining 400 iterations, we increase the blockade radius 15 times according to $r_{\rm bl} \to r_{\rm bl}\sqrt[15]{r_{\rm bl}^{(f)}/r_{\rm bl}^{(i)}}$, where $r_{\rm bl}^{(f)}$ is the blockade radius that the atoms finally achieve.

Appendix D

Mean and standard deviation of energy

Here, I consider a mean value and a standard deviation of energy over all the eigenstates. The Hamiltonian is given by

$$\hat{H} = \frac{1}{2}\sum_{i=1}^{N}\sum_{\substack{j=1\\(j\neq i)}}^{N} J_{ij}\left(\hat{S}_i^x\hat{S}_j^x + \hat{S}_i^y\hat{S}_j^y + \Delta\hat{S}_i^z\hat{S}_j^z\right) \tag{D.1}$$

and is block-diagonalized into sectors labeled by the total z-component of spin $\hat{Z} = \sum_{i=1}^{N}\hat{S}_i^z$. For convenient, I denote the sector labeld by $\hat{Z}$ as $\mathcal{H}_{\hat{Z}}$.

Let's calculate the mean value of the Hamiltonian

$$\overline{E} = \frac{1}{\mathcal{D}}\mathrm{Tr}[\hat{H}], \tag{D.2}$$

where $\mathcal{D}$ is the dimension of the sector and trace is taken over the sector $\mathcal{H}_{\hat{Z}}$. The eigenbasis of the sector is spanned by $\{|\uparrow\rangle, |\downarrow\rangle\}^{\otimes N}$ whose number of up spins is limited to $N_\uparrow = Z + N/2$. The number of down spins $N_\downarrow$ is given by $N = N_\uparrow + N_\downarrow$. The dimension of the sector $\mathcal{D}$ is given by $N!/N_\uparrow!N_\downarrow!$. Since any eigenbasis is given as a product state of eigenstates of $\hat{S}_i^z$, the flip-flop term $\propto \hat{S}_i^x\hat{S}_j^x + \hat{S}_i^y\hat{S}_j^y$ is exactly zero. The mean value of the Hamiltonian is reduced into

$$\overline{E} = \frac{\Delta}{\mathcal{D}}\frac{1}{2}\sum_{i=1}^{N}\sum_{\substack{j=1\\(j\neq i)}}^{N} J_{ij}\mathrm{Tr}[\hat{S}_i^z\hat{S}_j^z]. \tag{D.3}$$

The remained task is calculating

$$\mathrm{Tr}[\hat{S}_i^z\hat{S}_j^z] = \sum_{s\in\mathcal{H}_{\hat{Z}}}\langle s|\,\hat{S}_i^z\hat{S}_j^z\,|s\rangle, \tag{D.4}$$

where $s = s_1 s_2 \cdots s_{N-1}s_N$ with a local spin state at i, $s_i = \uparrow, \downarrow$. The expectation value $\langle s|\,\hat{S}_i^z\hat{S}_j^z\,|s\rangle$ is $+1/4$ if $s_i = s_j$ in a state $|s\rangle$, otherwise is $-1/4$. I denote the number of the configurations where $s_i = s_j$ within $\mathcal{H}_{\hat{Z}}$ as $C_{\mathrm{P}}(N, Z)$ and the number of the configurations where $s_i \neq s_j$ as C_{N}. Apparently, $C_{\mathrm{P}} + C_{\mathrm{N}} = \mathcal{D}$. From elementary calculation, one find that

$$C_{\mathrm{P}} = \frac{(N-2)!}{(N_\uparrow-2)!N_\downarrow!} + \frac{(N-2)!}{N_\uparrow!(N_\downarrow-2)!}, \quad C_{\mathrm{N}} = 2\frac{(N-2)!}{(N_\uparrow-1)!(N_\downarrow-1)!}. \tag{D.5}$$

The trace is given by

$$\mathrm{Tr}[\hat{S}_i^z \hat{S}_j^z] = \frac{1}{4} C_{\mathrm{P}}(N,Z) - \frac{1}{4} C_{\mathrm{N}}(N,Z). \tag{D.6}$$

I emphasize that $C_{\mathrm{P}}(N,Z)$ and $C_{\mathrm{N}}(N,Z)$ have no dependence on either i or j. The mean value of the Hamiltonian is written in

$$\overline{E} = \frac{\Delta}{4\mathcal{D}} \frac{1}{2} \big(C_{\mathrm{P}}(N,Z) - C_{\mathrm{N}}(N,Z) \big) \sum_{i=1}^{N} \sum_{\substack{j=1 \\ (j \neq i)}}^{N} J_{ij}. \tag{D.7}$$

If one define the mean interaction within a realization as $\langle J \rangle := \frac{2!(N-2)!}{N!} \sum_{i=1}^{N} \sum_{j=i+1}^{N} J_{ij}$, the mean value of the Hamiltonian can be rewritten in

$$\begin{aligned} \overline{E} &= \frac{\Delta}{8} \Big(\frac{N_\uparrow!}{(N_\uparrow - 2)!} + \frac{N_\downarrow!}{(N_\downarrow - 2)!} - 2 \frac{N_\uparrow! N_\downarrow!}{(N_\uparrow - 1)!(N_\downarrow - 1)!} \Big) \langle J \rangle \\ &= \frac{\Delta}{8} \big(4Z^2 - N \big) \langle J \rangle. \end{aligned} \tag{D.8}$$

Here, I denote the eigenvalue of $\hat{Z}$ in the sector is Z.

Next, I consider the variance of the energy

$$(\delta E)^2 = \frac{1}{\mathcal{D}} \mathrm{Tr}[\hat{H}^2] - \overline{E}^2. \tag{D.9}$$

The cross terms proportional to $\hat{S}_i^\alpha \hat{S}_j^\alpha \hat{S}_k^\beta \hat{S}_l^\beta$ for $\alpha \neq \beta$ vanishes after taking the trace. For $\alpha = \beta$, terms proportional to $\hat{S}_i^x \hat{S}_j^x \hat{S}_k^x \hat{S}_l^x$ or $\hat{S}_i^y \hat{S}_j^y \hat{S}_k^y \hat{S}_l^y$ survive even after taking the trace only if $(i,j) = (k,l)$ or (l,k). In the case, these operators is reduced to $\hat{I}_{\mathcal{D}}/2^4$, where $\hat{I}_{\mathcal{D}}$ is an identity operator in $\mathcal{D}$-dimensional Hilbert space. Terms proportional to $\hat{S}_i^z \hat{S}_j^z \hat{S}_k^z \hat{S}_l^z$ survives for any (i,j,k,l) after taking the trace. The trace $\mathrm{Tr}[\hat{H}^2]$ can be reduced into

$$\mathrm{Tr}[\hat{H}^2] = \frac{1}{4} \sum_{i=1}^{N} \sum_{\substack{j=1 \\ (j \neq i)}}^{N} \sum_{k=1}^{N} \sum_{\substack{l=1 \\ (l \neq k)}}^{N} J_{ij} J_{kl} \Big(\mathrm{Tr}[\hat{S}_i^x \hat{S}_j^x \hat{S}_k^x \hat{S}_l^x] + \mathrm{Tr}[\hat{S}_i^y \hat{S}_j^y \hat{S}_k^y \hat{S}_l^y] + \Delta^2 \mathrm{Tr}[\hat{S}_i^z \hat{S}_j^z \hat{S}_k^z \hat{S}_l^z] \Big). \tag{D.10}$$

The trace $\mathrm{Tr}[\hat{S}_i^z \hat{S}_j^z \hat{S}_k^z \hat{S}_l^z] = \sum_{s \in \mathcal{H}_{\hat{Z}}} \langle s | \hat{S}_i^z \hat{S}_j^z \hat{S}_k^z \hat{S}_l^z | s \rangle$ can be calculated by division into cases. For $(i,j) = (k,l)$ or (l,k), $\hat{S}_i^z \hat{S}_j^z \hat{S}_k^z \hat{S}_l^z = \hat{I}_{\mathrm{D}}/2^4$. For the case that $i = k$ and $j \neq l$, $i = l$ and $j \neq k$, $i \neq k$ and $j = l$ or $i \neq l$ and $j = k$, the trace is $\mathrm{Tr}[\hat{S}_j^z \hat{S}_l^z]/4$, $\mathrm{Tr}[\hat{S}_j^z \hat{S}_k^z]/4$, $\mathrm{Tr}[\hat{S}_i^z \hat{S}_k^z]/4$ or $\mathrm{Tr}[\hat{S}_i^z \hat{S}_l^z]/4$, respectively. As we saw above, these trace can be evaluated as

$$\frac{1}{4} \mathrm{Tr}[\hat{S}_i^z \hat{S}_k^z] = \frac{1}{2^4} (C_{\mathrm{P}} - C_{\mathrm{N}}). \tag{D.11}$$

For the other case of i,j,k,l, $\mathrm{Tr}[\hat{S}_i^z \hat{S}_j^z \hat{S}_k^z \hat{S}_l^z]$ is $+1/2^4$ if $s_i = s_j = s_k = s_l$, or two of (s_i, s_j, s_k, s_l) are up and the others are down, and is $-1/2^4$ if one of (s_i, s_j, s_k, s_l) are up and the others are down, or three of (s_i, s_j, s_k, s_l) are up and the others are down. The numbers of the configurations satisfying

the former case and the latter case are denoted as $B_{\rm P}$ and $B_{\rm N}$, respectively. They are calculated as

$$\begin{aligned} B_{\rm P} &= \frac{(N-4)!}{(N_\uparrow-4)!N_\downarrow!}+6\frac{(N-4)!}{(N_\uparrow-2)!(N_\downarrow-2)!}+\frac{(N-4)!}{N_\uparrow!(N_\downarrow-4)!}, \\ B_{\rm N} &= 4\frac{(N-4)!}{(N_\uparrow-3)!(N_\downarrow-1)!}+4\frac{(N-4)!}{(N_\uparrow-1)!(N_\downarrow-3)!}. \end{aligned} \tag{D.12}$$

The first term can be calculated as

$$\sum_{i=1}^{N}\sum_{\substack{j=1\\(j\neq i)}}^{N}\sum_{k=1}^{N}\sum_{\substack{l=1\\(l\neq k)}}^{N} J_{ij}J_{kl}{\rm Tr}[\hat{S}_i^x\hat{S}_j^x\hat{S}_k^x\hat{S}_l^x] = \frac{\mathcal{D}}{16}\sum_{i=1}^{N}\sum_{\substack{j=1\\(j\neq i)}}^{N}J_{ij}^2 = 2\frac{\mathcal{D}}{16}\frac{N(N-1)}{2}\langle J^2\rangle, \tag{D.13}$$

where $\langle J^2\rangle = (1/2)\frac{2}{N(N-1)}\sum_{i=1}^{N}\sum_{\substack{j=1\\(j\neq i)}}^{N}J_{ij}^2$. The second term is

$$\begin{aligned} &\sum_{i=1}^{N}\sum_{\substack{j=1\\(j\neq i)}}^{N}\sum_{k=1}^{N}\sum_{\substack{l=1\\(l\neq k)}}^{N} J_{ij}J_{kl}{\rm Tr}[\hat{S}_i^z\hat{S}_j^z\hat{S}_k^z\hat{S}_l^z] \\ = \;& 2\frac{\mathcal{D}}{16}\frac{N(N-1)}{2}\langle J^2\rangle + 4\sum_{ijk}(1-\delta_{ij})(1-\delta_{jk})(1-\delta_{ki})J_{ij}J_{ik}\frac{1}{4}\frac{C_{\rm P}-C_{\rm N}}{4} \\ &+\sum_{ijkl}(1-\delta_{ij})(1-\delta_{jk})(1-\delta_{kl})(1-\delta_{li})(1-\delta_{ik})(1-\delta_{jl})J_{ij}J_{kl}\frac{B_{\rm P}-B_{\rm N}}{16} \end{aligned} \tag{D.14}$$

Thus, the mean of the squared Hamiltonian is

$$\begin{aligned} \frac{1}{\mathcal{D}}{\rm Tr}[\hat{H}^2] &= \frac{(2+\Delta^2)}{4}\frac{N(N-1)}{16}\langle J^2\rangle + \frac{\Delta^2}{4\mathcal{D}}\sum_{ijk}(1-\delta_{ij})(1-\delta_{jk})(1-\delta_{ki})J_{ij}J_{ik}\frac{C_{\rm P}-C_{\rm N}}{16} \\ &+\frac{\Delta^2}{4\mathcal{D}}\sum_{ijkl}(1-\delta_{ij})(1-\delta_{jk})(1-\delta_{kl})(1-\delta_{li})(1-\delta_{ik})(1-\delta_{jl})J_{ij}J_{kl}\frac{B_{\rm P}-B_{\rm N}}{16}. \end{aligned} \tag{D.15}$$

Appendix E

Method of bipartitions

In lattice models with spins, one can define easily the bipartition because each spin is fixed at the site of the lattice. On the other hand, since the Rydberg atoms randomly distribute, there is no natural definition of the bipartition with subsystem A and its environment $\bar{\mathrm{A}}$. If one do not take in account the geometries of the atoms, the number of the bipartitions is estimated to be $N!/\lfloor N/2 \rfloor !(N - \lfloor N/2 \rfloor)!$ with the number of the atoms N. However, the number is quite large in the interest N, and the bipartitions include the atom geometrically apart from the other atoms in the same subsysetm A.

I adopt two methods of the bipartitions. The first method is based on the geometrically equal bipartition of the area of the enclosing circle. This method is adapted for the even N. In the preparation of the random configuration, a half number of the atoms are displaced within the upper half of the enclosing circle while the other atoms are displaced within the lower half. In this way, one obtain the line that divides the atoms into two and at the same time divides the area of the enclosing circle in two equal areas.

The second one is a method that one picks up $\lfloor N/2 \rfloor$ atoms closest to a point $\boldsymbol{X} = (X, Y)$ inside of the enclosing circle. The subsystem A made by this method forms a round shaped cloud. However, elongated clouds of the subsystem A are also acceptable in that there is no atom apart from the other atoms in the same subsystem A. To obtain the elongated cloud, I transform from circles to ellipses in calculating the distance of an atom from $\boldsymbol{X}$.

The transformation is parameterized by two parameters, θ and ϕ. The circle-ellipse transformation is squeezing a circle in a direction with conserving the area. The first parameter θ controls the direction to stretch, which is performed by the rotation. The rotation operator is defined as

$$\mathcal{R}_\theta = \begin{pmatrix} \cos\theta & -\sin\theta \\ \sin\theta & \cos\theta \end{pmatrix}. \tag{E.1}$$

The rotated coordinate of an atom is

$$\boldsymbol{x}_i \to \boldsymbol{x}_i' = \mathcal{R}(\theta)\boldsymbol{x}_i. \tag{E.2}$$

Then, I stretch the circle along with the rotated axis. The stretching operator is defined as

$$\mathcal{L}_\phi = \begin{pmatrix} \tan\phi & 0 \\ 0 & \cot\phi \end{pmatrix}. \tag{E.3}$$

Finally, I rotate the coordinate with the angle $-\theta$ and obtain the final form of the transformed coordinate as

$$\boldsymbol{x}_i \to \boldsymbol{x}'_i = \mathcal{R}(-\theta)\mathcal{L}(\phi)\mathcal{R}(\theta)\boldsymbol{x}_i. \tag{E.4}$$

The distance between the ith atom and the point $\boldsymbol{X}$ after the transformation is given by

$$d_{\theta,\phi}(\boldsymbol{x}_i, \boldsymbol{X}) = \sqrt{(x'_i - X')^2 + (y'_i - Y')^2}. \tag{E.5}$$

According to this measure, one can obtain the subsystem A with elongated cloud by picking up $\lfloor N/2 \rfloor$ atoms with the smallest $d_{\theta,\phi}(\boldsymbol{x}_i, \boldsymbol{X})$.

A set of parameters $\{\boldsymbol{X}, \theta, \phi\}$ provide a bipartition. To obtain various bipartitions, one needs to input various parameters. I parameterize $\boldsymbol{X} = (\beta\mathrm{cos}\alpha, \beta\mathrm{sin}\alpha)$ with increasing $\alpha \equiv (\sqrt{5}n - \lfloor\sqrt{5}n\rfloor)\pi,\ \beta \equiv (\sqrt{7}n - \lfloor\sqrt{7}n\rfloor)R$. At the same time, $\theta = (\sqrt{2}n - \lfloor\sqrt{2}n\rfloor)\pi,\ \phi = (\sqrt{3}n - \lfloor\sqrt{3}n\rfloor)\pi$. The parameter $n \in \mathbb{N}$ is iteratively increased until 100 inequilvalent bipartitions are obtained.